Modeling cellular responses to low-dose radiation and their medical implications

by

Oluwole Victor Olobatuyi

A thesis submitted in partial fulfillment of the requirements for the degree of

Doctor of Philosophy

in

Applied Mathematics

Department of Mathematical and Statistical Sciences
University of Alberta

Abstract

Ionizing radiation is widely used in treatment and medical diagnosis. Doses in the range of 1.5 Gy to 10 Gy are used in radiation treatment of cancer. Lower doses (less than 1.5 Gy) are used in medical imaging, and also are incurred by tissues that are near irradiated target volumes. The impact of treatment doses on healthy and pathological tissues has been analyzed in great detail and sophisticated mathematical models have been developed. A successful model, for example, is the so-called Linear Quadratic (LQ) model, which describes the survival fraction of cells as a function of radiation dose.

Recent experimental studies on low-dose radiation of tissue have shown a discrepancy with the standard LQ model; cell damage is much larger than expected by the LQ model. This phenomenon has been called hyper-radiosensitivity and increased radioresistance (HRS/IRR).

In this thesis, I develop and analyze mathematical models to understand the HRS/IRR phenomenon, and to analyze corresponding experimental data on low-dose radiation. I focus on two primary biological hypotheses, namely the radiation-induced bystander effects and the cell-cycle G2-checkpoint effects. I show that both hypotheses are able to explain the HRS/IRR phenomenon.

The bystander effects (BEs) are consequences of distress signals (also known as the bystander signals) that are emitted by radiation-damaged cells. The model for the BEs is a complex system of reaction-diffusion partial differential equations (PDEs), which incorporates BEs like bystander signal-induced death

and damage, and the bystander signal-dependent repair. I fit this model to experimental data and estimate model parameters. I analyze the steady states of this model and I identify long transients in the dynamics of bystander signals, consistent with biological observations. Moreover, I show the existence and uniqueness of weak solutions, and the existence of a compact global attractor for the system of PDE. Additionally, I analyze the effect of bystander signals on invasion of cancer into healthy tissue and I show that the bystander signal can accelerate cancer invasion.

On the other hand, the cell cycle G2-checkpoint is a regulatory mechanism that ensures that damaged cells in G2 phase of the cell cycle are repaired before progressing to the next phase. Experiments have shown that some damaged cells evade the G2 checkpoint, which result in cell death in the next phase. The model for the G2-checkpoint effects is derived from cell-cycle dynamics and this model can also explain the HRS/IRR phenomenon as observed in experiments on several cell lines. In fact, I have been able to derive explicit formulas that relate the HRS/IRR phenomenon to their underlying cell-cycle events, as well as to the surviving fraction at 2 Gy. This work has been able to resolve such a highly debated relationship.

Considering two possible explanations for the HRS/IRR phenomenon, I found evidence in the literature that these effects (bystander and G2-checkpoint) are mutually exclusive. For a given cell line, typically only one of these effects is important.

The HRS/IRR is a serious concern for tissues that are exposed to low-dose radiation and the low-dose risk assessment will have to be updated. On the other hand, low-dose radiation might suggest novel therapies for cancer treatment that benefit from a better understanding of the HRS/IRR phenomenon.

Preface

Chapter 2 of this thesis has been published as: Olobatuyi, Oluwole, de Vries, Gerda, and Hillen, Thomas. *A reaction-diffusion model for radiation-induced bystander effects.* Journal of Mathematical Biology 75(2) pp. 341-372, 2017. I was responsible for the idea formulation, model development and analyses. I was also responsible for writing the manuscript under the supervision of Drs. Gerda de Vries and Thomas Hillen.

Chapter 5 of this thesis has also been published as: Olobatuyi, Oluwole, de Vries, Gerda, and Hillen, Thomas. *Effects of G2 checkpoint dynamics on low-dose hyper-radiosensitivity.* Journal of Mathematical Biology, *in-press.* I was responsible for the idea formulation, model development and analyses. I was also responsible for writing the manuscript under the supervision of Drs. Gerda de Vries and Thomas Hillen.

I dedicate this thesis to God Almighty, the bedrock of my life.

Acknowledgements

I like to seize this opportunity to thank everyone who has contributed to the completion of this work.

Firstly, I would like to thank my supervisors, Drs. Gerda de Vries and Thomas Hillen, for their excellent guidance and financial support during the last five years. Their deliberate commitment to excellence in providing honest feedback and contagious enthusiasm in motivating the same in their students are extremely invaluable. I would also like to thank every member of the Mathematical Biology Journal Club and the Collaborative Mathematical Biology Group, whose feedback and ideas throughout the years were great treasures.

I would also like to acknowledge generous financial support from the University of Alberta. These were received at various times and in many forms including the President's International Doctoral Award, Queen Elizabeth II Graduate Scholarship - Doctoral level, and departmental teaching assistantships. This work would have been impossible without these sources of financial support.

I am forever grateful for the continuous encouragement from my wife (Taiwo) during this work. The birth of our beautiful daughter (Joy) during the last phase of this project was a great addition, not only to my family but also to my source of encouragement. The constant assurance and prayers from my parents (Johnson and Beatrice) can never be overemphasized. The sacrificial assistance and mentoring into parenthood by my mother-in-law (Adenike Sharomi) is extremely invaluable.

Finally, to my greatest inspiration, the only wise God, Jesus Christ our Saviour, be Glory and Majesty and Dominion and Power, both now and forever. Amen!

Table of Contents

List of Tables

List of Figures

Chapter 1

Introduction

In this chapter, we introduce radiation terminologies and experiments, and also motivate the central research questions investigated with mathematical models in this thesis.

In Section 1.1, we give a general introduction to ionizing radiation and their usage in cancer treatments and medical imaging. We describe the cell survival experiment from which the cell survival data used in this thesis were measured. Finally, we discuss one of the classical mathematical models earlier used to study cell survival. In Section 1.2, we review the effects of low doses of radiation on some cell lines, discuss some possible underlying mechanisms, and review one of the earlier mathematical models used to understand these effects. In Section 1.3, we outline the experimental data of different cell lines used in this thesis. In Section 1.4, we outline the research questions that will be answered in this thesis. In Sections 1.5 and 1.6, we discuss the significance of modeling cellular responses at low doses and the outline of main results of the thesis, respectively.

1.1 Ionizing radiation

Ionizing radiation is widely used in the treatment of more than 50% of cancer types and in various types of medical imaging. The effects of large doses of ionizing radiation on different tissues and cell lines are well studied. Much of these studies are attributed to the availability of epidemiological data from the atomic bomb survivors of Hiroshima and Nagasaki in 1945 [91], as well as emergency workers that responded to the Chernobyl nuclear power plant accident in 1986 [64]. Other sources of data include *in vivo* animal experiments [62, 120, 77, 79] and *in vitro* cell culture experiments [76, 82, 11, 80, 5]. In these studies, effects such as genetic mutations, carcinogenesis, cell death, and acute organ damage were observed.

According to the Canadian Nuclear Safety Commission[1], radiation from nuclear material is strictly regulated and humans seldom experience large doses. Meanwhile, there is an increase in the use of low-dose radiation in cancer treatments and in medical imagining such as dental scan, magnetic resonance imaging (MRI), computed tomography (CT), and X-ray scan. Incidental radiation exposures such as airplane has also increased. Studies on the effects of low-dose radiation are relatively recent, and suggest that these effects may have been underestimated. One of these studies, involving *in vitro* cell culture experiment, will be described in the following subsection.

1.1.1 Cell survival experiment

In an attempt to investigate the effects of radiation doses on cells, cell survival or cell death has been the measuring endpoint of most experiments [45, 108]. The cell survival curve describes the relationship between radiation doses and the proportion of cells that ‘survive’ - sometimes called the cell surviving fraction. Since cell survival, or its converse, cell death, can have different contextual interpretations, a precise definition is essential. For differentiated cells that do not proliferate, such as nerve, muscle, or secretory cells, death can be defined as the loss of a specific function. Whereas for proliferating cells, such as stem cells in the hematopoietic system or the intestinal epithelium, loss of the capacity for sustained proliferation - that is, loss of reproductive integrity - is an appropriate definition for death. This is sometimes called reproductive death and is usually the endpoint measured with cell-cultured *in vitro* experiments [38].

---

[1] http://nuclearsafety.gc.ca/eng/nuclear-substances/index.cfm

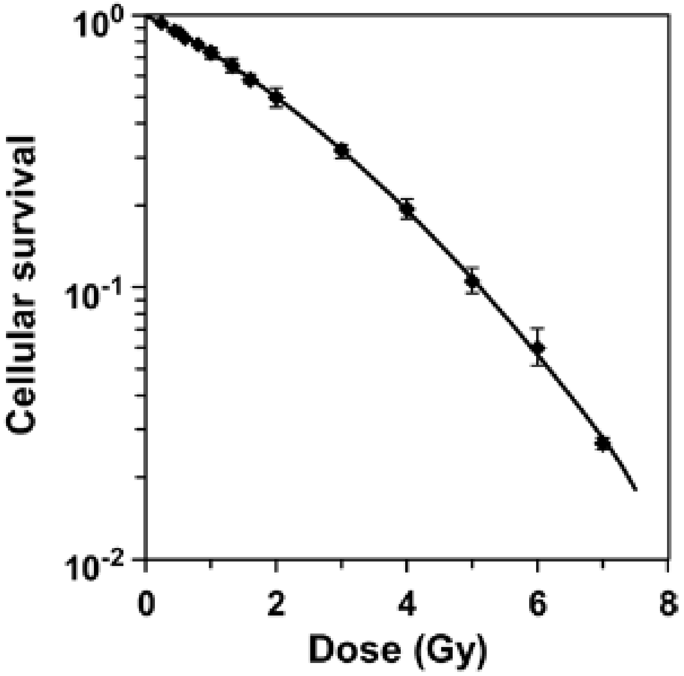

Figure 1.1: Shape of surviving curve for mammalian cells exposed to radiation. The surviving fraction axis is on a logarithmic scale while the dose axis is on a linear scale. Adapted from [12].

These *in vitro* experiments were conducted to study the surviving fraction of cells exposed to varying degrees of radiation doses. In these experiments, as described in [66], cells maintained in a suspension culture are irradiated at room temperature (21-24^{0}C) in sealed culture flasks. During irradiation, the cell suspension is stirred continuously using a magnetic stirrer. Cell samples are then removed sequentially at specified doses and seeded into tissue culture-grade plastic dishes. Dishes are incubated at 37^{0}C in a water saturated atmosphere for at least 7 days. The dishes are then stained and colonies containing $\geq$ 50 cells are scored as surviving cells from the original irradiated suspension. The choice of 50 cells might be due to the minimum number of cell cluster visible under the microscope. The surviving fraction (SF) is then computed as

$$\mathrm{SF} = \frac{\mathrm{CC}}{\mathrm{CI} \times \mathrm{PE}},$$

where CC denotes the number of irradiated colonies counted after the 7 day-incubation period, CI denotes the initial number of cells (colonies) exposed to radiation, and PE denotes the plating efficiency, which describes the % of colonies that survive in a control dish (without radiation). Let's illustrate this experiment with the following example.

Example 1 (Adapted from [38])**.** *Suppose there are 70 colonies in an unirradiated control dish, after 100 cells were seeded and allowed to grow for 7 days before being stained. Suppose also that in a separate experiment, there are 32 colonies on the dish after 2000 cells were seeded and then exposed to 2Gy of x-rays. Then the surviving fraction (SF) of the irradiated cells is* $\frac{32}{2000\times 0.7} \approx 0.023$.

A typical surviving fraction curve for mammalian cells, together with the corresponding surviving fraction data are usually presented in the form shown in Fig. 1.1, with dose (on the horizontal axis) plotted on a linear scale, and the surviving fraction (on the vertical axis) on a logarithmic scale. In the next subsection, we will review some of the mathematical models developed to study the surviving fraction data.

1.1.2 Linear Quadratic Model

Mathematical models such as the Linear Quadratic (LQ) model were built to study surviving fraction data. By the LQ model, the expression for dose-dependent cell survival is given by

$$S_0(D) = e^{-\alpha D - \beta D^2}, \tag{1.1}$$

where S_0 is the surviving fraction at dose D. The constants α and β are the component of radiation-induced cell killing that are respectively proportional to D and D^2. In Chapter 2, these constants will be described in terms of the deoxyribonucleic acid (DNA) double strand breaks and of the interactions between binary misrepair of two double strand breaks, respectively. In the meantime, the component of cell killing that are proportional to dose (i.e., αD) and to the square of dose (i.e., βD^2), respectively, are equal when $D = \frac{\alpha}{\beta}$.

The $\frac{\alpha}{\beta}$ ratio is useful for predicting likely radio-responsiveness in cells. For example, low values of $\frac{\alpha}{\beta}$ ratio (say between 1.5 - 5 Gy) indicate that the surviving curves are bending rapidly at low doses per single radiation exposure (also known as radiation fraction). Hence, there are more cell killing at low doses per fraction. On the other hand, high values of $\frac{\alpha}{\beta}$ (say between 6 - 14 Gy) indicate a greater predominance of the linear (α) term, so that changes in dose size per fraction have lesser effects on the survival rate of such cells [117]. Simply put, cells with high values of $\frac{\alpha}{\beta}$ require high doses to incur the same cell killing that will be easily achieved by low doses in cells with low $\frac{\alpha}{\beta}$. The range of values for $\frac{\alpha}{\beta}$ in tumor cells is usually higher than the range for normal cells. In a review paper [117], out of the 48 tumor cell lines investigated, 36 of them have values > 8 Gy, while only 4 out of 48 tumors have values less than 5 Gy. This high $\frac{\alpha}{\beta}$ for tumor cell lines may be responsible for their radioresistance to low doses [98, 7].

The LQ model is a good approximation to the surviving fraction of cells at doses > 1 Gy. Earlier attempts to also understand the dynamics of cell death at low doses simply extrapolated the LQ model to low radiation doses. As shown in Fig. 1.1, such extrapolations adduce little or no radiation consequence with low doses of radiation. In the next section, we will zoom in to the effects of low doses of radiation on cells and review one of the mathematical models earlier developed to study such effects.

1.2 Effects of low doses of radiation on cells

In the last decade, attention has shifted to the study of cell survival at low doses. These have resulted in increasing experimental evidence that exposure to low doses (< 1 Gy) can be quite dangerous. In fact, experiments have shown that higher-than-expected proportions of cells in some cell lines undergo cell death in response to low doses of radiation. This effect is called hyper-radiosensitivity (HRS). Following this effect, some cell lines also undergo increased resistance to radiation, a phenomenon called increased radio-resistance (IRR) [65, 71, 108, 52, 53]. These low-dose radiation effects on cell survival are illustrated in Figure 1.2. In addition, effects like enhanced cancer invasion [46, 111], increased cell damage, mutation, and carcinogenesis, have also been

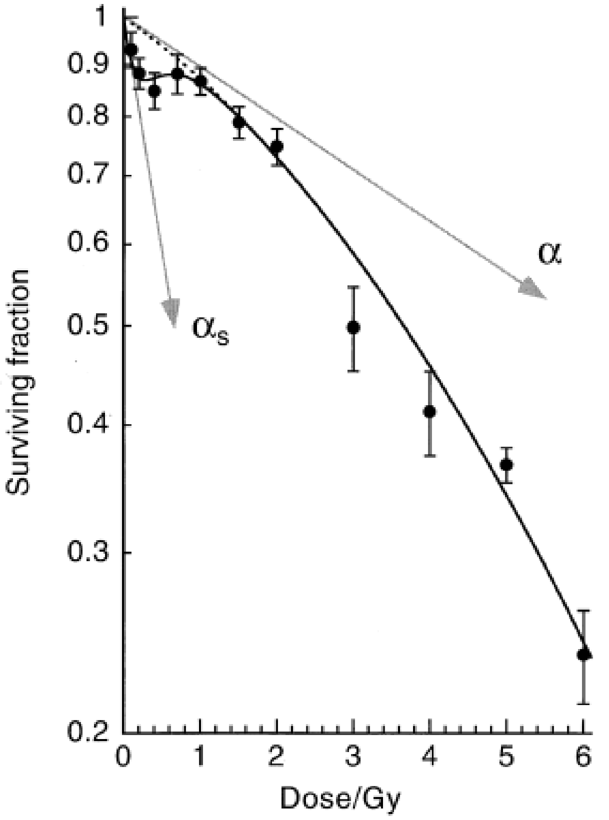

Figure 1.2: Surviving fraction curve of T98G human glioma cells irradiated with X-rays. The curve illustrates the phenomena of HRS and IRR. The solid curve is the IR model while the dotted curve is the LQ model. $-\alpha_s$ denotes the initial slope of the IR model while $-\alpha$ denotes initial slope of the LQ model. Figure is from Joiner [45]

observed in cells exposed to low doses of radiation.

The rest of this section is organized as follows. In Subsection 1.2.1, we review one of the mathematical models that was developed to understand the HRS/IRR phenomenon. In Subsection 1.2.2, we explore possible underlying mechanisms for the HRS/IRR phenomenon.

1.2.1 Induced Repair Model

Since the LQ model is unable to capture the cell survival at low doses, there is the need to build new models that can explain these low-dose responses.

Marples and Joiner in 1993 [66] responded by formulating a phenomenological model from the existing LQ model by introducing two additional parameters α_s and D_c. This model, which is called the Induced Repair (IR) model, expresses dose-dependent cell survival as

$$S_1(D) \;=\; \exp\Big\{-\alpha\Big(1+\Big(\frac{\alpha_s}{\alpha}-1\Big)e^{-\frac{D}{D_c}}\Big)D-\beta D^2\Big\}. \tag{1.2}$$

The parameter D_c describes the dose at which the surviving fraction curve attains minimum at low doses (usually < 1 Gy). This is also the dose at which cell's response switches from HRS to IRR. The parameter $-\alpha_s$ describes the slope of the surviving fraction curve at $D = 0$ (see Figure 1.2). Ever since the IR model was built, it has been widely used to model the HRS/IRR phenomenon. In fact, the index $\frac{\alpha_s}{\alpha}$ is commonly used to quantify the amount of HRS in cell lines [66, 68, 67]. Although the IR model is able to describe the low-dose cellular response, it is not capable of explaining the internal cellular mechanisms that cause the observed low-dose phenomenon.

1.2.2 Possible underlying mechanisms for HRS/IRR

Experiments [105, 88, 67, 65] have shown that the HRS/IRR phenomenon can be explained by two mutually exclusive cellular events [81], namely the radiation-induced bystander effects and the activity of the cell cycle G2 checkpoint. The hypothesis of radiation-induced bystander effects adduced that cells exposed to low dosees of radiation emit distress signals, also know as the bystander signals. These signals trigger secondary radiation effects like cell death, cell damage, mutation, genomic instability, and so on. Consequently, the increased cell death observed at low doses is due to the secondary death induced by the bystander signals. Examples of bystander signals include p53-induced cytochrome-complex [104, 23, 31, 32, 49], matrix metalloproteinase-induced vascular endothelial growth factor [42], reactive oxygen species [1], etc. This hypothesis will be made more explicit in Chapter 2, where we develop a detailed mathematical model to investigate the dynamics of bystander signals in tissue.

On the other hand, the hypothesis involving the activities of the G2 check-

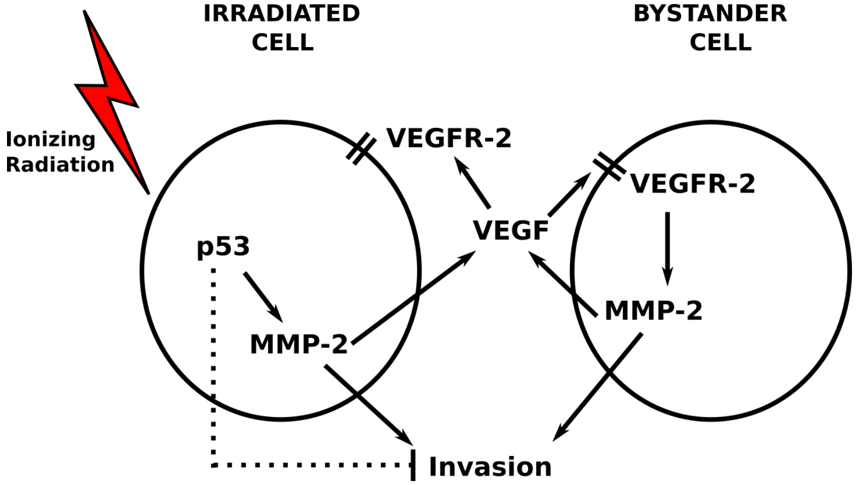

Figure 1.3: A proposed p53-regulated signal pathways in radiation-enhanced invasiveness of irradiated cells and their bystanders. Image adapted from He et. al [42].

point states that at low doses, damaged cells in the G2-phase of the cell cycle fail to undergo cell cycle arrest that leads to damage repair [100]. Rather the damaged cells proceed to the next phase of the cell cycle (i.e., the mitotic phase), where they undergo mitotic catastrophe (another form of cell death which occurs in the mitotic phase of the cell cycle) [16]. This hypothesis will be made more explicit in Chapter 5, where we develop a cell cycle model that incorporates G2-checkpoint dynamics to investigate the HRS/IRR phenomenon.

The mechanism and the dynamics of radiation-induced bystander effects and that of the cell cycle G2-checkpoint are still not well understood. Experiments have shown that the low-dose HRS/IRR phenomenon might play an important role in cancer invasion. In fact, experiments have also shown that enhanced cellular invasion in some cancer cell lines have been attributed to the activity of bystander effects [110, 19, 47, 37, 9, 97, 119, 18] (also see Figure 1.3). Intuitively, this could be the result of low dose exposure of normal cells surrounding the treated tumor cells. This low-dose exposure in turn results in both direct and indirect radiation effects that degrade the normal cells. Meanwhile, the tumor, which is often resistant to radiation and aggressive, now has more room to invade. These ideas will be made more explicit in Chapter 4, where we generalize the system of PDEs model for bystander effects to investigate the role of bystander effects on tumor invasion into surrounding normal cells.

1.3 Experimental data of cell survival

In this thesis, we work with some data of cell survival for different cell lines. These cell lines include glioblastoma tumor cell line (T98G) [45, 108], prostate cancer cell line (PC3) [73], Chinese hamster (V79) cell line [66, 69], human lung carcinoma cell line (A549) [118], human colon cancer cell line (HT29) [118], prostate epithelial cell line (RWPE1) [73], human astrocytoma cell line (U373) [108], etc. These data were measured via similar experiments described earlier in Section 1.1 and each cell line has been shown to exhibit HRS/IRR phenomenon. These cells were exposed to 250 - 320-kVp X-rays with a dose range between 0.01 - 6 Gy. Their incubation periods vary between 7 - 9 days for different cell lines. Each data point represents about 10-12 experiments and is presented as mean ± standard deviation.

1.4 Research Questions

This thesis is based on formulating and analyzing novel mathematical models to answer the following research questions:

1. Can bystander effects explain the HRS/IRR phenomenon?
2. What are the dynamics of radiation-induced bystander signals in tissues?
3. Are mathematical properties like local and global existence, and global attractor supported by the system of PDEs developed to model the bystander effects?
4. What are the effects of bystander signals on the speed and shape of invading tumor waves into its surrounding normal tissue?
5. Can the activity of the G2-checkpoint explain the HRS/IRR phenomenon?

6. How does the classical index $\frac{\alpha_s}{\alpha}$ for measuring the HRS in cells relate to the underlying cellular events that contribute to its occurrence?
7. Is there a relationship between the HRS index $\frac{\alpha_s}{\alpha}$ and the cell surviving fraction at 2 Gy?

1.5 Importance of modeling cellular responses to low doses of radiation

Both radiation-induced bystander effects and the dynamics of G2-checkpoint result from complex cellular events. For instance, in order to understand the dynamics of bystander signals, interactions such as direct and indirect radiation-induced cell death and damage, and bystander signal-dependent repair mechanisms are very important. Sometimes, the bystander effects are overshadowed by the direct radiation effects, which makes it very difficult to study experimentally. On the other hand, the dynamics of G2-checkpoint involves cellular interactions such as mitotic catastrophe, activation of checkpoint, cell damage, and direct radiation-induced death. Thus, in order to understand such complex systems, the information gathered from biological experiments and medical diagnostic data alone are not sufficient. Using mathematical models, and rigorous mathematical analyses, we can obtain insight into possible mechanisms driving these low-dose phenomena.

A sizeable number of phenomenological and stochastic models, and few hybrid of stochastic and continuum models have been formulated to investigate some research questions relating to these interactions. We will reserve the detailed literature review of these prior modeling attempts and our rationale for formulating novel continuum models for the respective chapters of this thesis, where each effects is investigated.

1.6 Outline of the main results

In this thesis, we formulate and analyze continuum models including systems of partial and ordinary differential equations to answer research questions stated in Section 1.4.

In Chapter 2, we formulate and analyze a system of reaction-diffusion partial differential equations that model the evolution of cells exposed to low doses of radiation in relation to the emission and response to bystander signals. We employ an affine invariant Markov Chain Monte Carlo procedure [35] to fit the model to a surviving fraction of glioblastoma cells [45]. We estimate the model parameters and their respective 95% credible intervals. We use numerical simulation to recover the dynamics of bystander signals found in the literature [91, 36]. By employing phase plane and bifurcation analyses, we show that the model has a saddle node bifurcation, which explains the switch between long persistence dynamics and decay of signals depending on the choice of parameters. The significance of this work is that it allows us to elucidate in detail how cell parameters influence the persistence of emitted bystander signals. Chapter 2 has been published in [89].

In Chapter 3, we study the existence of weak solutions to the system of partial differential equations formulated in Chapter 2. We use the classical method of Galerkin approximations to show the existence of weak solutions after a single radiation exposure. Furthermore, during multiple radiation exposure, we employ mollification in time to 'smoothen out' the temporal discontinuity in the model. Then we apply a uniform convergence in an appropriate Sobolev space to show existence of weak solutions. After single radiation exposure, we show the existence of the global attractor for the model.

In Chapter 4, we extend the system of reaction-diffusion partial differential equations to two cell lines - tumor and normal cells. The main motivation for this chapter is to study the effects of bystander signals on the speed and shape of invading tumor waves into surrounding normal cells. Using the method of matched asymptotic analysis and singular perturbation [27], we compute the asymptotic wave speed and show that it agrees very well with the numerical simulation. We identify the parameter regime that supports such traveling wave solutions.

In Chapter 5, we formulate a system of ordinary differential equations from an underlying cell-cycle dynamics. We also incorporate the dynamics of the G2 checkpoint and radiation treatment. Using the techniques for solving systems of linear differential equations, we derive an analytical formula for measuring the magnitude of hyper-radiosensitivity in cells. The relevance of this work is that it connects the magnitude of HRS measured by the classical Induced Repair (IR) model to its underlying cellular events. This derivation is validated with experimental data. We also derive an analytical relationship between index $\frac{\alpha_s}{\alpha}$ and the radioresistance at 2 Gy. Chapter 5 has been published in [90].

In Chapter 6, we conclude with a discussion, which presents the results of this thesis in their scientific context, and also outlines possible future research directions.

Chapter 2

A reaction-diffusion model for radiation-induced bystander effects

The work presented in this chapter has been published as: Olobatuyi, Oluwole, Gerda de Vries, and Thomas Hillen. *A reaction-diffusion model for radiation-induced bystander effects.* Journal of mathematical biology 75(2) pp. 341-372, 2017.

Abstract. *We develop and analyze a reaction-diffusion model to investigate the dynamics of the lifespan of a bystander signal emitted when cells are exposed to radiation. Experimental studies by Mothersill and Seymour 1997, using malignant epithelial cell lines, found that an emitted bystander signal can still cause bystander effects in cells even 60h after its emission. Several other experiments have also shown that the signal can persist for months and even years. Also, bystander effects have been hypothesized as one of the factors responsible for the phenomenon of low-dose hyper-radiosensitivity and increased radioresistance (HRS/IRR). Here, we confirm this hypothesis with a mathematical model, which we fit to Joiner's data on HRS/IRR in a T98G glioma cell line. Furthermore, we use phase plane analysis to understand the full dynamics of the signal's lifespan. We find that both single and multiple* *radiation exposure can lead to bystander signals that either persist temporarily or permanently. We also found that, in an heterogeneous environment, the size of the domain exposed to radiation and the number of radiation exposures can determine whether a signal will persist temporarily or permanently. Finally, we use sensitivity analysis to identify those cell parameters that affect the signal's lifespan and the signal-induced cell death the most.*

2.1 Introduction

The radiation-induced bystander effect (RIBE) has fascinated scientists since its first report in 1992 by Nagawasa and Little [86]. They observed that even though less than 1% of irradiated cells were actually traversed by an α-particle, about 30% of these cells exhibited radiation effects. At first, RIBE was understood as a secondary effect of radiation on cells exposed to low dose of radiation. These secondary effects of radiation include cell damage, cell death, DNA repair delays and genetic instabilities [95, 94]. More experiments [43] have further described RIBE to also include the induction of radiation-like effects in cells that have not been exposed to radiation at all, but are located near an irradiated region. These *by-standing* cells respond to signals − called bystander signals − emitted by irradiated cells and in turn behave as if they have been directly affected by radiation. In fact, it has been shown that these by-standing cells can influence their neighbours and further transport the bystander signal to more distant places. In exceptional cases, the bystander signal has been reported to persist for 31 years in an atomic bomb victim [91] and it was shown in [51] that irradiating a rat's liver caused a RIBE in its brain and affected the animal's behavior. These experiments suggest that the RIBE can persist for some time and may also have a non-local behavior.

The nature of the bystander signals is still not fully understood and several mechanisms have been discussed in the literature. For example, ionizing radiation produces free radicals which are, in principle, able to cross cell membranes from cell to cell [8]. However, it is believed that free radicals will quickly react with whatever they encounter and they will not survive very long. Hence free radicals are not able to explain the longevity of the bystander signal. Another explanation considers reactive oxygen species, which can also be transported from cell to cell and react with the DNA [8]. These reactive oxygen species have been identified as bystander signal [1]. Since they behave similar to free radicals, they cannot survive very long as well. Recently however, Cytochrome complex has emerged as a new candidate. Cytochrome complex (cyto-c) plays an important role in oxidative phosphorylation as it transports electrons from the cytochrome b-c1 complex (complex II) to the cytochrome oxidase (complex III) just before the ATP-synthase in complex IV. A functioning glycolysis inside a mitochondrion produces energy in the form of ATP, which is essential for the life of the cell. If glycolysis is disrupted, for example due to ionizing radiation, cyto-c might leave the mitochondrion, diffuse through the cell, and interact with other proteins, such as DNA [14]. Since cyto-c is small, it can diffuse, or be transported, to neighbouring cells causing damage to those cells. Cyto-c shows many of the characteristics of a bystander signal, making it a good candidate for further analysis.

In this chapter, we develop a spatially dependent mathematical model for the dynamics of the bystander signal. Since it is not established that cyto-c is the only bystander signal, we will refer to a general bystander signal. However, the model incorporates the bystander dynamics of cyto-c as far as they are known.

After we develop the new bystander model, we fit it to radiation survival data of Joiner et. al. [45]. Joiner et. al. [45], and many others, found that the cell survival is lower than expected for low-dose radiation exposure. This suggests potential risks associated with low-dose radiation exposure, which may have implications for carcinogenesis and radiation protection. In fact, low-dose radiation exposure has been found to be carcinogenic in some cases [60, 41].

The longevity of the bystander signal in tissues has surprised many scientists. Our model allows for a full understanding of the life time of the bystander signal, based on a positive feedback loop. Cells are damaged by radiation, these release cyto-c into the environment, which damages other cells, which releases more cyto-c into the environment. This feedback will not accumulate cyto-c, but it explains the long persistence of enlarged cyto-c levels.

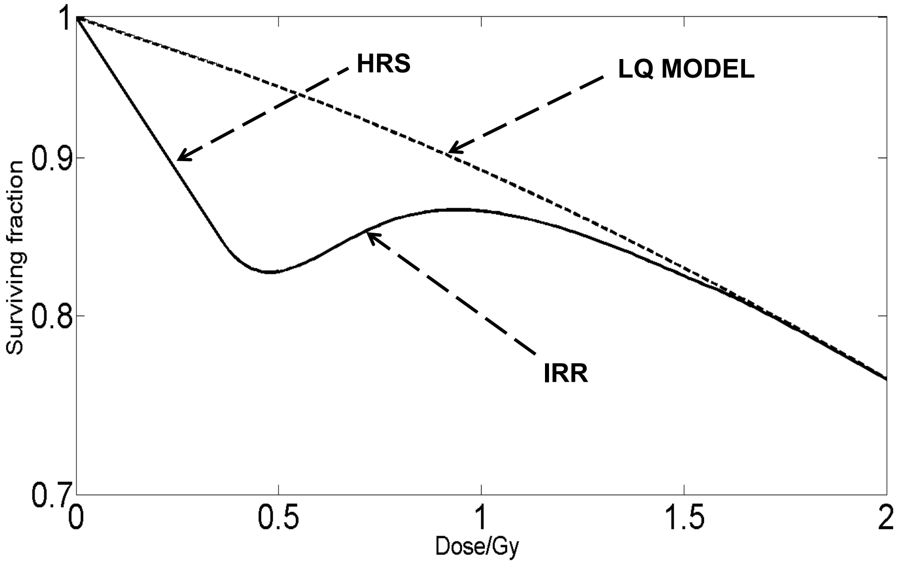

Figure 2.1: Surviving fraction of cells as a function of dose according to linear quadratic model (2.1) (dashed line) and with the HRS/IRR phenomenon (solid line)

The model lets us quantify how much tissue damage is related to direct radiation damage versus indirect bystander damage. Not surprising, we find that for low doses the bystander effect is largest, whereas for larger radiation doses, the direct cell kill dominates. These conclusions have also been found in Powathil et. al. [93] using a computational hybrid model.

The rest of this section will further describe some of the important terminology in this chapter.

2.1.1 Hyper-radiosensitivity (HRS) and increased radioresistance (IRR)

If ionizing radiation is applied to cells, we consider a cell *clonogenically* dead if it is unable to form cell colonies, i.e., it can no longer produce more than 50 offspring. The (clonogenic) surviving fraction (SF) of cells exposed to radiation is defined as the fraction of the irradiated cells that is capable of forming colonies after radiation exposure. A common model for SF of cells is the linear quadratic (LQ) model

$$\mathrm{SF}(d) = e^{-\alpha d - \beta d^2}, \tag{2.1}$$

where d is the radiation dose (measured in Gy), α is the rate at which single radiation tracks produce lethal lesion, and β is the rate at which binary misrepair of pairs of double strand break (DSB) from different radiation tracks lead to lethal lesions [12].

In recent experiments [58, 66, 106, 107, 118], it was shown that cell survival deviates from the LQ model prediction for low-dose radiation in the range of $0.1{-}1$ Gy. We illustrate this difference in Figure 2.1. The measured surviving fraction for low-dose radiation lies significantly below the LQ curve. This phenomenon has been termed low-dose hyper-radiosensitivity (HRS) [45]. The HRS is followed by a period of relative radio-resistance (per unit of dose) of cell kill over the dose range of $\sim 0.5 - 1$Gy. This later phenomenon is referred to as increased radio-resistance (IRR).

We will see that our bystander model can describe the observed hyper-radiosensitivity (HRS) and increased radio-resistance (IRR) effects, making the bystander effect a possible explanation of these phenomena.

2.1.2 Bystander effects

As previously noted, *bystander effects* are secondary effects of radiation either in cells exposed to low dose of radiation or in cells located near an irradiated region [94, 95]. Although most bystander effects are observed in direct proximity of the irradiated region, bystander effects have also been reported quite far from the irradiated region [96, 51]. Here we will focus on the immediate spatial vicinity of an irradiated region.

The *bystander effects* can be roughly classified into [95, 94]:

1. *Bystander signal-induced cell death*
   Bystander signal-induced cell death occurs when the bystander signal interacts with the DNA of a cell to reduce its proliferation capacity to the extent that it can no longer produce more than 50 offspring.

Since bystander signal-induced death may also be other forms of death besides clonogenic death, we will also account for other type of death like apoptosis, necrosis and so on.

2. *Bystander signal-induced cell damage*

   Bystander signal-induced cell damage occurs whenever the bystander signal interacts with the cell's DNA to damage its proliferation capacity but the cell can still produce more than 50 offspring.

3. *Cell repair delay*[2]

   This biological effect occurs when the repair mechanism of damaged DNA of an irradiated cell is interrupted, delayed or completely hindered by the bystander signals [101].

4. *Genetic instability*

   The interaction of the bystander signal with the DNA can also lead to DNA disrepair or mutations. We will not include genetic instabilities in our mathematical model, since these do not contribute to the dynamics of the bystander signal. Mutations might create cancers, or promote cancer development, but this is beyond the scope of this chapter.

As mentioned above, several molecules are discussed as bystander signals, and cyto-c is currently the most convincing candidate. Since this signal can diffuse from cell to cell it is possible that irradiated cells are also affected by the bystander signal. The release of cyto-c after radiation depends on the tumor suppressor gene p53. p53 initiates DNA repair but, at the same time, p53 initiates apoptosis when damage is irreparable. This apoptotic pathway basically involves destruction of mitochondria, releasing cyto-c into the cytoplasm [104, 32, 31, 23]. When cyto-c is released from a damaged cell, it is transmitted either via gap junctions [3] to neighboring cells or it diffuses to neighboring cells [87]. The cyto-c protein can initiate double strand breaks (DSBs) in neighboring cells [49]. These DSBs in neighboring cells also activate p53, which eventually can lead to further release of cyto-c. In this way

---

[2] The word "delay" in a biological context often refers to the fact that a process is slower than normal. It does not necessarily refer to a delay term as would arise in a delay equation.

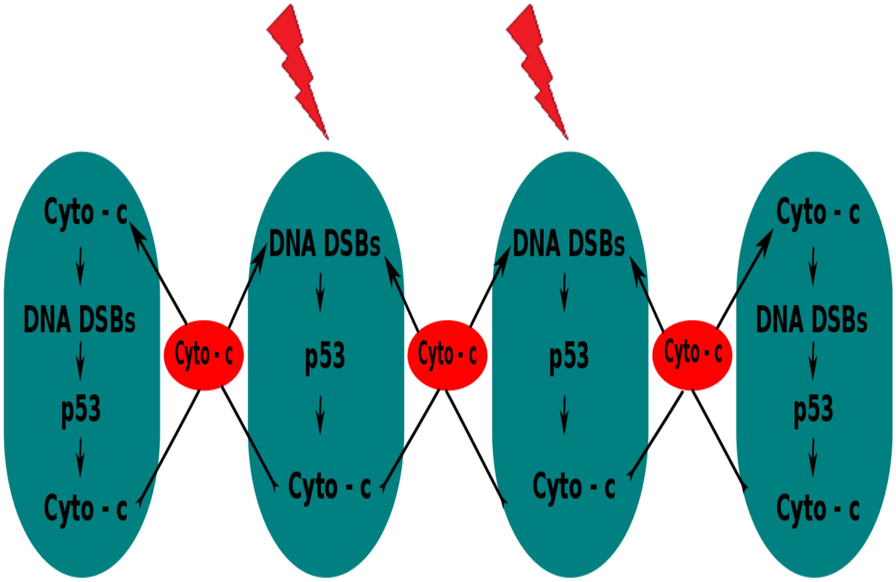

Figure 2.2: p53-induced coupling between irradiated cells and between irradiated and un-irradiated cells. The green ellipsoidal structures represent cells while the lightning symbols indicate radiation.

the cycle continues as illustrated in Figure 2.2 and we can obtain a rather long-lived signal cascade.

2.1.3 Bystander signal's lifespan

Bystander effects have been found in various *in vivo* and *in vitro* experiments to outlive the direct radiation effects. Pant and Kamada [91] reported the presence of bystander signal in the blood plasma of heavily exposed atomic bomb survivors 31 years after exposure. They found the presence of these signals when blood cells of normal individuals exhibited bystander effects when they were cultured with the blood cells of bomb survivors. Similarly, Goyanes-Villaescusa [36] reported the presence of bystander signals in the children born to mothers exposed to radiation several months before conception. These observations have led to an open question regarding “How long does a bystander signal live after its emission?”[10]. Our mathematical model will allow us to address this question in detail. We find that a saddle point in the phase plane of the bystander model is the organizing centre for the longevity of the bystander signal. Orbits pass by a saddle point, hence leading to a long transient.

2.1.4 Previous models of bystander effects

The idea of modelling radiation-induced bystander effects using diffusion-based mechanism began with Khvostunov et. al. [48, 87]. These early models use a quantitative approach that assumes that bystander signal is a protein-like molecule spreading via diffusion. The bystander effects considered are cell death and mutation induction. They assume that bystander effects only occurs in un-irradiated neighboring cells and the bystander response to this signal is assumed to be a binary “on/off” mechanism. They found that their bystander model can explain the experimental data for cell survival and induced oncogenic transformation frequencies. These data also confirm the assumption of the protein-like nature for the bystander signal.

In 2013, McMahon et. al. [75] first modeled the evolution of bystander signal with a partial differential equation (PDE) while a computational model was used to describe bystander cell’s responses. Their model also assumes a binary cell’s response to bystander signal but incorporates the occurrence of bystander effects in the irradiated cells as well. Their model only incorporated bystander signal-induced damage, which is assumed to result into cell death, cell-cycle arrest, or further cell damage. This model suggests that bystander effects play a significant role in determining cellular survival, even in directly irradiated populations.

Most influential to our work is a recent work (2016) by Powathil et. al. [93]. They developed a hybrid multi-scale mathematical and computational model to study multiple radiation-induced bystander effects (bystander signal-induced damage and death, and cell repair delay) on growing tumor within host normal tissue. In their model, the evolution of the bystander signal was described by a PDE, while a stochastic process was used to describe cellular evolution and responses to the signals. They also assumed that both irradiated and un-irradiated cells can respond to the bystander signals. They assumed that bystander signals are emitted by radiation-induced dead and damaged cells. Their model shows that bystander responses play a major role in mediating radiation damage to cells at low-doses of radiation, doing more damage than that due to direct radiation. The survival curves derived from this shows an area of hyper-radio-sensitivity at low-doses that are not obtained using a traditional radio-biological model.

In our model, we use PDE to describe both the dynamics of cells and the signals. In general, we extend most of the assumptions of Powathil et. al. in [93] but in a continuous setting. With the recent discovery of cyto-c as a candidate for the bystander signal, our model is able to incorporate more biologically justifiable assumptions. In particular, we assume that damaged cells do not proliferate since they are expected to be under cell cycle arrest. This assumption was not incorporated in any of the previous models. We also assume that cells which are damaged via bystander signals can also emit bystander signal. This is because DNA damage, irrespective of the cause, can trigger the activity of p53 which eventually leads to the emission of cyto-c as seen in Figure 2.2. The model also assumes that damaged cells emit bystander signals as long as they are not repaired or dead. It is more biological to model cellular response to bystander signal with a continuous functional rather than a discontinuous binary “on/off” mechanism. Finally, both irradiated and un-irradiated cells can exhibit the bystander effects.

Our model agrees with previous results on bystander effects both experimental and theoretical. In particular, our bystander model shows that bystander effects are predominant at low-doses of radiation and it is a major contributor to the phenomenon of hyper-radiosensitivity. Furthermore, we use our model to determine cell parameters that affect this phenomenon the most. Also, we use our model to extensively study how long an emitted signal lives and to show that, although bystander signal is produced at every radiation exposure, it does not increase with increase in radiation exposure. In fact, we found that the concentration converge to a steady state after a couple of exposures.

2.1.5 Outline of the rest of the chapter

In Section 2.2, we formulate and develop the mathematical model, explain the relevant parameters and parameter functions, and present a nondimensionalization of the model. We also fit the model to the radio-sensitivity data of Joiner [45] and estimate the model parameter values as well as their 95% credible intervals. In Section 2.3, we numerically explore the qualitative behavior of the bystander signal profile when cells undergo both single and multiple radiation exposures, respectively, in both homogeneous and heterogeneous domains. The numerical exploration in Section 2.3 shows that the bystander signal can live quite long, hence in Section 2.4 we analyze the bystander signal lifespan. In the analyses on the signal's lifespan in Section 2.4, we perform a phase-plane analysis to identify a saddle point as the organizing centre for the bystander signal dynamics. We also perform a sensitivity analysis to see which parameters have the most impact on the lifespan of the signal. After having gained a good understanding of the bystander dynamics, we analyze the relative significance of the bystander effect on cell survival in Section 2.5. We show that this effect is significant for small radiation doses (0.1−1 Gy), but it is almost irrelevant at larger doses. We finish the chapter with a discussion in Section 2.6.

2.2 The bystander model

2.2.1 Model development

The mathematical model of this paper describes the biological interactions between healthy cells, damaged cells, radiation energy, and bystander signals. We base the model on a typical bystander - *in vitro* assay [43], where cells are cultured on a petri-dish in a monolayer and radiation is applied to a certain partial area of the dish.

A schematic of the model, illustrating the relationship between the components, is given in Figure 2.3. The density of healthy cells is denoted by u, the density of damaged cells by v and the concentration of bystander signal by w. In Figure 2.3, we indicate that a cell exposed to ionizing radiation can either

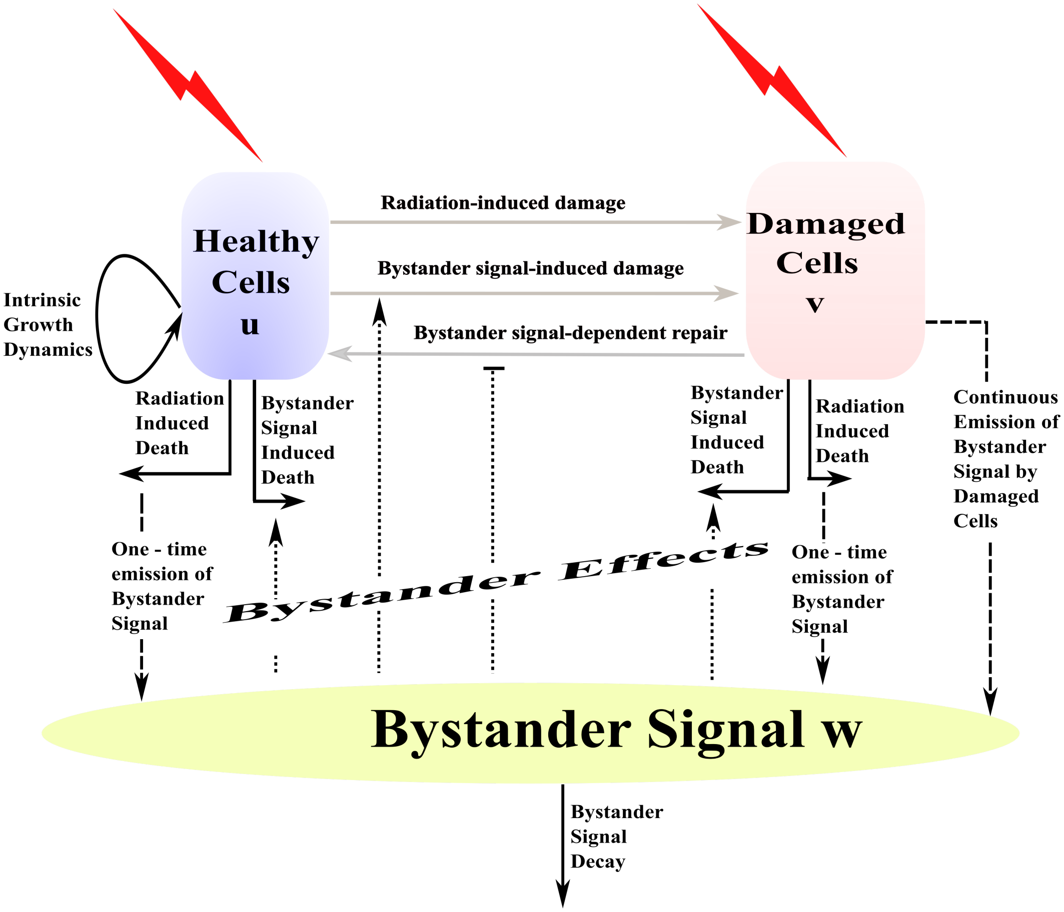

Figure 2.3: Schematics of the bystander signal model. The dotted lines represent the bystander effects, the dashed line represents the bystander signal emission, the grey solid line represent cellular interactions, and the black solid lines represent cellular responses to both radiations and bystander signals. The lightning symbols indicate radiation.

be damaged, or killed, or be completely unharmed and reproduce [59]. After radiation exposure, the fraction of the cells that is damaged by radiation enters the damaged cell compartment v. As suggested by the biology of cyto-c, we assume that radiation-induced damaged cells emit bystander signal as long as they live, while dead cells release bystander signal into the environment once at the time of their death.

Whenever a cell's DNA is damaged, several mechanisms are triggered to repair the damage [101, 2]. Thus, damaged cells have the potential to fully recover and become healthy cells again. The emitted bystander signals, w, provide negative feedback to both the healthy and the damaged cells by causing cell death, cell damage, and DNA repair delay. If a damaged cell is further damaged, then we keep it in the class of damaged cells until it either dies or is repaired. Finally, the bystander signal is produced by dying and damaged cells, it diffuses through the petri dish and it can decay or be cleared out.

To formulate the model mathematically, we denote the number of healthy cells by $u(x,t)$, the number of damaged cells by $v(x,t)$, and the concentration of the bystander signal by $w(x,t)$. Here $x \in \Omega$ denotes the spatial coordinate in a smooth bounded domain $\Omega \subset \mathbf{R}^n$ and $t \geq 0$ denotes time. The model that describes the mutual interactions between $u,\ v,$ and w based on the schematics described in Figure 2.3 is given by:

$$\begin{aligned} u_t &= D_u \Delta u + \mu u\Big(1 - \frac{u+v}{u_0}\Big) - \mathrm{Rad}_u(t)u \\ &\quad -\gamma(t)u - A(w)u + F(w)v - E(w)u, \\ v_t &= D_v \Delta v - \mathrm{Rad}_v(t)v + \gamma(t)u - B(w)v - F(w)v + E(w)u, \\ w_t &= D_w \Delta w + \lambda_1 \mathrm{Rad}_v(t)v + \lambda_2 \mathrm{Rad}_u(t)u + \lambda_3 \kappa v - \eta w, \end{aligned} \tag{2.2}$$

with appropriate boundary conditions depending on the biological situation. For instance, Neumann boundary conditions will be suitable for the petri dish experiment. Details are as follow:

1. In this model, all components are subject to spatial diffusion, expressed through the Laplacians $\Delta u,\ \Delta v,$ and Δw. In case of healthy normal tissue, the diffusion coefficients D_u and D_v might be zero, but if applied to tumor tissue, then D_u and D_v will be nonzero due to local spread of the tumor. Since the signal w can diffuse everywhere, we assume a nonzero diffusion coefficient $D_w > 0$.

2. Healthy cells, u, grow according to a logistic law with carrying capacity, u_0, and growth rate μ.

3. Biological cells respond to radiation exposure in two ways namely: radiation-induced death at rate $\mathrm{Rad}_i(t)$ (for $i = u, v$) and radiation-induced dam-

age at rate $\gamma(t)$. We model the radiation-induced death rate by the radiation hazard function for fractionated radiation [34]

$$\mathrm{Rad}_i(t) \quad = \quad (\alpha + \beta d)\dot{D}(t), \tag{2.3}$$

where d is the dose per fraction, $\dot{D}(t)$ denotes the dose rate (i.e. a piecewise constant jump function), α is the rate at which single radiation tracks produce lethal lesion, and β is the rate at which binary misrepair of pairs of double strand break (DSB) from different radiation tracks lead to lethal lesions [12].

4. To model the radiation-induced damage rate γ, we consider the classical Lethal-Potentially Lethal Model (LPL) of Curtis [22] for radiation damage. As shown in Figure 2.4 (solid curve), the damage rate in the LPL model has a characteristic shape of a steep increase, a single global maximum and a slow decay to zero. We describe this behaviour by the function shown in Figure 2.4 (dotted curve), which is given by

$$\gamma(t) \quad = \quad 2\gamma_0 \frac{\eta \dot{D}(t)}{1 + (\eta \dot{D}(t))^2}. \tag{2.4}$$

   Here γ_0 is the maximum damage rate and $\eta = 1/\dot{D}_{\max}$ denotes the reciprocal of the dose rate $\dot{D}_{\max}$ at which the radiation damage is maximal.

5. The bystander effects in system (2.2) are described by the functions $A(w)$, $B(w)$, $E(w)$, and $F(w)$. The rates $A(w)$ and $B(w)$ denote the bystander signal-induced death rates for healthy and damaged cells, respectively. $E(w)$ denotes the bystander signal-induced damage rate and $F(w)$ denotes the bystander signal-dependent damage repair rate. Mothersill and Seymour suggested in [105, 102] that responses to bystander signals are threshold phenomena. The signal induces a response only when the signal concentration exceeds a lower threshold, and it reaches a maximum response at an upper threshold. All the bystander effects in this chapter will be modeled with two threshold parameters (see Fig-

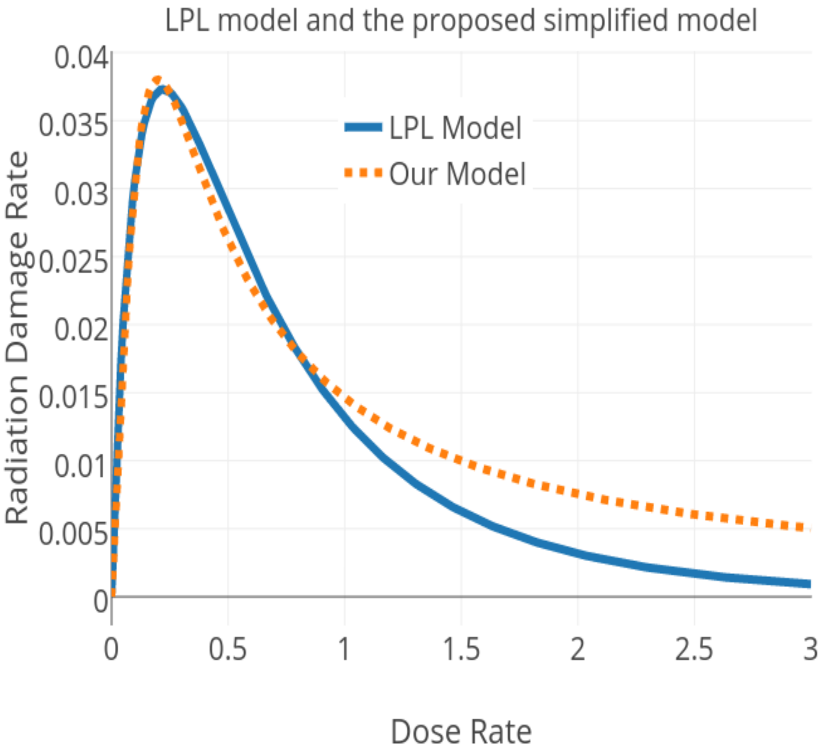

Figure 2.4: The profile of radiation-induced damage rate $\gamma(t)$, according to both the LPL model and our proposed simplified model. The solid line corresponds to the LPL model [22] while the dotted line corresponds to our proposed simplified model for radiation damage rate at $\gamma_0 = 0.038$ and $d_{\max} = 0.2$ Gy.

ure 2.5) using a generic tanh profile:

$$A(w) = \frac{A_0}{2}\Big[1+\tanh\Big(\frac{6}{a_2-a_1}\big(w-\frac{a_1+a_2}{2}\big)\Big)\Big], \tag{2.5}$$

$$B(w) = \frac{B_0}{2}\Big[1+\tanh\Big(\frac{6}{b_2-b_1}\big(w-\frac{b_1+b_2}{2}\big)\Big)\Big], \tag{2.6}$$

$$E(w) = \frac{E_0}{2}\Big[1+\tanh\Big(\frac{6}{e_2-e_1}\big(w-\frac{e_1+e_2}{2}\big)\Big)\Big], \tag{2.7}$$

$$F(w) = \frac{F_0}{2}\Big[1-\tanh\Big(\frac{6}{f_2-f_1}\big(w-\frac{f_1+f_2}{2}\big)\Big)\Big], \tag{2.8}$$

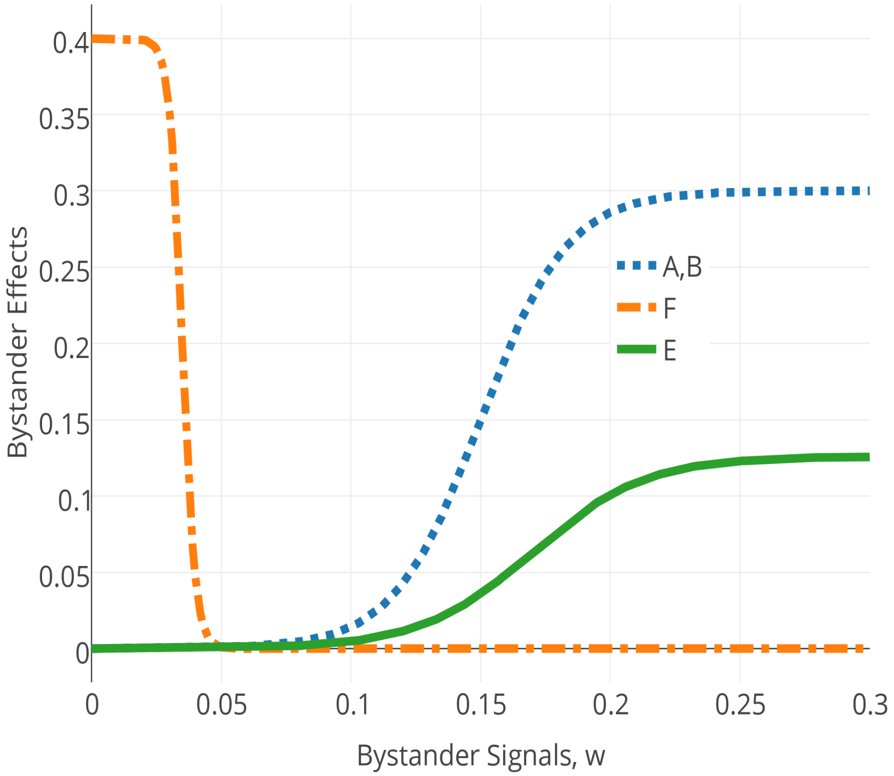

Figure 2.5: Bystander Effects, A, B, E, and F. The parameter values are $a_1 = b_1 = 0.05, a_2 = b_2 = 0.25$ & $A_0 = B_0 = 0.3$ for $A(w)$ and $B(w)$, $f_1 = 0.02, f_2 = 0.05$ & $F_0 = 0.4$ for $F(w)$, $e_1 = 0.04, e_2 = 0.3$ & $E_0 = 0.1333$ for $E(w)$.

These models contain threshold values $a_1 < a_2$, $b_1 < b_2$, $e_1 < e_2$, and $f_1 < f_2$ respectively. The repair rate, $F(w)$, of damaged cells is a decaying function of w, indicating reduced repair capabilities if w exceeds the lower threshold f_1. The above four rate functions are plotted in Figure 2.5.

2.2.2 Rescaling

The bystander signal model (2.2) contains many parameters. The parameters whose values are found in the literature are listed in Table 2.1. The remaining parameters will be estimated from Joiner's data set in the next subsection. However, before we attempt to estimate the parameters, we will rescale the model to carrying capacity $u_0 = 1$ and unit decay rate of the bystander signal.

Parameter	Sym.	Values	Ref.	Re-scaled
Diffusion constant for cells	D_u	$0.001458\text{mm}^2/\text{hr}$	[50]	$1.157e-3$
Diffusion constant for BS	D_w	$0.72\text{mm}^2/\text{hr}$	[4, 75]	0.571
Decay rate for Bystander Signal	η	1.26/hr	[75]	1
Cell's Carrying Capacity	u_0	$7.56e14$Cell/hr	[50]	-
Cell's proliferation rate	μ	0.00666hr^{-1}	[50]	$5.29e-3$
Prop. of signalling damaged cells	κ	0.5	[93]	0.3968
Signal prod. rate of damaged cells	λ_3	0.0066hr^{-1}	[75]	-
Max. rate of BS-induced cell damage	E_0	0.168hr^{-1}	[61]	0.1333
Radiosensitivity (linear)	α	0.11Gy^{-1}	[108]	-
Radiosensitivity (quadratic)	β	0.019Gy^{-2}	[108]	-

Table 2.1: Parameter values available in the literature and their references.

We apply the following transformations

$$u^* := \frac{u}{u_0}, \quad v^* := \frac{v}{u_0}, \quad w^* := \frac{w}{\lambda_3 u_0}, \quad t^* := \eta t, \quad \mu^* := \frac{\mu}{\eta}, \quad A^* := \frac{A}{\eta}, \tag{2.9}$$

$$F_0^* := \frac{F_0}{\eta}, \quad k_i^* := \frac{k_i}{u_0\lambda_3}, \quad a_i^* := \frac{a_i}{u_0\lambda_3}, \quad b_i^* := \frac{b_i}{u_0\lambda_3}, \quad e_i^* := \frac{e_i}{u_0\lambda_3}, \tag{2.10}$$

$$\text{Rad}_i^*(t) := \frac{\text{Rad}_i(t)}{\eta}, \quad D_i^* := \frac{D_i}{\eta}, \quad \kappa^* := \frac{\kappa}{\eta}, \quad \lambda_1^* := \frac{\lambda_1}{\lambda_3}, \quad \lambda_2^* := \frac{\lambda_2}{\lambda_3}, \tag{2.11}$$

to model (2.2) and arrive at the following dimensionless model after dropping the asterisk (*)

$$\begin{aligned} u_t &= D_u\Delta u + \mu u(1-u-v) - \text{Rad}_u(t)u - \ A(w)u - \boldsymbol{\gamma}(t)\ u + F(w)v - E(w)u, \\ v_t &= D_v\Delta v - \text{Rad}_v(t)\ v - B(w)v + \boldsymbol{\gamma}(t)u - F(w)v + E(w)u, \\ w_t &= D_w\Delta w + \lambda_1\text{Rad}_v(t)v + \lambda_2\text{Rad}_u(t)u + \kappa v - w. \end{aligned} \tag{2.12}$$

2.2.3 Parameterizations and data fitting

The parameters that are unknown (see Table 2.2) are mostly parameters such as the bystander effect thresholds which may be difficult to measure directly. Thus, there is the need to accurately estimate their values and a credible interval for each of them, which will form the parameter space for our model.

The data of Joiner et. al. [45] describe the survival of asynchronous T98G human glioma cells irradiated with 240kVp X-rays. These cells were irradiated with single doses of X-ray between 0.05 and 6 Gy at a dose rate of $0.2-0.5$ Gy per min. The surviving fraction of cells following exposure to single doses was measured using a Cell Sorter. Each data point in Figure 2.6 represents between $10-12$ measurements and is denoted as mean ± the standard deviation. Cell survival was described in terms of their ability to form a colony (i.e. reproduce at least 50 offspring after radiation exposure) and cells which are unable to form a colony do not survive.

We employ an implementation of the Goodman and Weare affine invariant ensemble Markov Chain Monte Carlo (MCMC) sampler [35] to fit the model to the dataset in [45]. In particular, we fit the surviving fraction, $\mathrm{SF}(t)$, of irradiated cells at time $t = 6$h computed from the bystander signal model (2.12) to the surviving fraction data [45]. The affine invariance property of this routine enables a much faster convergence even for badly scaled problems. The implementation takes a log-likelihood function of the experimental data and a log-prior of each parameter as input. We assume an exponential distribution for these data. We also assume a uniform distribution for the prior of each parameter over the prescribed intervals of biologically relevant values. The implementation of this MCMC sampler on the bystander signal model results in the fit shown in Figure 2.6. The values of the parameters and their respective 95% credible intervals are given in Table 2.2 below.

We need to reiterate that the parameters estimated are the dimensionless parameters. For example, we will interpret the estimated threshold values in unit of bystander signal per unit of cell's carrying capacity per unit of rate of bystander signal production. The 95% credible intervals of these parameter values will allow for further study of the bystander signal's dynamics via

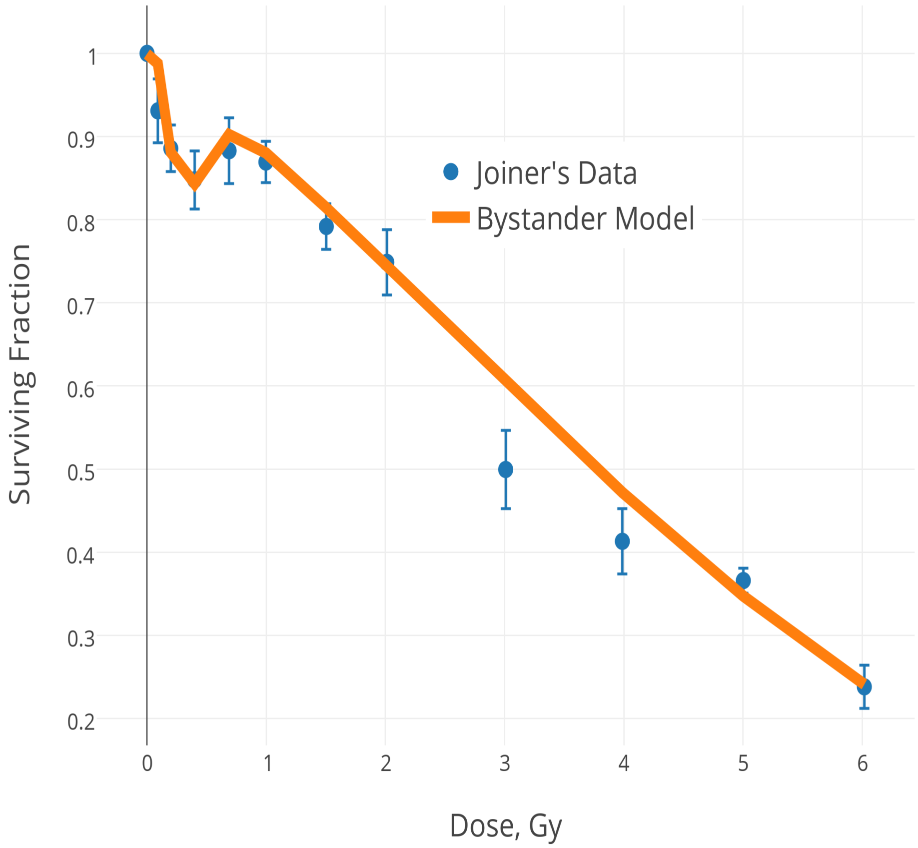

Figure 2.6: Data fitting. The dots with error bars are the data from Joiner et. al. [45] while the solid curve is the best fit from the bystander signal model.

mathematical techniques like bifurcation and sensitivity analyses.

This parameter estimation gives some very useful insight into the parameter relationships between the healthy and damaged cells. For example, the estimation suggests that the bystander signal-induced death rate and the rate of one-time bystander signal emission by radiation-induced dead cells are the same in both the healthy and damaged cells. Thus, we will henceforth assume that $A = B$ and $\lambda_1 = \lambda_2$. This estimation also suggests that the dynamics of the bystander signal is faster than the cellular dynamics. This fact will become important in Section 2.4 as we reduce the system of three PDEs to a system of two ODEs for phase plane analysis.

As noted earlier, this system of three PDEs was motivated by the stochas-

Parameters (thrld= threshold)	Sym.	Est. Values	95% C. I.
Lower thrld. for signal-dependent repair	f_1	0.0128	0.0009 − 0.0284
Lower thrld. for byst. damage in healthy cells	e_1	0.0251	0.0015 − 0.0592
Lower thrld. for byst. death in damaged cells	b_1	0.0254	0.0012 − 0.0600
Lower thrld. for byst. death in healthy cells	a_1	0.0262	0.0017 − 0.0634
Upper thrld. for signal-dependent repair	f_2	0.0327	0.0129 − 0.0546
Upper thrld. for byst. damage in healthy cells	e_2	0.2232	0.0918 − 0.3849
Upper thrld. for byst. death in damaged cells	b_2	0.1881	0.0283 − 0.3914
Upper thrld. for byst. death in healthy cells	a_2	0.1366	0.0245 − 0.2844
Max. rate of signal-dependent repair	F_0	0.5437	0.2642 − 0.8759
Max. rate of Byst. death in damaged cells	B_0	0.6507	0.2559 − 1.1186
Max. rate of Byst. death in undamaged cells	A_0	0.6524	0.2807 − 1.1423
Max. rate of radiation damage	γ_0	1.5027	1.3805 − 1.6208
Rate of signal prod. of dying healthy cells	λ_1	0.0512	0.0027 − 0.1184
Rate of signal prod. of dying damaged cells	λ_2	0.0490	0.0027 − 0.1164

Table 2.2: Parameters and their values estimated using an MCMC sampler.

a_1	a_2	A_0	e_1	e_2	f_1	f_2	F_0	λ_1	γ_0
0.05	0.25	0.3	0.04	0.3	0.02	0.05	0.4	0.016	1.5

Table 2.3: Default parameter set for the simulation in this chapter.

tic spatial model of Powathil et. al. [93]. Thus, in the next section, we will numerically explore this system of PDEs, although much of the qualitative behavior can be captured by the corresponding system of ODEs, as we will show in Section 2.4. The standard parameter set used for all the simulations in this chapter consists of the parameter values found in the literature (which are highlighted in Table 2.1) and the default parameter set in Table 2.3, which is a subset of the dimensionless parameter space (from Table 2.2).

2.3 Numerical exploration of the model

For the numerical exploration of the model (2.12), we choose parameter values from Tables 2.1 and 2.3. We use Matlab to solve system (2.12) on an interval $[0, 1]$ with spatial step $dx = 0.05$ and temporal step $dt = 1/60$ (corresponding to 1 minute). We first consider a single radiation exposure with dose, d, given at the beginning of the simulation, which we incorporate by the dose rate

$$\dot{D}(t) = \begin{cases} \frac{d}{10 \text{ min}} & \text{for } 0 \leq t \leq 10 \text{ min} \\ 0 & \text{for } t > 10 \text{ min.} \end{cases}$$

The dose rate is incorporated into both the hazard function (2.3) and the radiation-induced damage rate (2.4). Since the bystander effects have been found to be more pronounced at low dose of radiation, we will only irradiate at dose $d = 0.2$ Gy.

We will study the profile of a bystander signal in both homogeneous and heterogeneous domains using the model (2.12). A domain is termed homogeneous if every part of the domain is *equally* exposed to radiation, otherwise, it is termed heterogeneous. For simplicity, we will restrict our numerical simulations to a one-dimensional domain. We will assume the initial condition $(1, 0, 0)$, representing cells that are fully grown to its full carrying capacity but have never been previously exposed to radiation. Since we want to study the cellular response at low dose in a petri dish setting similar to [43], it is natural to assume a Neumann boundary condition for all the components. Although the boundary effects on the dynamics of bystander signal are also interesting, we will not consider them in this chapter.

We are also interested in studying the behavior of the system under multiple radiation exposures with each exposure corresponding to a daily dose of 0.2 Gy at 0.02 Gy/min dose rate. Each daily radiation exposure will be referred to as a *fraction*.

2.3.1 Bystander signal profile in a homogeneous domain

The monolayer cells are exposed uniformly to radiation similar to the setup in [43]. Immediately, we observe a rapid production of the bystander signal reaching a maximum shortly after the exposure as illustrated by Fig. 2.7a. Although the signal concentration slowly declines, it seems to converge to some nonzero concentration at $w \simeq 0.0653$. This value is higher than the lower thresholds for all the bystander effects. This suggests that even in the long run, the bystander effects can persist. On the other hand, if the maximum rate of bystander signal-induced death, A_0, in cells is increased to 0.7 as seen in Fig. 2.7b, we observe that the signal concentration is washed out at some later time after radiation exposure. This observation about the dynamics of the signal's lifespan raises the question of 'How long can bystander effects persist in cells after radiation exposure and what are the parameters that affect the dynamics?' We will fully answer this question in Section 2.4 using phase plane and sensitivity analyses.

The profile of the emitted bystander signal is quite different under multiple radiation exposures. At each fraction, there is an increase in the signal's

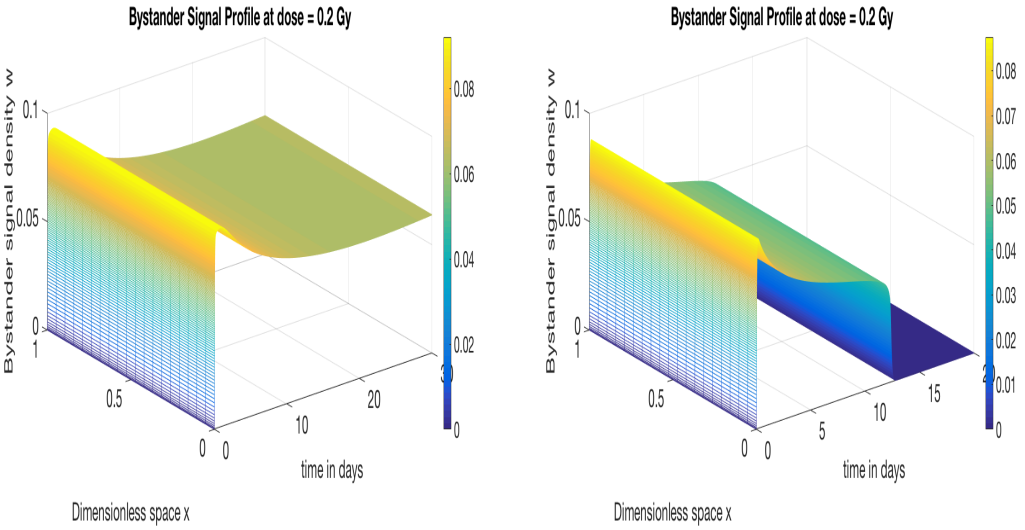

(a) $A_0 = 0.3$ **(b)** $A_0 = 0.7$

Figure 2.7: Bystander signal profiles with single radiation exposure at different values of A_0.

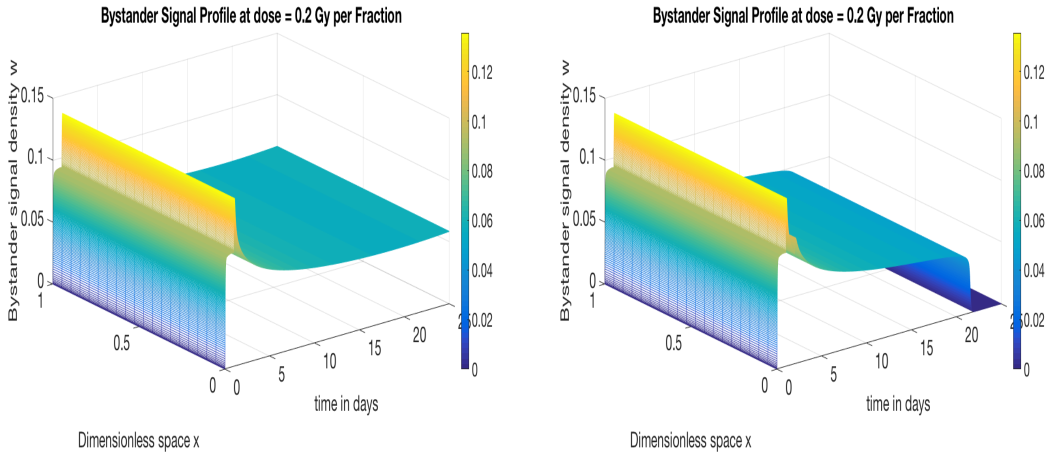

(a) Two fractions. **(b)** Three fractions.

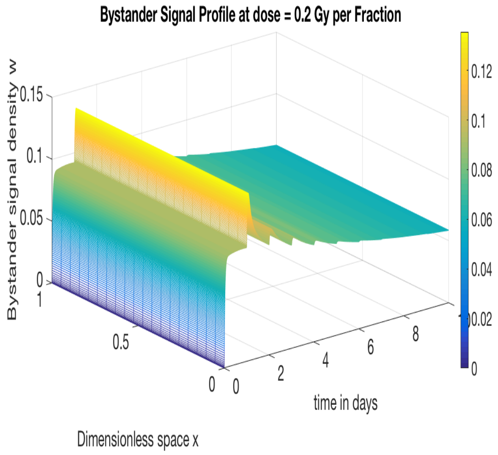

(c) Ten fractions.

Figure 2.8: Bystander signal profiles with multiple radiation exposures at $A_0 = 0.3$.

concentration with the maximum concentration occurring immediately after the second fraction as seen in Fig. 2.8. In fact, further exposure to radiation after about 7 days does not significantly increase the concentration of the signal as seen in Fig. 2.8c.

We noted in Fig. 2.7a that the long-term dynamics of the signal converge to a nonzero concentration at $A_0 = 0.3$. However, at the same parameter value, we observe that after three fractions of radiation exposures, the signal converges to zero. Whereas, the nonzero convergence at $A_0 = 0.3$, is preserved with two fractions as seen in Figure 2.8a. The number of fractions of radiation

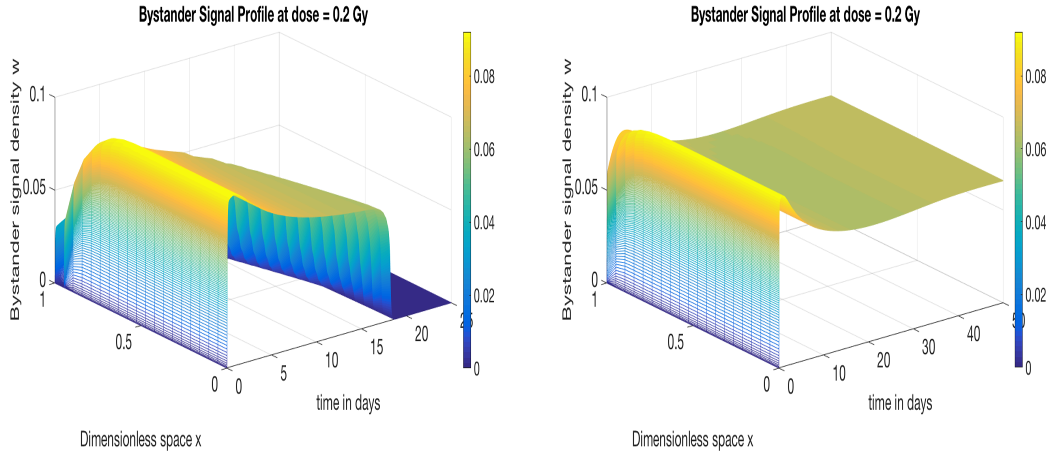

(a) 90% of the domain irradiated. **(b)** 91% of the domain irradiated.

Figure 2.9: Bystander profiles in a single fraction on a heterogeneous domain at $A_0 = 0.3$.

exposure appears to affect the long-term dynamics of the signal. We will try to understand this effect on signal dynamics using phase plane analysis in the following section.

2.3.2 Bystander signal profile in a heterogeneous domain

It is also interesting to study the dynamics of the emitted signal when the cells are not uniformly irradiated. In this subsection, all simulations will be done at $A_0 = 0.3$ unless otherwise stated. Depending on the percentage of the domain exposed to radiation, we observe different dynamics. For instance, when we irradiate $\leq 90\%$ of the domain, even at $A_0 = 0.3$, the signal converges to zero. Figure 2.9a corresponds to the system when 90% of the domain is exposed to radiation. Since the same behavior is seen when less $< 90\%$ of the domain is irradiated we will not include the simulations. On the other hand, we observe that the bystander signal converges to a nonzero value when $\geq 91\%$ of the domain is exposed to radiation as seen in Figure 2.9b. This spatially-driven change in the signal's dynamics is interesting and a rigorous mathematical analysis of this phenomenon is required.

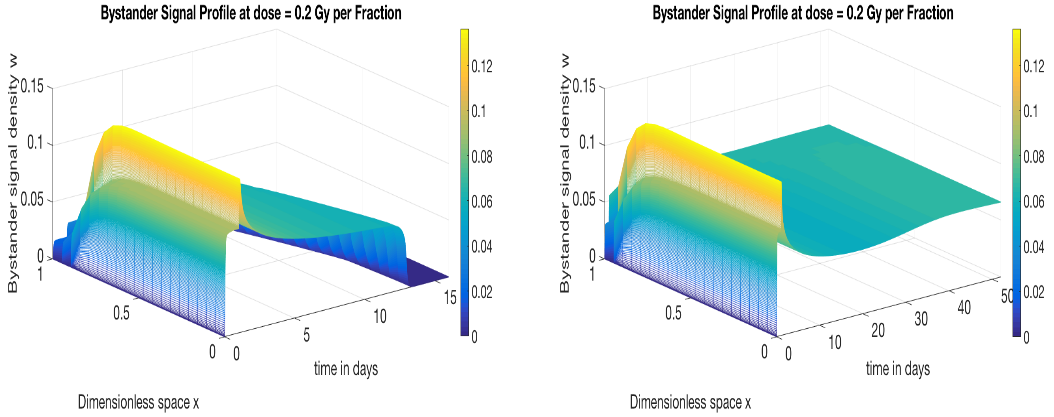

(a) 2 fractions with 85% of the domain irradiated.

(b) 2 fractions with 86% of the domain irradiated.

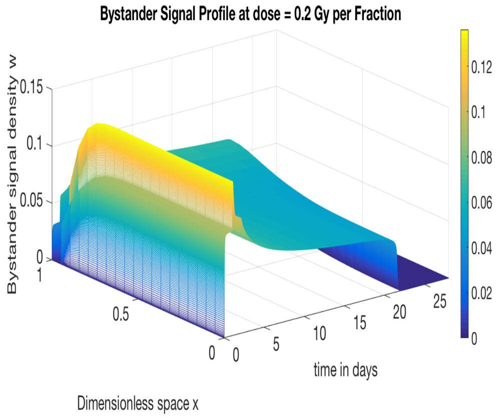

(c) 3 fractions with 86% of the domain irradiated.

Figure 2.10: Bystander signal profiles with fractionated radiation exposure in a heterogeneous domain. All simulations done at $A_0 = 0.3$.

The dynamics of bystander signal with multiple radiation exposures in a heterogeneous domain is very interesting due to its application to radiotherapy. For example, tumor undergoing fractionated radiation treatment is usually surrounded by normal cells. We observe that the bystander signal dynamics changes significantly depending on the number of fractional exposures and the percentage of the domain exposed to radiation.

In Figures 2.10a and 2.10b, we observe the effect of space on the signal dynamics. The signal converges to zero when 85% of the domain is exposed to radiation while the signal converges to a nonzero value when about 86% of the domain is irradiated. We observe this phenomenon as well for a single radiation exposure but with different size of irradiated domain.

In Figures 2.10b and 2.10c, we observe the effect of number of exposures on the dynamics of the signal. Two exposures lead to a convergence to a nonzero steady state while three exposures ensure a complete decay of the signal.

There is the need for further understanding of the effects of the number of fractions and the size of irradiated domain on the qualitative behaviors of the bystander signal, and it is time for a phase plane analysis.

2.4 Analysis of the signal's lifespan in a homogeneous domain

In this section, we will analyze the model to further understand both the zero and the nonzero steady state convergence observed in the previous section as well as the effect of fractional radiation treatment schedules on the signal's dynamics. Since the focus is on a homogeneous domain, we ignore the diffusion terms so that the system of PDEs reduces to a system of ODEs. For the moment, we will focus on a single radiation exposure. Since we are interested in the large-time dynamics of the model, we may view all the radiation terms as a one-time input into the model which can be accommodated into the initial conditions. Then system (2.12) becomes

$$\begin{aligned} \dot{u} &= \mu u(1-u-v) - A(w)u + F(w)v - E(w)u, \\ \dot{v} &= -A(w)v - F(w)v + E(w)u, \qquad (2.13) \\ \dot{w} &= \kappa v - w, \end{aligned}$$

coupled with appropriate initial conditions for $u(t)$, $v(t)$, and $w(t)$, respectively.

We will constrain the initial conditions for the cells to be below their carrying capacity, i.e., $u(0) + v(0) \leq 1$ and consider a very small concentration of bystander signal initially present, i.e., $w(0) \ll \kappa$. These conditions are biologically reasonable for healthy cells because they can not grow beyond their carrying capacity. Under these conditions, the system (2.13) has the following properties:

Theorem 1 (Positivity and Boundedness)**.** *All solutions of the system (2.13) are positive for all time,* t*. Moreover, if* $u_0 = u(0) \geq 0,\ v_0 = v(0) \geq 0$ *and* $w_0 = w(0) \geq 0$*, then*

$$u(t) + v(t) \ \leq \ \frac{u_0 + v_0}{(1 - u_0 - v_0)e^{-\mu t} + u_0 + v_0}. \tag{2.14}$$

Furthermore, if $u_0 + v_0 \leq 1$ *and* $w_0 \leq \kappa$*, then*

$$\begin{aligned} u(t) + v(t) \ &\leq \ 1 \\ w(t) \ &\leq \ \kappa - (\kappa - w_0)e^{-t} \end{aligned}$$

and $w(t) \leq \kappa$*, for all time,* t*.*

Proof. Since

$$\dot{u}|_{u=0} = F(w)v \geq 0, \quad \dot{v}|_{v=0} = E(w)u \geq 0 \quad \text{and} \quad \dot{w}|_{w=0} = \kappa v \geq 0,$$

then all solutions are nonnegative for all time, t.
Let $m = u + v$ and $m_0 = u_0 + v_0$. We have

$$\dot{m} \ = \ \mu u(1 - m) - A(w)m \ \leq \ \mu u(1 - m) \ \leq \ \mu m(1 - m).$$

Thus,

$$m(t) \ \leq \ \frac{m_0}{m_0 + (1 - m_0)e^{-\mu t}}, \tag{2.15}$$

which implies (2.14) and $u + v \leq 1$ if $u_0 + v_0 \leq 1$.

Also, in case of $v \leq 1$,

$$\dot{w} \ = \ \kappa v - w \ \leq \ \kappa - w, \tag{2.16}$$

which implies that

$$w(t) \leq \kappa - (\kappa - w_0)e^{-t}. \tag{2.17}$$

$\square$

An immediate consequence of the above result is given by the following corollary:

Corollary 1 (Forward Invariant Region)**.** *The set*

$$\Gamma \;=\; \{(u,v,w):\; u \geq 0,\; v \geq 0,\; 0 \leq u+v \leq 1,\; 0 \leq w \leq \kappa\} \tag{2.18}$$

defines a forward invariant region of the system (2.13).

The forward invariant region is closed and bounded in $\mathbf{R}^3$; and therefore compact. If we restrict the phase plane to this invariant region, then any trajectory with initial condition in this region will remain in the region for all times. This suggests that the system of three ODEs (2.13) has a global attractor.

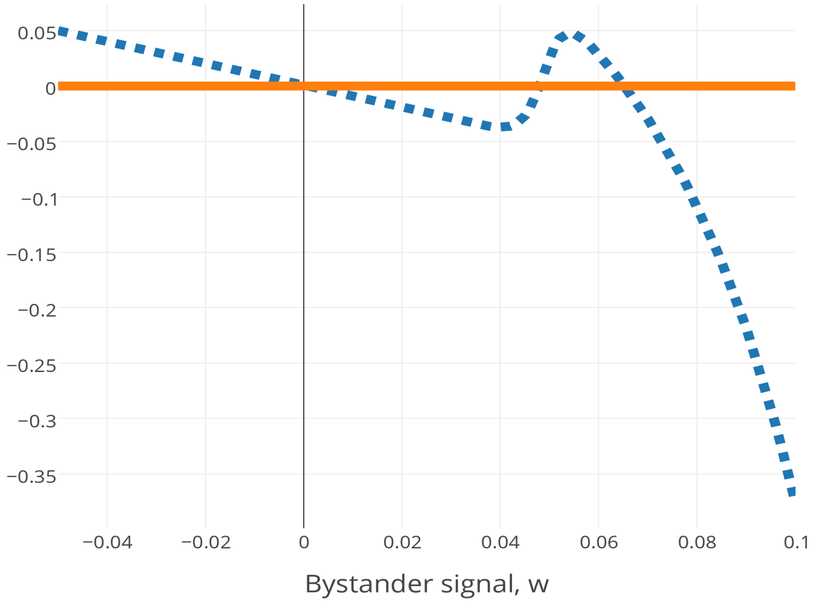

Figure 2.11: The graph of $\Psi(w^*)$ as defined in (2.24) for $A_0 = 0.3$.

We can further reduce this system from three ODEs to two ODEs by simply assuming that the bystander signal's dynamics is faster than cells' dynamics (a fact that was suggested by the data fitting of the model). This implies that $\dot{w} = 0$ and we have

$$w = \kappa v. \tag{2.19}$$

So

$$\dot{w} = \kappa \dot{v} = -A(w)w - F(w)w + E(w)\kappa u. \tag{2.20}$$

Combining eqs. (2.13), (2.19), and (2.20) we derive

$$\begin{aligned} \dot{u} &= \mu u(1 - u - \frac{w}{\kappa}) - A(w)u + F(w)\frac{w}{\kappa} - E(w)u && (2.21) \\ \dot{w} &= -A(w)w - F(w)w + \kappa E(w)u. && (2.22) \end{aligned}$$

2.4.1 Phase plane analysis of the system of two ODEs

The boundary steady states of (2.21)– (2.22) are $(0,0)$ and $(1,0)$. Interior steady states $\left(\frac{A(w^*)+F(w^*)}{\kappa E(w^*)} w^*, w^*\right)$, exist provided $\Psi(w^*) = 0$ and

$$A(w^*)E(w^*) \leq (\mu - A(w^*))(A(w^*) + F(w^*)), \tag{2.23}$$

with

$$\Psi(w^*) = w^* - \kappa E(w^*)\Big[\frac{1}{A(w^*) + E(w^*) + F(w*)} - \frac{A(w^*)}{\mu(A(w^*) + F(w^*))}\Big]. \tag{2.24}$$

A typical form of $\Psi(w^*)$ is shown in Figure 2.11. We observe that (2.24) has up to three zeros (including $w^* = 0$ which is already listed above) which implies that the system admits between two and four steady states depending on the values of model parameters.

The trivial equilibrium, $(0,0)$, is a saddle, and the homogeneous equilib-

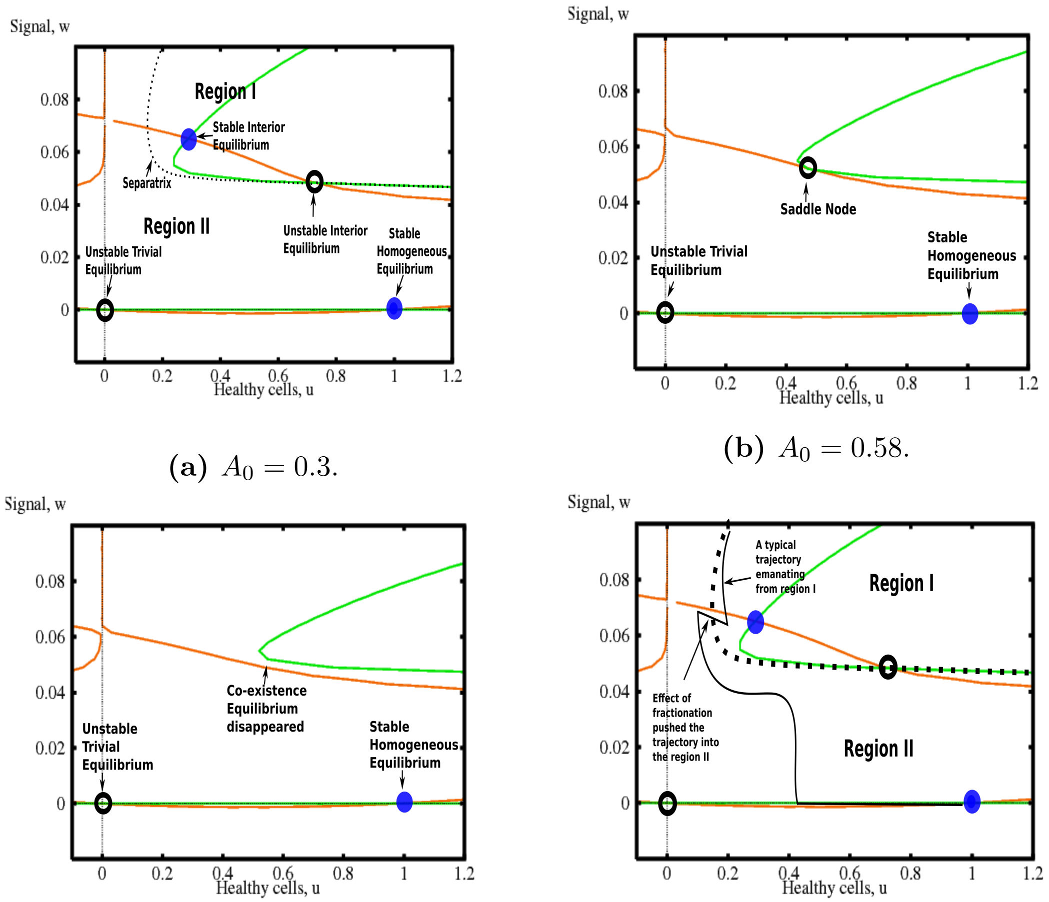

(a) $A_0 = 0.3$.

(b) $A_0 = 0.58$.

(c) $A_0 = 0.7$.

(d) $A_0 = 0.3$

Figure 2.12: Phase plane showing the nullclines of the system (2.21)−(2.22) for three different values of A_0. (a) $A_0 = 0.3$; (b) $A_0 = 0.58$; (c) $A_0 = 0.7$; (d) $A_0 = 0.3$ with a typical trajectory with two radiation exposures.

rium, $(1, 0)$, is a stable node. An interior equilibrium, (u^*, w^*), is stable if

$$\mu\Big(1-u^*(2-\frac{\kappa}{\mu}E')-\frac{w^*}{\kappa}\Big) < 2A+E+F+(A'+F')w^*, \tag{2.25}$$

$$\mu\Big(1-2u-\frac{w}{\kappa}-\frac{1}{\mu}(A-E)\Big)\big(w(A'+F')+(A+F)-\kappa E'u\big) < E\big(\mu u+\kappa u(A'+E')-F-F'w\big). \tag{2.26}$$

Otherwise, (u^*, w^*) is unstable.

The nullclines of the system (2.21)− (2.22) are shown in Figure 2.12 for three different values of the parameter A_0. For $A_0 = 0.3$, the system has two interior equilibria, one of which is a saddle and the other of which is a stable node, as shown in Fig. 2.12a. The stable manifold of the interior saddle equilibrium forms a separatrix (dotted line) that demarcates the basins of attraction of the stable interior steady state and the stable homogeneous steady state, $(1, 0)$, into Region I and Region II, respectively. The interior equilibria coalesce and disappear through a saddle-node bifurcation when the condition in (2.23) is violated at $A_0^* \simeq 0.58$ as shown in Figure 2.12b and 2.12c. For $A_0 > A_0^*$, there are no interior steady state. The homogeneous steady state, $(1, 0)$, is the global attractor in this case. Furthermore, we observe that a trajectory that originates from Region I can be pushed into Region II by a further radiation exposure as seen in Fig. 2.12d. This explains the effect of multiple radiation exposures previously observed in the qualitative behavior of bystander signal profile.

In what follows, we want to make connections between the previous phase plane analysis and the *lifespan* of a bystander signal - which we make more precise in the following.

Definition 1 (Lifespan)**.** *Let f_1, a_1, and e_1 be the lower thresholds of the bystander effects as in Equations (2.5) – (2.8). Let $k = \min\{f_1, a_1, e_1\}$.*

1. *A bystander signal $w(t)$, at time, t, is called active (or inactive) if $w(t) > k$ (or $w(t) < k$).*

2. *Suppose that T is the time at which the bystander signal becomes active, i.e., $w(T) = k$ and $w(t) < k$ for $t < T$. Let*

$$\tau = \inf\{t > T : w(t) \leq k\}$$

be the time at which the signal, $w(t)$, first becomes inactive after time, T. If τ exists, then we define the lifespan of the emitted bystander signal as τ. Otherwise, the lifespan is defined by the host's lifespan.

3. *A bystander signal $w(t)$ is called a transient-state signal if the bystander signal lifespan is finite. Otherwise, it is called a steady-state signal.*

Indeed, any trajectory with initial condition in Region I of Fig. 2.12a converges to the stable interior steady state, while any trajectory with an initial condition in Region II of Fig. 2.12a persists for a while but eventually converges to zero. We can see this clearly illustrated in Fig. 2.13a. This persistence is due to the slow transit along the saddle interior equilibrium, which may take many days. However, as the values of A_0 increases and the homogeneous steady state, $(1, 0)$, becomes the global attractor, we observe that it takes shorter time for trajectories to converge to the homogeneous steady state, $(1, 0)$. This is

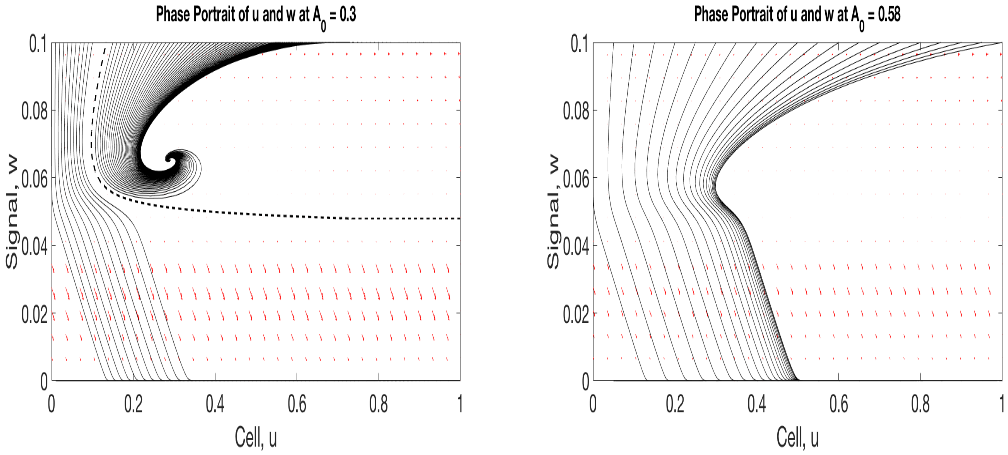

(a) At $A_0 = 0.3$. **(b)** At $A_0 = 0.58$.

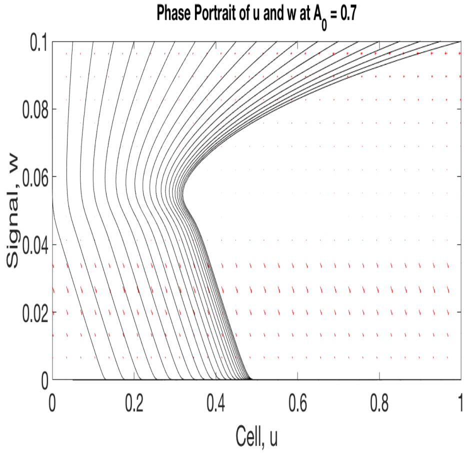

(c) At $A_0 = 0.7$.

Figure 2.13: Phase portrait at different values of A_0. $A_0 = 0.3$; (b) $A_0 = 0.58$; (c) $A_0 = 0.7$.

illustrated in both Figures 2.13b and 2.13c.

2.4.2 Sensitivity analysis of the lifespan of the bystander signal

In this section, we identify parameters that affect the lifespan of the bystander signal the most. We study the normalized sensitivity coefficient $\mathcal{S}_\tau$ of the bystander signal's lifespan, τ, to a parameter p, that is,

$$\mathcal{S}_\tau = \frac{\frac{\partial \tau(p)}{\partial p}}{\frac{\tau(p)}{p}}. \tag{2.27}$$

$\mathcal{S}_\tau$ can be interpreted as the % change in the signal's lifespan per 1% change in the value of a cell's parameter. $\mathcal{S}_\tau$ can be positive or negative indicating that the parameter increases or decreases the lifespan of the signal.

Since we do not have an explicit formula for the signal's lifespan, we estimate $\frac{\partial \tau}{\partial p}$ using the central difference approximation:

$$\frac{\partial \tau}{\partial p} \quad = \quad \frac{\tau(p+\Delta) - \tau(p-\Delta)}{2\Delta p} + \mathcal{O}(\Delta p^2), \tag{2.28}$$

where $\Delta p = 1\%$ of p. The resulting sensitivity indices of the lifespan are summarized in Table 2.4.

The lower threshold for the bystander-induced death in healthy cells, a_1, has the strongest positive relationship to the lifespan of the bystander signal. The positive value suggests that a cell that is highly resistant to signal-induced death, i.e., will emit a longer-lived bystander signal. In contrast to the lower threshold of the signal-dependent repair, f_1, which has the lowest positive sensitivity index, a_1 will be a more important parameter to control in order to reduce the lifespan of an emitted bystander signal.

The upper threshold for the signal-dependent repair, f_2, has the strongest negative relationship to the lifespan of the signal. This is because any increase in f_2 will allow for more repair in the damaged cells and thereby reducing the number of cells emitting the bystander signal. This parameter also is a good

Parameters	$\mathcal{S}_\tau$	
μ	0.3676	Cell's proliferation rate
λ	-0.0028	Rate of one-time signal emission by dead cells
κ	-0.1066	Proportion of damaged cells that are signalling
f_1	0.0337	Lower threshold for signal-dependent repair
f_2	-4.3947	Upper threshold for signal-dependent repair
a_1	4.7595	Lower threshold for byst. death in healthy cells
a_2	0.7577	Upper threshold for byst. death in healthy cells
e_1	-0.9485	Lower threshold for byst. damage in healthy cells
e_2	-0.0898	Upper threshold for byst. damage in healthy cells
A_0	-1.6389	Max. rate of byst. death in healthy cells
E_0	0.5192	Max. rate of bystander signal-induced cell damage
F_0	-0.0730	Max. rate of signal-dependent repair
γ_0	-0.8812	Max. rate of radiation damage

Table 2.4: Sensitivity analysis of the bystander signal's lifespan.

candidate to control in order to reduce the lifespan of an emitted bystander signal.

Parameters such as λ, κ, and γ_0 that enhance the production of bystander signal have negative sensitivity indices. This negative relationship to the signal's lifespan might seem counterintuitive. Since an increase in either λ, κ or γ_0 will lead to an emission of more signals. However, increasing the bystander signal production will also increase the rate of bystander signal-induced death in cells. This in turn leads to the death of damaged cells, which are the emitters of bystander signals, and ultimately leads to a reduction in the lifespan of the signals.

The rate of proliferation, μ, has a positive relationship to the signal's lifespan. This increased proliferation will ensure a quick re-population of cells after radiation exposure. This will in turn yield a consistent increase in the population of the damaged cells via bystander signal-induced damage leading

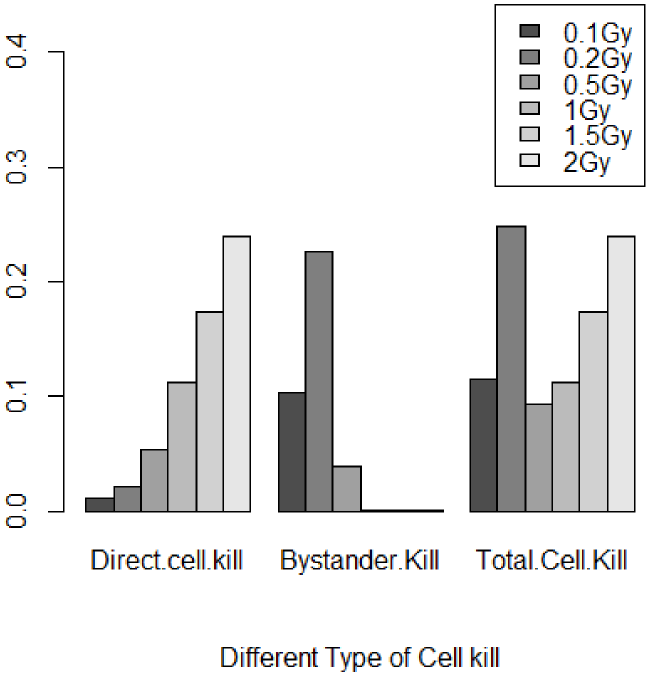

Figure 2.14: Histogram comparing the total cell death, direct radiation-induced death, and bystander signal-induced death, respectively at different doses.

to a longer-lived signal.

Parameters such as e_1, e_2 and F_0 whose increase in value reduce the population of the damaged cells have negative sensitivity indices. This is because reduced concentration of bystander signal will quickly decay due to the threshold-dependent nature of bystander effects.

2.5 Sensitivity analysis of the bystander signal-induced cell death

Bystander signal-induced death is one of the bystander effects in cells that needs to be further understood. Many biological observations and mathematical models have found this bystander effect to be more pronounced with low doses of radiation [78, 93]. Our model exhibit the same behaviour, as illustrated in Figure 2.14. We found that, although the direct radiation-induced death i.e., the direct cell kill, is monotonically increasing with doses, the bystander cell death is non-monotonic. Indeed, we observe more bystander cell death at lower doses than at higher doses. The non-monotonicity of the bystander cell death reflects in the overall effect of radiation, i.e., the total cell kill, where there are more cell death than expected at low doses. This is the phenomenon of hyper-radiosensitivity and increased radio-resistance described in Section 2.1.1. We use sensitivity analysis similar to the one used in the previous section to investigate the cell parameters that affect this bystander cell death the most.

Let $x^*(t)$ be the difference between the cell death at time, t, computed using the full bystander model (2.12) and the cell death at time, t, computed when the bystander signal component of the bystander model is removed. The sensitivity coefficient, $\mathcal{S}_{x^*}$, of the bystander cell death to a parameter, p, is given by

$$\mathcal{S}_{x^*} = \frac{\frac{\partial x^*(p)}{\partial p}}{\frac{x^*(p)}{p}}. \tag{2.29}$$

We will use forward difference to estimate $\frac{\partial x^*(p)}{\partial p}$. The resulting sensitivity indices of the bystander signal-induced cell death are summarized in Table 2.5.

The parameters such as κ, E_0, and γ_0 that enhance the population of the damaged cells all have strong relationships to the bystander signal-induced cell death. This is because increase in bystander signal production will in turn increase the rate of bystander signal-induced death in cells. However, κ has the strongest positive relationship to the bystander signal-induced cell death and will be a more important parameter to control in order to reduce the signal-induced death in cells.

As expected, the signal-induced death in cells increases with increase in the rate of bystander signal-induced death in cells, A_0, as seen in the positivity of its sensitivity index. On the other hand, its lower and upper thresholds, a_1 and a_2, both have negative relationship to the signal-induced death. This is because increase in any of these thresholds will reduce the rate of signal-

Parameters	$\mathcal{S}_{x^*}$	
μ	-0.0366	Cell's proliferation rate
λ	0.0044	Rate of one-time signal emission by dead cells
κ	3.4630	Proportion of damaged cells that are signalling
f_1	-0.1792	Lower threshold for signal-dependent repair
f_2	-0.4733	Upper threshold for signal-dependent repair
a_1	-0.9903	Lower threshold for byst. death in healthy cells
a_2	-0.9699	Upper threshold for byst. death in healthy cells
e_1	-0.3306	Lower threshold for byst. damage in healthy cells
e_2	-0.4946	Upper threshold for byst. damage in healthy cells
A_0	0.4012	Max. rate of byst. death in healthy cells
E_0	0.2220	Max. rate of bystander signal-induced cell damage
F_0	-0.5066	Max. rate of signal-dependent repair
γ_0	2.7417	Max. rate of radiation damage

Table 2.5: Sensitivity analysis of the bystander signal-induced cell death.

induced death in cells, which explains their negative sensitivity indices.

Parameters such as f_1, f_2, e_1, e_2 and F_0 whose increase in value reduces the population of the damaged cells all have negative relationship to the signal-induced death in cells. This is simply because fewer damaged cells will result in lower concentration of emitted signals and in turn result in less bystander effects including the signal-induced cell death.

Lastly, the rate of cell proliferation, μ, has a negative relationship to the signal-induced death in cells. This seems counterintuitive but increase in cell death will reduce the cell's population below their carrying capacity. This population reduction will result in cell repopulation which is even more rapid with cells of high proliferation capacity. This repopulation eventually masks the effect of radiation on cells, especially the secondary radiation effects on cell death.

2.6 Discussion

Radiation-induced bystander signal is a low-dose phenomenon whose effect on cancer radiotherapy and radiation risk can no longer be overlooked. The dynamics presented in this manuscript have many biological implications.

It is interesting to see that the bystander effect model is able to fully explain the observed HRS and IRR phenomena as seen in the fit in Fig. 2.6. This is in perfect agreement with the result of a computational model of Powathil et. al. in [93] and experimental observations of Mothersill and Seymour [83]. Although there are other possible explanations of the HRS/IRR phenomena as well, namely, the cell cycle arrest via the G2-checkpoint [65] and the ATM-independent p53-dependent apoptosis [118]. G2 checkpoint is a regulatory mechanism that prevents damaged G2-phase cells from proceeding to mitosis until the damage is repaired. At low doses, this checkpoint is not quickly activated; and damaged cells entering mitosis without repair eventually undergo apoptosis. This leads to an increased cell death at low doses; and hence the phenomenon of HRS/IRR. ATM-independent p53-dependent apoptosis is the apoptotic pathway that is initiated by the tumor suppressor protein, p53, when a damage is irreparable. This mechanism is similar to the mechanism of Cytochrome Complex, except that bystander signal can also involve molecules or proteins which are not p53-dependent. There has been experimental evidence for these three hypotheses, but it is still not clear which, or in which combination, they contribute to the HRS and IRR; and thus further analysis is required. However, our model shows that bystander effect is an important contributor to the HRS/IRR phenomenon.

The parameter estimation in Section 2.2 computes a 95% credible interval for each parameter value. The credible intervals for the lower thresholds of bystander effects considered in this work (that is, bystander signal-induced cell death, DNA repair delay and bystander signal-induced cell damage) present a possible succession of occurrence of these bystander effects. Proper ordering of the lower bounds of these credible intervals i.e., $f_1 \leq b_1 \leq e_1 \leq a_1$, gives some insight into the possibility of damaged cells experiencing DNA repair delay as the first bystander effect. This is followed by the bystander signal-induced death in the damaged cells, and afterwards, the bystander signal-induced damage and death in the healthy cells population. This sequence suggests that the damaged cells respond to the signals before the healthy cells respond.

In the implementation of affine invariant ensemble MCMC sampler to estimate the model parameters, there may be technical issues such as parameter identifiability. In which case the parameter space in Table 2.2 may not be unique. This problem usually arises as a result of model complexity and/or the sufficiency of the available data. There are standard methods for addressing such issues in literature [92, 13, 115, 72]. We did not investigate this issue in this chapter and it will be a subject of future research.

The question about the lifespan of a bystander signal once it is emitted has been questioned in the literature [10]. Mothersill and Seymour in [78] found that an emitted bystander signal can still cause bystander effects in cells even 60h after its emission. Also, Goyanes-Villaescusa [36] and Pant and Kamada [91] observed that the signal can persist for several months and years, respectively. In our model, we found two interior steady states whose stability are respectively stable and saddle. We also found a stable homogeneous steady state at $(u = 1, w = 0)$. The stable manifold of the saddle interior steady state forms a separatrix that demarcates the basins of attraction of the two stable steady states. We observe that the trajectories that converge to the stable interior steady state provides an explanation for the observation of the presence of bystander signal in cells exposed to radiation several years before. On the other hand, trajectories that converge to the stable homogeneous steady state, $(1, 0)$, pass by the interior saddle point leading to a long persistence.

We found a condition for the existence of the interior steady states in Eqn. (2.11). Although this condition depends on all the bystander effects considered in this work, we also found a dependence on the cell's proliferation capacity, μ. We observe that cells with high values of μ are likely to admit the interior steady states while lower values of μ are unlikely to satisfy Eqn. (2.11). Also, we observe the dependence of the existence of this interior steady states on the values of the bystander effects. In particular, we found the maximum rate, A_0, of bystander signal-induced death as an important bifurcation parameter leading to a saddle node bifurcation. Higher values of A_0 leads to disappearance of the interior steady state while the system admits these interior steady states at lower values.

In the absence of the interior steady state, we found several sensitive parameters that can influence the signal's lifespan. The strongest of these is the lower threshold, a_1, for bystander signal-induced death in cells. This parameter will be very important in controlling the effect of bystander signal. Most importantly, we also observe that highly proliferating cells emit a longer-lived bystander signal. This is also corroborated by the dependence of the condition in Eqn. (2.11) on μ.

The understanding of the signal's behavior in a homogeneous environment with multiple radiation exposures is of great interest since fractionated radiation treatment is a very common treatment strategy for cancer. Our model shows that the bystander signal is being produced immediately after each fraction as seen in Section 2.3. Although the peak of signal concentration does not grow with increase in radiation exposures, the peak of the signal concentration immediately after the second radiation exposure is significantly higher than the rest. We also observe that an increase in radiation exposure can push a trajectory out of the basin of attraction for the stable interior steady state to the basin of attraction of the stable homogeneous steady state. Thus, a further radiation exposure can completely change the behavior of an emitted bystander signal.

Bystander signal dynamics when the domain is partially irradiated is very crucial. This is because tumor cells undergoing radiotherapy are usually surrounded by normal tissues. Under singular and multiple exposures, there seem to be a maximum domain size that needs to be irradiated in order for the signal to die out. We will refer to this as *the maximum domain problem.* Similar to the dynamics in a homogeneous domain, we also observe that further radiation exposure can push a trajectory heading for the stable interior steady state to the basin of attraction of the stable homogeneous steady state. Our simulations reveal that the signal dynamics with more than two fractions will always converge to a zero steady state.

The understanding of the dynamics of the bystander signal cell kill is very interesting to the radiologists in administering low dose of radiation to surrounding normal tissues while the target volume is treated to a high radiation doses. This is usually done in order to reduce radiation toxicity to the surrounding tissues. The sensitivity analysis of the bystander signal cell kill in Section 2.5 shows that the maximum rate, E_0, of radiation damage, the fraction, κ, of damaged cells and the maximum rate, γ_0, of radiation damage are very strongly influential on the bystander signal-induced cell death. Thus, highly resistant cells to radiation damage will also be resistant to the bystander cell kill.

In this chapter, we analyzed some spatial aspects of the model, but additional analysis certainly would be fruitful. In typical radiation treatments, the radiation dose is not applied uniformly over the tumor domain, hence a distinct spatial structure is imprinted. Also, the bystander signal might be transported differently in different types of tissue such as tumor tissue, stroma, blood vessels, collagen networks etc. However, a detailed consideration of such spatial aspects is beyond the scope of this chapter and needs to be left for future research.

Our model incorporated three bystander effects: cell repair delay, bystander signal-induced death and damage. There is the need to incorporate more bystander effects like genetic instabilities, mutation, etc., for more insight and richer understanding of this phenomenon of bystander effects.

Chapter 3

Existence theory and global attractor for the model in Chapter 2

Abstract. *We establish the global existence of weak solutions of the system of reaction-diffusion equations with Neumann boundary condition. This system of equations was developed in Chapter 2 to model the dynamics of radiation-induced bystander effects. The model incorporates different radiation schedules described by time-dependent functions with discontinuous jumps at time points when radiation exposure ends or resumes. In this chapter, we employ mollification and uniform convergence techniques to resolve this inherent temporal discontinuity. We found that the choice of parameter values used for numerical simulations in the previous chapter is a special case of a larger parameter space that support global existence of solutions. Furthermore, we study the asymptotic behavior of solutions at long-time. We prove the asymptotic compactness of solutions and then establish the existence of the global attractor in* $L^2(\Omega)^3$.

3.1 Introduction

In the previous chapter, we formulated a continuum system of reaction-diffusion equations for radiation-induced bystander effects given by

$$\begin{aligned} u_t &= D_u \Delta u + \mu u(1-u-v) - r_u(t)u - A(w)u - \boldsymbol{\gamma}(t)u + F(w)v - E(w)u, \\ v_t &= D_v \Delta v - r_v(t)v - B(w)v + \boldsymbol{\gamma}(t)u - F(w)v + E(w)u, \\ w_t &= D_w \Delta w + \lambda_1 r_v(t)v + \lambda_2 r_u(t)u + \kappa v - w, \end{aligned} \tag{3.1}$$

with Neumann boundary condition:

$$\nabla u(x,t) \cdot \vec{n} \;=\; \nabla v(x,t) \cdot \vec{n} \;=\; \nabla w(x,t) \cdot \vec{n} \;=\; 0, \qquad x \in \partial\Omega, \quad t > 0, \tag{3.2}$$

where Ω is a piecewise smooth domain and $\vec{n}$ is an outer normal vector to its boundary $\partial\Omega$. The initial cell population and signal concentration are given by

$$u(x,0) = u_0(x), \quad v(x,0) = v_0(x), \quad w(x,0) = w_0(x), \qquad x \in \Omega, \tag{3.3}$$

which satisfy the following nonnegative conditions:

$$\min_{x\in\bar{\Omega}} u_0(x) \geq 0, \quad \min_{x\in\bar{\Omega}} v_0(x) \geq 0, \quad \text{and} \quad \min_{x\in\bar{\Omega}} w_0(x) \geq 0.$$

In this dimensionless model, $u(x,t)$ and $v(x,t)$ represent the populations of healthy and damaged cells, and $w(x,t)$ denotes the concentration of bystander signals; at time t and position x. The functionals A, B, E and F represent the bystander effects such as bystander signal-induced death and damage, and bystander signal-dependent repair. The radiation death and damage are denoted by r_i and $\boldsymbol{\gamma}$, respectively. The detailed explanation of the model and a description of its terms can be found in the previous chapter.

In Chapter 2, we numerically explored the model's qualitative behavior, which includes persistent coexistence of cells with bystander signals as well as non-persistent behaviors, where the bystander signal concentration converges to zero steady state. In order to further understand these qualities, we reduced the system of three partial differential equations (PDE) to a system of two ordinary differential equations (ODE), which we then studied using phase plane analysis.

The phase plane analysis of the reduced ODE system showed that the model admits at most four steady states, namely, two boundary and two internal steady states. Depending on the parameter values, the two internal steady states can collapse into a steady state, or disappear due to saddle-node bifurcation. Furthermore, we analytically established the existence of a compact invariant region for the reduced ODE system, which suggests the existence of the global attractor. In this chapter, we want to investigate if the same is true for the full system and establish the existence of the global attractor for the full PDE system (3.1)-(3.3).

Global attractors play an important role in the study of the long-time behavior of solutions of PDEs. Global attractor is a compact subset of the phase space that attracts all the trajectories. As such, we can expect the set of solutions that lie in the attractor to cover all possible 'eventual' dynamical behaviors of the system. Particular attention has been directed to the existence of attractors for a scalar reaction-diffusion equation both in bounded [63, 99] and unbounded domains [116]. Several authors like Conway [21], Smoller [109] and Temam [112] also have investigated the existence of attractors for systems of partial differential equations.

In this chapter, we will proceed by first proving the global existence and the uniqueness of solutions to the system of PDEs, and then investigate the existence of the global attractor for the system. In Robinson [99], the global existence of solutions and the existence of the global attractor for a single reaction-diffusion equation with Dirichlet boundary condition was explored. On the other hand, the biological motivation for our system of PDEs inspires the choice of Neumann boundary condition and we will modify the methods from [99] to establish global existence of solutions and the existence of the global attractor. Much of the mathematical analysis will be made possible by the isomorphism theorems and norm equivalence, which holds up to finite Cartesian products of Banach Spaces.

Furthermore, we noted that the functions modeling the radiation contributions (both damage and death) are discontinuous in time at points when radiation commences and stops. After radiation stops, the system is continuous in time until the next radiation exposure. This intrinsic property of the model will be explored by first establishing the global existence of solutions to the system between radiation exposures. Afterward, we will apply mollification in time and appropriate convergence results to establish the global existence of solutions to the full system in the presence of radiation.

Indeed, we find a parameter regime for which we have the existence of global attractor for the long-time dynamics of model after a radiation exposure. We note that the parameters used in the model simulation in Chapter 2 belong to these parameter regime. The existence of the global attractor suggests that for an appropriate parameter regime, the long-time dynamics of the interactions between the cells and the bystander signals is not affected by intermittent radiation exposure. This was also confirmed numerically in Chapter 2, when the fluctuations in the bystander signal concentration are unaffected by further radiation exposures at long time.

The rest of this chapter is outlined as follows. In Section 3.2, we work with model (3.1)-(3.3) in a vectorized form. We describe some of the properties of various functionals in the model, properties of the the nonlinear reactions term, with and in between radiation exposures, and the positivity of the system in between radiation exposures. In particular, we establish the parameter regime that supports the existence of the global attractor for the model. Some of the classical results that will be applied in this chapter are outlined in Section 3.3. Most of these results also hold in finite Cartesian product of their respective Banach Spaces through norm equivalence in finite dimensional spaces and isomorphism properties. In Section 3.4, we establish the global existence and uniqueness of solutions to the system in between radiation exposures. Similarly in Section 3.5, we establish the global existence and uniqueness of solutions to the system with radiation exposures by employing temporal mollification and relevant uniform convergence properties. In Section 3.6, we only establish the existence of the global attractor for the system in between radiation exposures. The analysis in this section also applies to the case with constant radiation exposure. We conclude with a discussion in Section 3.7.

3.2 Preliminaries

The model (3.1)-(3.3) can be written in the vectorized form given by

$$\begin{cases} z_t = D\Delta z + G_R(z), & (x,t) \in \Omega \times \{t \geq 0\} \\ \nabla z(x,t) \cdot \vec{n} = \mathbf{0}, & (x,t) \in \partial\Omega \times \{t \geq 0\} \\ z(x,\mathbf{0}) = z_0(x), & x \in \Omega. \end{cases} \tag{3.4}$$

where we have denoted

$$z = \begin{pmatrix} u & v & w \end{pmatrix}^T, \ \Delta z = \begin{pmatrix} \Delta u & \Delta v & \Delta w \end{pmatrix}^T, \ D = \operatorname{diag}(D_u, D_v, D_w), \tag{3.5}$$

$$G(z) = \begin{pmatrix} \mu u(1-u-v) - A(w)u + F(w)v - E(w)u \\ -B(w)v - F(w)v + E(w)u \\ \kappa v - w \end{pmatrix}, \tag{3.6}$$

$$R(t,z) = \begin{pmatrix} -r_u(t)u - \gamma(t)u \\ -r_v(t)v + \gamma(t)u \\ \lambda_1 r_v(t)v + \lambda_2 r_u(t)u \end{pmatrix}, \tag{3.7}$$

$$\text{and} \ \ G_R(z) = G(z) + R(t,z). \tag{3.8}$$

The superscript T in equation (3.5) denote vector transpose.

Consequently, the interaction in between cells and bystander signals between radiation exposures is governed by

$$\begin{cases} z_t = D\Delta z + G(z), & (x,t) \in \Omega \times \{t \geq 0\} \\ \nabla z(x,t) \cdot \vec{n} = \mathbf{0}, & (x,t) \in \partial\Omega \times \{t \geq 0\} \\ z(x,\mathbf{0}) = z_0(x), & x \in \Omega. \end{cases} \tag{3.9}$$

3.2.1 Properties of the model's parameters

P1: The radiation terms $r_{u,v}(t)$ and $\gamma(t)$ are piecewise continuous and bounded functions: there exists $r_1 > 0, \gamma_0 > 0$, such that $0 \leq r_{u,v}(t) \leq r_1$ and $0 \leq \gamma(t) \leq \gamma_0$, for all $t > 0$. In applications, we typically have $r_j(t) = r_j(d(t))$, $j = u, v$ where $d(t)$ denotes the total dose over time, t.

For $T_1 > 0$, let

$$\underline{r}_i := \min_{0 \le t \le T_1} r_i(t),\ \overline{r}_i := \max_{0 \le t \le T_1} r_i(t),\ \underline{\gamma} := \min_{0 \le t \le T_1} \gamma(t),\ \overline{\gamma} := \max_{0 \le t \le T_1} \gamma(t)$$

P2: The bystander response functions $A(w), B(w), E(w), F(w)$ are monotonic and bounded C^∞ functions such that there exist positive constants $A_0,\ B_0,\ E_0$, and F_0 satisfying $0 < A(w) \le A_0$, $0 < B(w) \le B_0$, $0 < E(w) \le E_0$, and $0 < F(w) \le F_0$. A, B, and E are increasing and F is decreasing

P2*: Consequently, there exist nonnegative constants $A_{10},\ B_{10},\ E_{10}$, and negative constant F_{10} such that for all $w > 0$, we have $0 \le A'(w) \le A_{10}$, $0 \le B'(w) \le B_{10}$, $0 \le E'(w) \le E_{10}$, and $F_{10} \le F'(w) \le 0$.

P3: For a given $\epsilon > 0$ we denote by $w_0^* > 0$ a constant such that

$$A(w) \ge A_0 - \epsilon := A_1, \quad \forall w \ge w_0^*, \tag{3.10}$$

$$E(w) \ge E_0 - \epsilon := E_1, \quad \forall w \ge w_0^*, \tag{3.11}$$

$$B(w) \ge B_0 - \epsilon := B_1, \quad \forall w \ge w_0^*, \tag{3.12}$$

$$2\epsilon \ge F(w) \ge 0, \quad \forall w \ge w_0^*. \tag{3.13}$$

We will focus on the properties of the nonlinear reaction term $G(z)$ in the next subsection.

3.2.2 Properties of the nonlinear term $G(z)$

Theorem 2 (Positivity). *Suppose the initial data $z_0(x) \ge 0\ \forall x \in \bar{\Omega}$ then any classical solution $z(x,t)$ to the system (3.9) is nonnegative* $\forall (x,t) \in \bar{\Omega} \times (0, \infty)$.

Proof. By inspection, we see that $(G(z))_1 \ge 0$ for $u = 0$, $(G(z))_2 \ge 0$ for $v = 0$, and $(G(z))_3 \ge 0$ for $w = 0$, where the index 1,2,3 denotes the components of G. Since Δ with homogeneous Neumann boundary condition is uniformly parabolic and G is C^1 in z; and Hölder continuous in x and t. The result follows from a comparison theorem in Theorem 10.1 [109]. $\square$

Theorem 3. *Assume (P1)-(P3) hold. Suppose*

$$\kappa^2 < B_1 - \frac{E_0}{2}, \tag{3.14}$$

then there exist positive constants M and k_2 such that

$$G(z) \cdot z \leq M - k_2 |z|^2. \tag{3.15}$$

Proof.

$$\begin{aligned} G(z) \cdot z &= \mu u^2 - \mu u^3 - \mu u^2 v - A(w) u^2 - E(w) u^2 + F(w) uv \\ &\quad - \big(B(w) + F(w)\big) v^2 + E(w) uv + \kappa v w - w^2 \end{aligned}$$

Using property (P3) above, we have

$$\begin{aligned} G(z) \cdot z &\leq \mu u^2 - \mu u^3 - \mu u^2 v - A_1 u^2 - E_1 u^2 + 2\epsilon uv - B_1 v^2 \\ &\quad + E_0 uv + \kappa v w - w^2 + M, \end{aligned}$$

where

$$M = \max\{G(z) \cdot z : 0 \leq w \leq w_0^*,\ 0 \leq u, v \leq 1\} \tag{3.16}$$

Young's inequality implies that

$$\begin{aligned} G(z) \cdot z &\leq -\mu u^2 (u - 1 + v) - \big(A_1 + E_1 - \frac{E_0}{2}\big) u^2 \\ &\quad - \big(B_1 - \frac{E_0}{2} - \kappa \epsilon_0\big) v^2 - (1 - \frac{\kappa}{\epsilon_0}) w^2 + M \\ &\leq -\Big[\mu(u - 1 + v) + A_1 + E_1 - \frac{E_0}{2}\Big] u^2 \\ &\quad - \big(B_1 - \frac{E_0}{2} - \kappa \epsilon_0\big) v^2 - \big(1 - \frac{\kappa}{\epsilon_0}\big) w^2 + M. \end{aligned}$$

By the condition (3.14), if we choose $\epsilon_0 > 0$ such that $\kappa^2 < \epsilon_0 < B_1 - \frac{E_0}{2}$ then

$B_1 - \frac{E_0}{2} - \kappa\epsilon_0$ and $1 - \frac{\kappa}{\epsilon_0}$ are positive. If

$$k_2 := \min\big\{\mu(u-1+v) + A_1 + E_1 - \frac{E_0}{2},\ B_1 - \frac{E_0}{2} - \kappa\epsilon_0,\ 1 - \frac{\kappa}{\epsilon_0}\big\},$$

then we have

$$G(z)\cdot z \le M - k_2|z|^2,$$

and the proof is complete. □

We note that condition (3.14) is satisfied by the choice of parameter values:

$$\kappa = 0.3968,\ E_0 = 0.1333,\ B_1 \approx 0.3,\ \epsilon = 0$$

that was used in Chapter 2. The condition in (3.14) suggests that the rate of bystander production κ, in the absence of radiation exposure, is less than the maximum rate of bystander signal-induced death B_1. Later on we will see that this condition is also necessary for the global existence of weak solutions to the system of PDEs (3.9) when the reaction term is $G(z)$.

The following result shows that each component of $G(z)$ is linearly bounded.

Lemma 1. *Suppose $u, v, w > 0$, there exist positive M_{1i} and M_{2i}, such that, for each $i \in \{1, \dots, 3\}$,*

$$(G(u,v,w))_i \le M_{1i} + M_{2i}(u+v+w). \tag{3.17}$$

Proof. Using properties (P2)-(P3), let

$$M_{2i} := \{(G(z))_i : 0 < u, v < 1, 0 < w < w_0^*\}.$$

For the first entry,

$$\begin{aligned}(G(u,v,w))_1 &= \mu u(1-u-v) - A(w)u + F(w)v - E(w)u \\ &\le \mu u(1-u-v) - A_1 u + 2\epsilon v - E_1 u + M_{11} \\ &\le -(A_1 + E_1)u + 2\epsilon v + M_{11}.\end{aligned}$$

Thus, if $M_{22} = 2\epsilon$, then

$$(G(u,v,w))_1 \;\leq\; M_{22}(u+v) + M_{11}.$$

For the second entry,

$$\begin{aligned} (G(u,v,w))_2 &= -B(w)v - F(w)v + E(w)u \\ &\leq -(B_1 + 2\epsilon)v + E_0 u + M_{13} \\ &\leq M_{23}(v+w) + M_{13}, \end{aligned}$$

where $M_{23} = \kappa$.

For the third entry,

$$\begin{aligned} (G(u,v,w))_2 &= \kappa v - w \\ &\leq \kappa v - w + M_{13} \\ &\leq M_{13}(u+v) + M_{12}, \end{aligned}$$

where $M_{12} = E_0$. □

In order to establish the local Lipschitz property of $G(z)$, it suffices (in conjunction with Lemma 1) to show that the derivative of $G(z)$ is at least linearly bounded.

Lemma 2. *Consider $G(z)$ given by (3.6). The derivative of $G : \mathbf{R}^3_+ \to \mathbf{R}^3$, denoted by $DG(z)$, has the following upper bound: There exist positive constants M_0 and M_1 such that*

$$|DG(z)| \leq M_0 + M_1|z|. \tag{3.18}$$

Proof. The Jacobian matrix of $G(z)$ is given by

$$DG(z) = \begin{pmatrix} \mu(1-2u-v) - A(w) - E(w) & -\mu u + F(w) & -A'(w)u + F'(w)v - E'(w)u \\ E(w) & -B(w) - F(w) & -v(B'(w) + F'(w)) + E'(w)u \\ 0 & \kappa & -1 \end{pmatrix}.$$

Using $L1$ norm, we have

$$
\begin{aligned}
|DG(z)| &= |\mu(1-2u-v) - A(w) - E(w)| + |-\mu u + F(w)| \\
&\quad + |-A'(w)u + F'(w)v - E'(w)u| + |E| + |-B-F| \\
&\quad + |-v(B'+F') + E'u)| + \kappa + 1 \\
&\le |\mu(1-2u-v) - A_1 - E_1| + |-\mu u + F_0| \\
&\quad + |-A'(w)u + F'(w)v - E'(w)u| + E_0 + B_0 + F_0 \\
&\quad + |-v(B'(w) + F'(w)) + E'(w)u| + \kappa + \\
&\le \mu + 3\mu|u| + \mu|v| + A_1 + E_1 + E_0 + B_0 + 2F_0 \\
&\quad + |-A'(w)u + F'(w)v - E'(w)u| + \kappa + 1 \\
&\quad + |-v(B'(w) + F'(w)) + E'(w)u| \\
&\le \mu + 3\mu|u| + \mu|v| + A_1 + E_1 + E_0 + B_0 + 2F_0 \\
&\quad + (A_{10} + E_{10})|u| + F_{10}|v| + E_{10}|u| + \kappa + 1 \\
&\quad + (B_{10} + F_{10})|v| + E_{10}|u| \\
&\le M_0 + (3\mu + A_{10} + 3E_{10})|u| + (\mu + 2F_{10} + B_{10})|v| \\
&\le M_0 + M_1|z|,
\end{aligned}
$$

where

$$
\begin{aligned}
M_0 &:= \mu + A_1 + E_1 + E_0 + B_0 + 2F_0 + \kappa + 1 \\
M_1 &:= \max\{3\mu + A_{10} + 3E_{10}, \mu + 2F_{10} + B_{10}\}.
\end{aligned}
$$

The first inequality holds by applying properties (P2) and (P3), and the third inequality holds from the property (P2*). □

The following useful corollary will be handy after the boundedness of z has been established. In fact, we will only use it to establish the uniqueness of a bounded solution.

Corollary 2. *Suppose that there exists a positive constant M_2 such that $|z| < M_2$, then*

$$|DG(z)| \le M,$$

for some $M > 0$.

Proof. The result follows directly from Lemma 2 by noting that $|z| < M_2$ and setting $M = M_0 + M_1 M_2$. $\square$

This corollary implies that each component of the matrix $DG(z)$ is finite for bounded z.

In the next subsection, we will focus on the properties of the full nonlinear reaction term $G_R(z)$.

3.2.3 Properties of the nonlinear term $G_R(z)$

Similar to Theorem 3, we can prove the same result for the reaction term $G_R(z)$ as follows:

Theorem 4. *Suppose* $\frac{\kappa}{2} < \min\left\{B_1,\ 1 - \lambda_2 \frac{\overline{r}_u}{2} - \lambda_1 \frac{\overline{r}_v}{2}\right\}$. *If*

$$\frac{(\overline{\gamma} + E_0)^2}{2(\mu + A_1 + E_1 + \underline{\gamma} - \epsilon + \underline{r}_u) - \lambda_2 \overline{r}_u} < 2(B_1 - \epsilon + \underline{r}_v) - \kappa - \lambda_1 \overline{r}_v \tag{3.19}$$

then under the assumptions (P1)-(P3), there exist positive M *and* k_2 *such that*

$$G_R(z) \cdot z = M - k_2 |z|^2. \tag{3.20}$$

Proof.

$$\begin{aligned}
G_R(z) \cdot z \;&=\; \mu u^2 - \mu u^3 - \mu u^2 v - r_u(t) u^2 - \gamma(t) u^2 - A(w) u^2 \\
&\quad - E(w) u^2 + F(w) uv - r_u(t) v^2 + \gamma(t) uv \\
&\quad - \big(B(w) + F(w)\big) v^2 + E(w) uv + \lambda_1 r_u(t) vw \\
&\quad + \lambda_2 r_u(t) uw + \kappa vw - w^2 \\
&\le\; - u^2 \Big[\mu(u + v - 1) + r_u(t) + A_1 + E_1 + \gamma(t)\Big] \\
&\quad - v^2 \big(r_v(t) + B_1\big) + \big(2\epsilon + \gamma(t) + E(w)\big) uv \\
&\quad + \lambda_1 r_u(t) vw + \lambda_2 r_u(t) uw + \kappa vw - w^2 + M,
\end{aligned}$$

where the last inequality is due to property (P3) and M is defined as

$$M = \max\{G_R(z,t)\cdot z : 0 \le w \le w_0^*,\ 0 \le u, v \le 1,\ 0 < t < T\} \tag{3.21}$$

Young's inequality implies that

$$\begin{aligned} G_R(z)\cdot z \ \le\ & -u^2\Big[\mu(u+v-1) + r_u(t) + A_1 + E_1 \\ & + \gamma(t) - \epsilon - \frac{\gamma(t)}{2\epsilon_0} - \frac{E_0}{2\epsilon_0} - \lambda_2\frac{r_u(t)}{2}\Big] \\ & - v^2\Big[r_v(t) + B_1 - \frac{\epsilon_0\gamma(t)}{2} - \epsilon - \frac{\epsilon_0 E_0}{2} - \lambda_1\frac{r_u(t)}{2} - \frac{\kappa}{2}\Big] \\ & - w^2\Big[1 - \lambda_2\frac{r_u(t)}{2} - \lambda_1\frac{r_v(t)}{2} - \frac{\kappa}{2}\Big] + M \\ \le\ & -u^2\Big[\mu(u+v-1) + r_u(t) + A_1 + E_1 + \gamma(t) \\ & - \epsilon - \frac{\gamma(t)}{2\epsilon_0} - \frac{E_0}{2\epsilon_0} - \lambda_2\frac{r_u(t)}{2}\Big] \\ & - v^2\Big[r_v(t) + B_1 - \frac{\epsilon_0\gamma(t)}{2} - \epsilon - \frac{\epsilon_0 E_0}{2} - \lambda_1\frac{r_u(t)}{2} - \frac{\kappa}{2}\Big] \\ & - w^2\Big[1 - \lambda_2\frac{r_u(t)}{2} - \lambda_1\frac{r_v(t)}{2} - \frac{\kappa}{2}\Big] + M \\ \le\ & -u^2\Big[\mu(u+v-1) + \underline{r}_u + A_1 + E_1 + \underline{\gamma} \\ & - \epsilon - \frac{\overline{\gamma}}{2\epsilon_0} - \frac{E_0}{2\epsilon_0} - \lambda_2\frac{\overline{r}_u}{2}\Big] \\ & - v^2\Big[\underline{r}_v + B_1 - \frac{\epsilon_0\overline{\gamma}}{2} - \epsilon - \frac{\epsilon_0 E_0}{2} - \lambda_1\frac{\overline{r}_u}{2} - \frac{\kappa}{2}\Big] \\ & - w^2\Big[1 - \lambda_2\frac{\overline{r}_u}{2} - \lambda_1\frac{\overline{r}_v}{2} - \frac{\kappa}{2}\Big] + M, \end{aligned}$$

where the last inequality is as a result of property (P1). Let

$$\begin{aligned} A_{11} &:= \mu(u+v-1) + \underline{r}_u + A_1 + E_1 + \underline{\gamma} - \epsilon - \frac{\overline{\gamma}}{2\epsilon_0} - \frac{E_0}{2\epsilon_0} - \lambda_2\frac{\overline{r}_u}{2} \\ B_{11} &:= \underline{r}_v + B_1 - \frac{\epsilon_0\overline{\gamma}}{2} - \epsilon - \frac{\epsilon_0 E_0}{2} - \lambda_1\frac{\overline{r}_u}{2} - \frac{\kappa}{2} \\ C_{11} &:= 1 - \lambda_2\frac{\overline{r}_u}{2} - \lambda_1\frac{\overline{r}_v}{2} - \frac{\kappa}{2}. \end{aligned}$$

Since

$$A_{11} \geq \mu + \underline{r}_u + A_1 + E_1 + \underline{\gamma} - \epsilon - \frac{\overline{\gamma}}{2\epsilon_0} - \frac{E_0}{2\epsilon_0} - \lambda_2 \frac{\overline{r}_u}{2},$$

if we choose positive ϵ_0 such that

$$\frac{\overline{\gamma} + E_0}{2(\mu + A_1 + E_1 + \underline{\gamma} - \epsilon + \underline{r}_u) - \lambda_2 \overline{r}_u} < \epsilon_0 < \frac{2(B_1 - \epsilon + \underline{r}_v) - \kappa - \lambda_1 \overline{r}_v}{\overline{\gamma} + E_0}$$

then A_{11} and B_{11} are positive. If $k_2 := \min\big\{A_{11}, B_{11}, C_{11}\big\}$, then we have $G_R(z) \cdot z \leq M - k_2|z|^2$, and the proof is complete. □

Condition (3.19) implies that the damage incurred through bystander and radiation damage during a radiation event is less than the bystander death incurred in both damaged and healthy cells. Notice that this condition still holds when $\overline{\gamma} = \overline{r}_{u,v} = 0$. It will be interesting to estimate the maximum values of the radiation terms that satisfy the condition. For simplicity, we will denote

$$\begin{aligned} L_0 &:= 2E_0, \\ L_1 &:= E_0^2 - \Big[(2B_1 - \kappa - 2\epsilon - \lambda_1 \overline{r}_v)\Big]\Big[2(\mu + A_1 + E_1 - \epsilon) - \lambda_2 \overline{r}_u\Big]. \end{aligned} \tag{3.22}$$

Corollary 3. *Suppose $L_1 < 0$. There exists a bound for $\overline{\gamma}$ for which condition (3.19) holds. In fact,*

$$0 \leq \overline{\gamma} \leq \frac{1}{2}\Big\{ - L_0 + \sqrt{L_0^2 - 4L_1}\Big\},$$

where L_0 and L_1 are as defined in (3.22).

Proof. Let $x = \overline{\gamma}$, then from (3.19) we have $\mathbf{F}(x) := x^2 + xL_0 + L_1 < 0$. If we can show that $\mathbf{F}(x)$ has a minimum between its two zeros, then we are done. Indeed, the zeros of $\mathbf{F}(x)$ are $\frac{1}{2}\big\{ - L_0 \pm \sqrt{L_0^2 - 4L_1}\big\}$ and its attains a minimum at $x = -\frac{L_0}{2}$. This implies that $\mathbf{F}$ attains a minimum (which is negative) between its zeros. If $L_1 < 0$ then $\mathbf{F}$ will be negative for all values in the interval $\big(0, \frac{1}{2}\big\{ - L_0 + \sqrt{L_0^2 - 4L_1}\big\}\big)$ and the proof is complete. □

Since we are dealing with a system of nonlinear parabolic equations in this chapter, there is the need to define our vector norm that will be used in the remainder of this chapter.

Definition 2. *Let* $\Big(\mathbf{X}, \|\cdot\|_{\mathbf{X}}\Big)$ *be a Banach space and let* $z = \begin{pmatrix} u \\ v \\ w \end{pmatrix}$ *such that* $z \in \mathbf{Y} = \mathbf{X}^3$. *We will define*

$$\|z\|_{\mathbf{Y}} := \|u\|_{\mathbf{X}} + \|v\|_{\mathbf{X}} + \|w\|_{\mathbf{X}}.$$

In the next section, we will outline some of the classical results that will be used in the remainder of this chapter.

3.3 Some useful classical results

In this section, we will state some of the classical results[3] that will be used to prove the existence of solutions for the system of reaction-diffusion equations used to model the radiation-induced bystander effects (3.9). Although, these results hold in their respective underlying Banach spaces. They also hold up to a finite Cartesian product of these underlying spaces.

Let $C^{0,\alpha}(\bar{\Omega}),\ 0 < \alpha \leq 1$, be the spaces of Hölder continuous functions on a bounded domain $\bar{\Omega}$ with the norm given by

$$\|f\|_{0,\alpha} = \sup |f| + |f|_{0,\alpha},$$

where

$$|f|_{0,\alpha} = \sup_{x,y\in\bar{\Omega}, x\neq y} \frac{|f(x) - f(y)|}{|x-y|^{\alpha}}.$$

We will use the following classical result to deduce that the non-linearity $G(z) \in L^p(\Omega)^3$ for $p \in (1, \infty)$.

Lemma 3. *Let* $\bar{\Omega}$ *be bounded.* $C^{0,\alpha}(\bar{\Omega}) \subset L^p(\Omega)$, *for* $p \in (1, \infty)$.

---

[3] please consult the references for the details of the proofs

Proof. Let $f \in C^{0,\alpha}(\bar{\Omega})$, then

$$\begin{aligned} \|f\|_p \ := \ \left(\int_\Omega |f|^p\right)^{\frac{1}{p}} &\leq |\Omega|^{\frac{1}{p}} \sup |f| \\ &\leq |\Omega|^{\frac{1}{p}} \sup |f| + |\Omega|^{\frac{1}{p}} |f|_{0,\alpha} \\ &= |\Omega|^{\frac{1}{p}} \|f\|_{0,\alpha}. \end{aligned}$$

Since $\|f\|_{0,\alpha} < \infty$ then the result follows. □

Lemma 4. *If $G(z(x,t))$ is Hölder continuous in $z(x,t)$ and $z(x,t)$ is Lipschitz continuous in x. Then $G(z(x,t))$ is Hölder continuous in x for every finite $t > 0$.*

Proof. Since $G(z(x,t))$ is Hölder continuous in $z(x,t)$ we have

$$|G(z(x,t)) - G(z(y,t))| \leq C_1 |z(x,t) - z(y,t)|^\alpha. \tag{3.23}$$

If $z(x,t)$ is Lipschitz continuous in x for every $t > 0$ then we have

$$|z(x,t) - z(y,t)| \leq C_2 |x - y|. \tag{3.24}$$

Substituting (3.24) into (3.23) yields

$$|G(z(x,t)) - G(z(y,t))| \leq C|x - y|^\alpha,$$

and the result follows. □

If the function $G(z(x,t))$ is $C^\infty(\Omega)$ in $z(x,t)$ it is then Hölder continuous in $z(x,t)$. In addition, if $z(x,t)$ is Lipschitz continuous in x, then Lemma 4 implies that $G(z(x,t))$ is Hölder continuous in x. By applying Lemma 3, we have the following corollary:

Corollary 4. *Suppose $\bar{\Omega}$ is bounded. If $G(z(x,t)) \in C^\infty(\Omega)$ then $G(z(x,t)) \in L^p(0,T; L^p(\Omega))$ for every finite $T > 0$. Indeed, for every finite $T > 0$,*

$$\int_0^T \|G(z(x,t))\|_p^p dt = \int_0^T \int_\Omega |G(z(x,t))|^p dx dt \ \leq \ T|\Omega| \|G\|_{0,\alpha}^p < \infty.$$

We will use the following result, which is usually a corollary to Alaoglu compactness theorem, in the proof of the existence of solution of (3.9). This result is from Corollary 4.19 in [99].

Lemma 5 (Reflexive weak compactness)**.** *Let X be a reflexive Banach space and x_n a bounded sequence in X. Then x_n has a subsequence that converges weakly in X.*

The above result will be very useful in extracting a convergent subsequence from a bounded sequence in a Hilbert space. In the next lemma, which is from Theorem 8.1, [99], we will interpret $A \subset\subset B$ as "A is compactly embedded B".

Lemma 6. *Let $X \subset\subset H \subset Y$ be Banach spaces, with X reflexive. Suppose that u_n is a sequence that is uniformly bounded in $L^2(0,T;X)$, and du_n/dt is uniformly bounded in $L^p(0,T;Y)$, for some $p > 1$. Then there is a subsequence that converges strongly in $L^2(0,T;H)$.*

The following result is from Exercise 7.3 in [99].

Lemma 7. *Let $1 \leq p < \infty$. Then elements of the form*

$$\psi = \sum_{j=1}^{n} \psi_j \alpha_j(t), \tag{3.25}$$

with $\psi_j \in V$ and $\alpha_j \in L^p(0,T)$, are dense in $L^p(0,T;V)$. Moreover, the result also holds for $\alpha_j \in C^1(0,T)$ or $\psi_j \in C_c^\infty(\Omega)$.

The following result is adapted from Lemma 8.3 in [99]

Lemma 8. *Let $U \subset \mathbf{R}^m$ be bounded and open, and let g_j be a bounded sequence of functions in $L^p(U)$. If $g \in L^p(U)$ and $g_j \to g$ a.e then $g_j \rightharpoonup g$ in $L^p(U)$.*

The following result is adapted from Theorem 7.2 in [99].

Lemma 9. *Suppose that*

$$u \in L^2(0,T;H^1(\Omega))^3 \qquad \text{and} \qquad \frac{du}{dt} \in L^2(0,T;H^{-1}(\Omega))^3$$

then $u \in C^0(0,T;L^2(\Omega))$, with

$$\sup_{t\in[0,T]} |u(t)| \leq C\Big(\|u\|_{L^2(0,T;H^1(\Omega))} + \Big\|\frac{du}{dt}\Big\|_{L^2(0,T;H^{-1}(\Omega))}\Big).$$

In the next section, we will employ the above classical results to establish the existence of weak solutions for the system of PDEs with $G(z)$ as the reaction term.

3.4 Existence of solutions to the system of PDEs with reaction term $G(z)$

In this section, we will focus on the system (3.9) with reaction term $G(z)$. A natural way to think of a solution $z(x,t)$ is as a trajectory in some infinity-dimensional phase space. That is, we can view $z(x,t)$ as a sequence of functions $z(t)$, each defined on Ω, so that

$$[z(t)](x) = z(x,t) \quad \text{with} \quad z(t) : \Omega \to \mathbf{D}^3, \quad \text{for some space } \mathbf{D}. \tag{3.26}$$

In the light of (3.26), we will rewrite (3.9) as

$$\frac{dz}{dt} + Az = G(z), \tag{3.27}$$

where $A = -\Delta$ with Neumann boundary condition.

Definition 3 (Weak Solution)**.** *We say that a function*

$$z \in L^2(0,T;H^1(\Omega))^3 \quad \textit{with} \quad \frac{dz}{dt} \in L^2(0,T;H^{-1}(\Omega))^3$$

is a weak solution of the initial-boundary-value problem in (3.9) provided

$$\left\langle \frac{dz}{dt}, \nu \right\rangle + \langle Az, \nu \rangle = \langle G(z), \nu \rangle$$

for each $\nu \in L^2(0,T;H^1(\Omega))^3$ *and a.e. time* $0 \le t \le T$*; and* $z(0) = z_0$*.*

Theorem 5 (Existence of weak solution)**.** *Given* $z_0 \in L^2(\Omega)^3$*, then the system of equations (3.9), with* $G(z)$ *satisfying properties (3.15), (3.17), and (3.18), has a unique weak solution* $z(t)$ *for any* $T > 0$*. Moreover,*

$$z \in L^2(0,T;H^1(\Omega))^3 \cap C^0(0,T;L^2(\Omega))^3,$$

and $z_0 \mapsto z(t)$ *is continuous on* $L^2(\Omega)^3$. *Eq. (3.27) holds as an equality in* $L^2(0,T;H^{-1}(\Omega))^3$.

Proof. Using Galerkin approximation, we look for an approximate solution $z_n(t)$ that lies in the finite dimensional space spanned by the first n eigenfunctions, $\omega_j \in L^2(\Omega)^3$, of A i.e.,

$$z_n(x,t) \;=\; \sum_{j=1}^{n} z_{nj}(t)\omega_j(x), \tag{3.28}$$

and solves

$$\left\langle \frac{dz_n}{dt}, \omega_j \right\rangle + \langle Az_n, \omega_j\rangle = \langle G(z_n), \omega_j\rangle, \quad 1 \le j \le n, \tag{3.29}$$

with $\langle z_n(0), \omega_j\rangle = \langle z_0, \omega_j\rangle$.
Since each ω_j is orthonormal, from (3.28) we have $z_{nj} = \langle z_n, w_j\rangle$; also

$$\left\langle \frac{dz_n}{dt}, w_j \right\rangle = \frac{dz_{nj}}{dt} \quad \text{and} \quad \langle Az_n, w_j\rangle = \lambda_j z_{nj}.$$

So we have the following set of ODEs for the components z_{nj}:

$$\frac{dz_{nj}}{dt} + \lambda_j z_{nj} = \langle G(z_{nj}), w_j\rangle.$$

We could also write this as

$$\frac{dz_n}{dt} + Az_n = P_n G(z_n), \qquad z_n(0) = P_n z_0, \tag{3.30}$$

where P_n is the orthogonal projection in $L^2(\Omega)^3$ unto the span of $\{\omega_1, \cdots, \omega_n\}$. Since the nonlinearity in (3.30) is locally Lipschitz by Lemmas 1 and 2 , then the finite dimensional system (3.30) has a unique local solution.

It remains to show that the solutions are bounded in time and uniformly bounded in n. If we multiply (3.30) by z_n and integrate over domain Ω, while noting that

$$\langle P_n G(z_n), z_n\rangle = \langle G(z_n), P_n z_n\rangle = \langle G(z_n), z_n\rangle,$$

we get

$$\frac{1}{2}\frac{d}{dt}\|z_n\|_2^2 + \|\nabla z_n\|_2^2 = \int_\Omega G(z_n) z_n dx.$$

Now we can use Theorem 3 to write

$$\begin{aligned} \frac{1}{2}\frac{d}{dt}\|z_n\|_2^2 + \|\nabla z_n\|_2^2 &\leq \int_\Omega M - k_2|z_n|^2 dx \\ &= M|\Omega| - k_2\|z_n\|_2^2. \end{aligned} \tag{3.31}$$

This implies that

$$\frac{1}{2}\frac{d}{dt}\|z_n\|_2^2 + k\|z_n\|_{\mathbf{H^1}}^2 \leq M|\Omega|, \qquad \text{for some } k.$$

Integrating both sides between 0 and T gives

$$\frac{1}{2}\|z_n(T)\|_2^2 + k\int_0^T \|z_n\|_{\mathbf{H^1}}^2 dt \leq M|\Omega|T + \frac{1}{2}\|z_0\|_2^2.$$

It then follows from the last inequality that

$$\sup_{t\in[0,T]} \|z_n(t)\|_2^2 \leq 2K,$$

$$\int_0^T \|z_n\|_{\mathbf{H^1}}^2 dt \leq \frac{K}{k},$$

where $K := M|\Omega|T + \frac{1}{2}\|z_0\|_2^2 < \infty$, for bounded sets of initial conditions in $L^2(\Omega)^3$ and bounded time intervals. This implies that

$$z_n \quad \text{is uniformly bounded in} \quad L^\infty(0,T;L^2(\Omega))^3, \tag{3.32}$$

$$z_n \quad \text{is uniformly bounded in} \quad L^2(0,T;H^1(\Omega))^3. \tag{3.33}$$

Corollary 4 already shows that

$$G(z_n) \quad \text{is uniformly bounded in} \quad L^p(0,T;L^p(\Omega))^3. \tag{3.34}$$

Finally, we need a uniform bound on $\frac{dz_n}{dt}$. We first note that $L^2(0,T;H^{-1}(\Omega))^3$

and $L^p(0,T;L^p(\Omega))^3$ are continuously included in $L^p(0,T;H^{-1}(\Omega))^3$, for $p=2$. It follows that since

$$\frac{dz_n}{dt} = -Az_n + P_nG(u_n),$$

we have

$$\frac{dz_n}{dt} \quad \text{is uniformly bounded in} \qquad L^2(0,T;H^{-1}(\Omega))^3.$$

Based on (3.32) and (3.33) and using Lemma 5 we can extract a weakly convergent subsequence, z_n, with

$$\begin{aligned} z_n \rightharpoonup z \quad &\text{in} \quad L^2(0,T;H^1(\Omega))^3, &(3.35)\\ G(z_n) \rightharpoonup \chi \quad &\text{in} \quad L^2(0,T;L^2(\Omega))^3. &(3.36)\end{aligned}$$

Since $H^1(\Omega)^3 \subset\subset L^2(\Omega)^3 \subset H^{-1}(\Omega)^3$ and $H^1(\Omega)^3$ is reflexive we can apply Lemma 6 to further extract a subsequence such that

$$z_n \to z \qquad \text{in} \quad L^2(0,T;L^2(\Omega))^3.$$

Note that this space can also be written as $L^2(\Omega_T)^3$, where $\Omega_T = \Omega \times T$. If $Q_n = I - P_n$, since we want $P_nG(z_n) \rightharpoonup \chi$ in $L^2(0,T,L^2(\Omega))^3$, we can write

$$\begin{aligned}\int_{\Omega\times T}(P_nG(z_n)-\chi)\psi dxdt \;&=\; \int_{\Omega\times T}(G(z_n)-\chi)\psi dxdt\\ &\quad -\int_{\Omega\times T} Q_nG(z_n)\psi dxdt \qquad (3.37)\end{aligned}$$

for all $\psi \in L^2(0,T;L^2(\Omega))^3$. The first term in (3.37) tends to zero by (3.36). For the convergence of the second term, we will employ Lemma 7 to find functions of the form (3.25) with $\alpha_j \in L^2(0,T)^3$ and $\psi_j \in C_c^\infty(\Omega)^3$ which are dense in $L^2(0,T;L^2(\Omega))^3$. For such functions

$$\int_{\Omega_T}\sum_{i=1}^{3}[Q_nG(z_n)]_i \sum_{j=1}^{n}\psi_j^i\alpha_j^i(t)dxdt = \int_{\Omega_T}\sum_{i=1}^{3}[G(z_n)]_i\Big(\sum_{j=1}^{n}\alpha_j^i(t)Q_n\psi_j^i\Big)dxdt.$$

Since $Q_n \psi_j^i \to 0$ in $L^2(\Omega)$ for each i and j, we have the required convergence of $P_n G(z_n)$. Notice that $L^2(0,T;H^1(\Omega))^3 \cap L^2(0,T;L^2(\Omega))^3 = L^2(0,T;H^1(\Omega))^3$.

It then follows that all terms converge in the dual space $L^2(0,T;H^{-1}(\Omega))^3$ of $L^2(0,T;H^1(\Omega))^3$. The following equality also holds in this dual space:

$$\frac{dz}{dt} + Az = \chi.$$

It remains to show that $\chi = G(z)$. Since $z_n \to z$ in $L^2(\Omega_T)^3$, then there is a subsequence $z_{n_j}(x,t)$ that converges pointwise to $z(x,t)$ almost everywhere in Ω_T. By the continuity of G, then $G(z_{n_j}(x,t)) \to G(z(x,t))$ for a.e $(x,t) \in \Omega_T$. By the bound of $G(z_{n_j})$ in $L^2(\Omega_T)^3$ in (3.34), we can apply Lemma 8 to deduce that $G(z_{n_j}) \rightharpoonup G(z)$ in $L^2(\Omega_T)^3$. By uniqueness of weak limits, it follows that $\chi = G(z)$.

To prove that $z \in C^0(0,T;L^2(\Omega))^3$, we use the fact that $z \in L^2(0,T;H^1(\Omega))^3$ and $\frac{dz}{dt} = -Az + G(z) \in L^2(0,T;H^{-1}(\Omega))^3$, and then apply Lemma 9 to deduce that $z \in C^0(0,T;L^2(\Omega))^3$.

To show that $z(0) = z_0$, we will choose some $\phi \in C^1(0,T;H^1(\Omega) \cap L^2(\Omega))^3$ with $\phi(T) = 0$. Observe that $\phi \in L^2(0,T;H^1(\Omega))^3$. So if we integrate

$$\left\langle \frac{dz}{dt}, \phi \right\rangle + \langle Az, \phi \rangle = \langle G(z), \phi \rangle$$

by parts in the t variable we get

$$\int_0^T -\langle z, \dot{\phi} \rangle + \langle Az, \phi \rangle ds = \int_0^T \langle G(z), \phi \rangle ds + \langle z(0), \phi(0) \rangle.$$

Also, doing the same in the Galerkin approximations yields

$$\int_0^T -\langle z_n, \dot{\phi} \rangle + \langle Az_n, \phi \rangle ds = \int_0^T \langle P_n G(z_n), \phi \rangle ds + \langle z_n(0), \phi(0) \rangle. \tag{3.38}$$

We can take limits in (3.38) to conclude that

$$\int_0^T -\langle z, \dot{\phi} \rangle + \langle Az, \phi \rangle ds = \int_0^T \langle G(z), \phi \rangle ds + \langle z_0, \phi(0) \rangle,$$

since $z_n(0) = P_n z_0 \to z_0$. Thus, $z(0) = z_0$.

To prove uniqueness and continuous dependence, let $z_0,\ \zeta_0 \in L^2(\Omega)^3$ and consider $\xi(t) = z(t) - \zeta(t)$. Then

$$\frac{\partial \xi}{\partial t} + A\xi = G(z) - G(\zeta), \qquad \xi(0) = z_0 - \zeta_0.$$

Multiplying by ξ and integrating over Ω gives

$$\frac{1}{2}\frac{d}{dt}\|\xi\|_2^2 + \|\nabla \xi\|_2^2 = \langle G(z) - G(\zeta), z - \zeta \rangle.$$

The RHS can be further simplified as follows:

$$\begin{aligned}
\langle G(z) - G(\zeta), z - \zeta \rangle &= \int_\Omega \big(G(z) - G(\zeta)\big)(z - \zeta)dx \\
&= \int_\Omega \sum_{i=1}^{3} \Big(G_i(z_1, z_2, z_3) - G_i(\zeta_1, \zeta_2, \zeta_3)\Big)(z_i - \zeta_i)dx \\
&= \int_\Omega \sum_{i=1}^{3} \Big(G_i(z_1, z_2, z_3) - G_i(\zeta_1, z_2, z_3) \\
&\quad + G_i(\zeta_1, z_2, z_3) - G_i(\zeta_1, \zeta_2, z_3) \\
&\quad + G_i(\zeta_1, \zeta_2, z_3) - G_i(\zeta_1, \zeta_2, \zeta_3)\Big)(z_i - \zeta_i)dx \\
&= \int_\Omega \sum_{i=1}^{3} \Big[\sum_{j=1}^{3} \int_{\zeta_j}^{z_j} \frac{\partial G_i}{\partial z_j}(s)ds\Big](z_i - \zeta_i)dx \\
&= \int_\Omega \sum_{i,j=1}^{3} l_{i,j}(z_j - \zeta_j)(z_i - \zeta_i)dx \qquad (3.39) \\
&\leq 3l \int_\Omega \sum_{i=1}^{3} |z_i - \zeta_i|^2 dx \qquad (3.40) \\
&= 3l \int_\Omega |z - \zeta|^2 dx \\
&= 3l\|z - \zeta\|_2^2 \\
&= 3l\|\xi\|_2^2.
\end{aligned}$$

The equality in (3.39) holds from Corollary 2, which implicitly implies that if

z is bounded then $\frac{\partial G_i}{\partial z_j}(z)$ is finite for each i, j. Also, we have assumed that

$$\frac{\partial G_i}{\partial z_j} = l_{i,j}.$$

In (3.40), we assume that $l = \sup_{i,j} l_{i,j}$ and then expand the bracket in the integrand using Young's Inequality. We therefore obtain

$$\frac{1}{2}\frac{d}{dt}\|\xi\|_2^2 \leq 3l\|\xi\|_2^2,$$

and integrating this yields

$$\|z(t) - \zeta(t)\|_2 \leq \|z_0 - \zeta_0\|_2 e^{3lt}.$$

This is uniqueness if $z_0 = \zeta_0$ and is continuous dependence on initial data otherwise.

So far we have established the existence of global weak solution to the system of PDE modeling evolution bystander signals after radiation exposure. In the next section, we will show the existence theory for the full system of PDE model with the radiation terms. □

3.5 Existence of solutions to the system of PDEs with reaction term $G_R(z)$

In this section, we will focus on establishing the existence of unique, bounded, weak solution for the full system in (3.4). The main challenge here is the presence of inherent discontinuity in time in the reaction term $G_R(z)$ due to switching on/off radiation. In order to establish the existence and uniqueness of bounded solutions (in appropriate Sobolev spaces), we will consider the following system:

$$\frac{dz_h}{dt} + Az_h = G_h(z_h), \tag{3.41}$$

where $\{G_h\}_h$ is a sequence of smooth functions such that $G_h \to G_R$ "in some sense" (which will soon be made rigorous) as $h \to 0$. To show the global existence of unique, weak solution for the system of PDEs with G_R as its reaction terms, we proceed as follows:

- Since G_h is Lipschitz for each h, then (similar to the case with $G(z)$ in Theorem 5) there exists a unique, bounded, weak solution z_h for each h;
- Also, similar to the case with $G(z)$, we can write (3.41) as an equality in $L^2(0,T;H^{-1}(\Omega))^3$ for each h. Thus, if $G_h \to G_R$ uniformly in $L^2(0,T;H^{-1}(\Omega))^3$ as $h \to 0$ then $z_h \to z$ as $h \to 0$, where z is the unique, bounded, weak solution of

$$\frac{dz}{dt} + Az \;=\; G_R(z). \tag{3.42}$$

We therefore need to first establish that $G_R(z) \in L^2(0,T;H^{-1}(\Omega))^3$. Recall that $G_R(z) = G(z) + R(t,z)$, where

$$R(t,z) = \begin{pmatrix} -r_u(t)u - \gamma(t)u \\ -r_v(t)v + \gamma(t)u \\ \lambda_1 r_v(t)v + \lambda_2 r_u(t)u \end{pmatrix}.$$

Since $G(z) \in L^2(0,T;H^{-1}(\Omega))^3$ by Theorem 5, investigating that $G_R(z) \in L^2(0,T;H^{-1}(\Omega))^3$ is equivalent to checking if $R(t,z) \in L^2(0,T;H^{-1}(\Omega))^3$. We have the following result to this effect:

Lemma 10. *If $z \in L^2(0,T;H^1(\Omega))^3$ then $R(t,z) \in L^2(0,T;H^{-1}(\Omega))^3$.*

Proof. It suffices to show that

$$\|R(t,z)\|_{H^{-1}(\Omega)^3} \le K_0 \|z\|_{H^1(\Omega)^3},$$

for some $K_0 > 0$.

To this end,

$$\|R(t,z)\|_{H^{-1}(\Omega)^3} \;=\; \sup_{\|\theta\|_{H^{-1}(\Omega)^3} \le 1} \langle R(t,z), \theta \rangle,$$

where

$$\begin{aligned}
\langle R(t,z),\theta\rangle &= \int_\Omega R(t,z)\theta dx \\
&= \int_\Omega r_u(t)(\lambda_2 u\theta_3 - u\theta_1) + \boldsymbol{\gamma}(t)(u\theta_2 - u\theta_1) \\
&\quad + r_v(t)(\lambda_1 v\theta_3 - v\theta_2)dx \\
&= \int_\Omega u(\boldsymbol{\gamma}(t)\theta_2 + r_u(t)\lambda_2\theta_3 - r_u(t)\theta_1 - \boldsymbol{\gamma}(t)\theta_1) \\
&\quad + v(r_v(t)\lambda_1\theta_3 - r_v(t)\theta_2)dx \\
&= \int_\Omega z \cdot m \ dx, \qquad (3.43)
\end{aligned}$$

where

$$m = \begin{pmatrix} \boldsymbol{\gamma}(t)\theta_2 + r_u(t)\lambda_2\theta_3 - r_u(t)\theta_1 - \boldsymbol{\gamma}(t)\theta_1 \\ r_v(t)\lambda_1\theta_3 - r_v(t)\theta_2 \\ 0 \end{pmatrix};$$

with

$$\begin{aligned}
m_1 &= \begin{pmatrix} (-\boldsymbol{\gamma}(t) - r_u(t)) & \boldsymbol{\gamma}(t) & r_u(t)\lambda_2 \end{pmatrix} \cdot \theta \\
m_2 &= \begin{pmatrix} 0 & -r_v(t) & r_v(t)\lambda_1 \end{pmatrix} \cdot \theta \\
m_3 &= \begin{pmatrix} 0 & 0 & 0 \end{pmatrix} \cdot \theta,
\end{aligned}$$

where

$$\theta = \begin{pmatrix} \theta_1 & \theta_2 & \theta_3 \end{pmatrix}^T.$$

Applying Cauchy-Schwartz's Inequality to Eqn. (3.43), we have

$$\langle R(t,z),\theta\rangle \leq \|z\|_{H^1(\Omega)^3}\|m\|_{H^{-1}(\Omega)^3}.$$

To compute $\|m\|_{H^{-1}(\Omega)^3}$, we proceed as follows:

$$\|m\|_{H^{-1}(\Omega)^3} = \sup_{\|\zeta\|_{H^1(\Omega)^3} \leq 1} \langle m, \zeta\rangle$$

with

$$\begin{aligned}
\langle m, \zeta\rangle &= \int_\Omega m\cdot\zeta dx \\
&= \int_\Omega \gamma(t)\theta_2\zeta_1 + r_u(t)\lambda_2\theta_3\zeta_1 - r_u(t)\theta_1\zeta_1 - \gamma(t)\theta_1\zeta_1 \\
&\quad +r_v(t)\lambda_1\theta_3\zeta_2 - r_v(t)\theta_2\zeta_2 dx \\
&\le \int_\Omega \gamma(t)\theta_2\zeta_1 + r_u(t)\lambda_2\theta_3\zeta_1 + r_v(t)\lambda_1\theta_3\zeta_2 dx \\
&\le \int_\Omega \bar{\gamma}\theta_2\zeta_1 + \bar{r}_u\lambda_2\theta_3\zeta_1 + \bar{r}_v\lambda_1\theta_3\zeta_2 dx \\
&\le k\int_\Omega \theta_2\zeta_1 + \theta_3\zeta_1 + \theta_3\zeta_2 dx \\
&= k\int_\Omega \begin{pmatrix}\theta_2+\theta_3\\ \theta_3\\ 0\end{pmatrix}\cdot\begin{pmatrix}\zeta_1\\ \zeta_2\\ \zeta_3\end{pmatrix} dx \\
&\le K_0\langle\theta,\zeta\rangle, \quad \text{for some } K_0 \\
&\le K_0\|\theta\|_{H^{-1}(\Omega)^3}\|\zeta\|_{H^1(\Omega)^3},
\end{aligned}$$

where $k = \max\{\bar{\gamma}, \bar{r}_u\lambda_2, \bar{r}_v\lambda_1\}$ and the last inequality is from Cauchy-Schwartz's inequality. Consequently,

$$\|m\|_{H^{-1}(\Omega)^3} = \sup_{\|\zeta\|_{H^1(\Omega)^3}\le 1}\langle m,\zeta\rangle \le K_0\|\theta\|_{H^{-1}(\Omega)^3}.$$

We then have

$$\begin{aligned}
\sup_{\|\theta\|_{H^{-1}(\Omega)^3}\le 1}\langle R(t,z),\theta\rangle &\le \sup_{\|\theta\|_{H^{-1}(\Omega)^3}\le 1}\|z\|_{H^1(\Omega)^3}\|m\|_{H^{-1}(\Omega)^3} \\
&\le \sup_{\|\theta\|_{H^{-1}(\Omega)^3}\le 1} K_0\|z\|_{H^1(\Omega)^3}\|\theta\|_{H^{-1}(\Omega)^3} \\
&\le K_0\|z\|_{H^1(\Omega)^3}
\end{aligned}$$

This implies that

$$\|R(t,z)\|_{H^{-1}(\Omega)^3} \le K_0\|z\|_{H^1(\Omega)^3}.$$

$\square$

We will now formally construct the sequence $\{G_h\}$ of smooth functions. First, let us define a time-dependent mollifier function $\rho(t)$ as

$$\rho(t) = \begin{cases} c\exp(\frac{1}{t^2-1}), & |t| \leq 1 \\ 0, & |t| \geq 1, \end{cases}$$

with a choice of c so that $\int_{\mathbf{R}} \rho(t)dt = 1$. Then for each h,

$$R_h(t,z) := \rho_h(t) * R(t,z) \in C^\infty(0,T;H^{-1}(\Omega))^3,$$

where $\rho_h(t) = h^{-1}\rho\big(\frac{t}{h}\big)$ and $*$ signifies convolution. For each h, we define our sequence $\{G_h\}$ of smooth functions as

$$G_h(z) = G(z) + R_h(t,z). \tag{3.44}$$

Since Lemma 10 implies that $R(t,z) \in L^2(0,T;H^{-1}(\Omega))^3$ whenever we have $z \in L^2(0,T;H^1(\Omega))^3$, then to complete the existence proof for system (3.42) we only need to show that

$$R_h(t,z) \to R(t,z) \quad \text{in} \;\; L^2(0,T;H^{-1}(\Omega))^3 \;\; \text{uniformly as} \;\; h \to 0.$$

Theorem 6. *If* $R(t,z) \in L^2(0,T;H^{-1}(\Omega))^3$ *then* $R_h(t,z) \to R(t,z)$ *uniformly in* $L^2(0,T;H^{-1}(\Omega))^3$ *as* $h \to 0$.

Proof. Let $L^* = L^2(0,T;H^{-1}(\Omega))^3$, $H^* = H^{-1}(\Omega)^3$, $H = H^1(\Omega)^3$. We claim that

$$\|R_h(t,z)\|_{L^*} \;\; \leq \;\; \|R(\tau,z)\|_{L^*}, \quad \forall h, \;\; \forall R \in L^*. \tag{3.45}$$

Suppose for the moment that the claim is true. Let's choose a function $K \in C(0,T;H^{-1}(\Omega))$ such that

$$\|R-K\|_{L^*} < \delta.$$

Also, let $K_h = \rho_h(t) * K(t,z)$, which obviously belong to $C(0,T;H^{-1}(\Omega))$. Therefore, using (3.45) we find

$$\begin{aligned}
\|R_h - R\|_{L^*} &= \|R_h - K_h + K_h - K + K - R\|_{L^*} \\
&\le \|R_h - K_h\|_{L^*} + \|K_h - K\|_{L^*} + \|K - R\|_{L^*} \\
&\le 2\|R - K\|_{L^*} + \|K_h - K\|_{L^*} \\
&= 2\delta + \|K_h - K\|_{L^*}.
\end{aligned}$$

Since $K_h \to K$ uniformly as $h \to 0$, we have $\limsup_{h\to 0} \|R_h - R\|_{L^*} \le 2\delta$.

To prove the above claim (3.45), we consider

$$\|R_h(t,z)\|^2_{L^*} = \int_0^T \|R_h(s,z)\|^2_{H^*} ds,$$

with

$$\begin{aligned}
\|R_h(s,z)\|_{H^*} &= \sup_{\|\theta\|_H \le 1} \int_\Omega R_h(s,z)\cdot\theta dx \\
&= \sup_{\|\theta\|_H \le 1} \int_\Omega \theta \int_0^T \rho_h(s-\tau) R(\tau,z) d\tau dx \\
&= \sup_{\|\theta\|_H \le 1} \int_0^T \rho_h^{\frac{1}{2}}(s-\tau) \int_\Omega \rho_h^{\frac{1}{2}}(s-\tau)\theta R(\tau,z) dx d\tau \\
&\le \Big(\sup_{\|\theta\|_H \le 1} \int_0^T \rho_h(s-\tau)d\tau\Big)^{\frac{1}{2}} \\
&\quad \Big[\int_0^T \Big(\int_\Omega \rho_h^{\frac{1}{2}}(s-\tau)\theta R(\tau,z)dx\Big)^2 d\tau\Big]^{\frac{1}{2}} \qquad (3.46) \\
&\le \sup_{\|\theta\|_H \le 1} \Big[\int_0^T \Big(\int_\Omega \rho_h^{\frac{1}{2}}(s-\tau)\theta R(\tau,z)dx\Big)^2 d\tau\Big]^{\frac{1}{2}} \\
&= \sup_{\|\theta\|_H \le 1} \Big[\int_0^T \Big(\rho_h^{\frac{1}{2}}(s-\tau)\int_\Omega \theta R(\tau,z)dx\Big)^2 d\tau\Big]^{\frac{1}{2}} \\
&= \sup_{\|\theta\|_H \le 1} \Big[\int_0^T \rho_h(s-\tau)\Big(\int_\Omega \theta R(\tau,z)dx\Big)^2 d\tau\Big]^{\frac{1}{2}},
\end{aligned}$$

where we have used Holder's Inequality in (3.46).

$$\begin{aligned}
\|R_h(t,z)\|^2_{L^*} &:= \int_0^T \|R_h(s,z)\|^2_{H^*} ds \\
&\leq \int_0^T \sup_{\|\theta\|_H \leq 1} \int_0^T \rho_h(s-\tau)\Big(\int_\Omega \theta R(\tau,z)dx\Big)^2 d\tau ds \\
&\leq \int_0^T \sup_{\|\theta\|_H \leq 1} \int_0^T \rho_h(s-\tau)\Big(\|R(\tau,z)\|_{H^*}\|\theta\|_H\Big)^2 d\tau ds \\
&\leq \int_0^T \int_0^T \rho_h(s-\tau)\|R(\tau,z)\|^2_{H^*} d\tau ds \\
&= \int_0^T \int_0^T \rho_h(s-\tau)ds \ \ \|R(\tau,z)\|^2_{H^*} d\tau \\
&= \int_0^T \|R(\tau,z)\|^2_{H^*} d\tau = \|R(\tau,z)\|^2_{L^*}.
\end{aligned}$$

□

This result shows that $G_h \to G_R$ uniformly in $L^2(0,T;H^{-1}(\Omega))^3$ as $h \to 0$. This in turn implies that $z_h \to z \in L^p(0,T;H^1(\Omega))^3$, where z is the unique solution of the full system of PDE with radiation. Thus, we have proved the following existence theorem for the fully system of PDE in (3.4) with radiation terms (3.42):

Theorem 7 (Existence theory for the full system). *Given $z_0 \in L^2(\Omega)^3$, then the system of equations (3.4) has a unique, bounded weak solution $z(t)$ for any $T > 0$. Moreover,*

$$z \in L^2(0,T;H^1(\Omega))^3$$

and equation (3.42) holds as an equality in $L^2(0,T;H^{-1}(\Omega))^3$.

3.6 Existence of global attractor for the PDEs with $G(z)$

In this section, we will prove the existence of a global attractor for the system of PDE with reaction term $G(z)$ in $L^2(\Omega)^2$. In the following, we will precisely define the notion of ω-limit set, which will be critical in the analysis of this section.

Definition 4 (ω-limit set)**.** *The ω-limit set of a set $\mathcal{D}$ is the set consisting of all the limit points of the orbits, $S(t)$, of $\mathcal{D}$. Precisely, $\omega(\mathcal{D}) := \{y : \exists \ \ t_n \to \infty, x_n \in \mathcal{D} \ \ with \ \ S(t_n)x_n \to y\}$.*

Since global attractor is the ω-limit set of a compact absorbing set, we will first prove the existence of a compact absorbing set. We will start by finding an absorbing set in $L^2(\Omega)^3$, and then use the result to show the existence of an absorbing set in $H^1(\Omega)^3$. Since $H^1(\Omega)^3$ is compactly embedded in $L^2(\Omega)^3$, the we have a compact absorbing set in $L^2(\Omega)^3$.

In the rest of this section, we will denote $\mathbf{H}^1 := H^1(\Omega)^3$ and $\mathbf{L}^2 := L^2(\Omega)^3$. We proceed as follows:

Proposition 1 (Absorbing set in $\mathbf{L}^2$)**.** *The reaction-diffusion system (3.9) has an absorbing set in $\mathbf{L}^2$; there is a constant I_0 and a time $t_0(\|z_0\|_2)$ such that the solution $z(t)$ satisfies*

$$\|z(t)\|_2 \leq I_0, \quad \forall \ t \geq t_0(\|z_0\|_2)$$

In addition there is a constant I_1 such that

$$\int_t^{t+1} \|z\|^2_{\mathbf{H}^1} dx \leq I_1, \quad \forall \ t > t_0(\|z_0\|_2) \tag{3.47}$$

Proof. If we multiply (3.27) by z and integrate over Ω while applying Theorem 3, we obtain

$$\frac{d}{dt}\|z(t)\|_2^2 + \|\nabla z\|_2^2 \leq 2M|\Omega| - 2k_2\|z\|_2^2, \tag{3.48}$$

from which we can derive

$$\frac{d}{dt}\|z(t)\|_2^2 + 2k_2\|z\|_2^2 \leq 2M|\Omega|.$$

Using Gronwall inequality we derive

$$\|z(t)\|_2^2 \leq \|z_0\|_2^2 e^{-2k_2 t} + \frac{M|\Omega|}{k_2}(1 - e^{-2k_2 t}).$$

If $t \geq t_0(\|z_0\|_2) \;=\; \frac{1}{2k_2} \ln \frac{k_2\|z_0\|_2^2}{M|\Omega|}$, then

$$\|z(t)\|_2^2 \leq I_0^2 = \frac{2M|\Omega|}{k_2}. \tag{3.49}$$

Thus, there exists an absorbing set

$$B \;=\; \Big\{ z(t): \; \|z(t)\|_2^2 \leq I_0^2, \; \forall \; t \geq \frac{1}{2k_2} \ln \frac{k_2\|z_0\|_2^2}{M|\Omega|} \Big\} \subset \mathbf{L}^2.$$

Furthermore, from (3.48) we can also derive

$$\frac{d}{dt}\|z(t)\|_2^2 + \|\nabla z\|_2^2 + 2k_2\|z\|_2^2 \leq 2M|\Omega|,$$

which implies

$$\frac{d}{dt}\|z(t)\|_2^2 + k\|z\|_{\mathbf{H}^1}^2 \leq 2M|\Omega|, \quad \text{for some} \;\; k.$$

Integrating this last equation from t to $t+1$ we obtain

$$\begin{aligned} & \frac{1}{2}\|z\|_2^2 \Big|_t^{t+1} + k \int_t^{t+1} \|z\|_{\mathbf{H}^1}^2 dt \leq M|\Omega| \\ \Rightarrow \quad & \int_t^{t+1} \|z\|_{\mathbf{H}^1}^2 dt \leq \frac{M}{k}|\Omega| + \frac{1}{2k}\|z(t)\|_2^2 \;\leq\; \frac{M|\Omega|}{k}\Big(1 + \frac{1}{k_2}\Big) := I_1 \end{aligned}$$

for all $t \geq t_0(\|z_0\|_2)$. □

Suppose we multiply the non-linearity $G(z)$ by $-\Delta z$ and integrate over the space Ω, we derive

$$\begin{aligned} -\int_\Omega \Delta z \cdot G(z) dx &= \int_\Omega \nabla z^T \nabla G(z) \nabla z dz \\ &= \int_\Omega \sum_{i,j} \frac{\partial G_i}{\partial z_j} \frac{\partial z_i}{\partial x} \frac{\partial z_j}{\partial x} dx \\ &\leq \int_\Omega \sum_{i,j} l_{i,j} \frac{\partial z_i}{\partial x} \frac{\partial z_j}{\partial x} dx \qquad \text{from (3.18),} \end{aligned}$$

Thus, continuing from the last inequality, we have

$$\begin{aligned}
-\int_\Omega \Delta z \cdot G(z) &\leq I_2 \int_\Omega \sum_{i,j} \frac{\partial z_i}{\partial x}\frac{\partial z_j}{\partial x} dx \qquad \text{where } I_2 = \sup_{i,j} l_{i,j} \\
&\leq I_2 \int_\Omega 3|u_x|^2 + 3|v_x|^2 + 3|w_x|^2 dx \\
&= 3I_2 \int_\Omega |\nabla z|^2 dx.
\end{aligned}$$

The last inequality holds by Young's inequality.

If we multiply (3.27) by $-\Delta z$ and integrate over Ω, we obtain

$$\begin{aligned}
&\frac{1}{2}\frac{d}{dt}\|\nabla z\|_2^2 + \|Az\|_2^2 \leq 3I_2\|\nabla z\|_2^2 \\
\Rightarrow \quad &\frac{1}{2}\frac{d}{dt}\|\nabla z\|_2^2 \leq 3I_2\|\nabla z\|_2^2. \qquad (3.50)
\end{aligned}$$

Similarly from (3.31) we obtain

$$\frac{1}{2}\frac{d}{dt}\|z\|_2^2 \leq M|\Omega| + k_2\|z\|_2^2. \qquad (3.51)$$

Adding (3.50) and (3.51) we obtain

$$\frac{1}{2}\frac{d}{dt}\|z\|_{\mathbf{H}^1}^2 \leq M|\Omega| + k_0\|z\|_{\mathbf{H}^1}^2, \qquad \text{for some constant } k_0.$$

Integrating between s and t ($t-1 \leq s \leq t$) gives

$$\|z(t)\|_{\mathbf{H}^1}^2 \leq 2M|\Omega| + 2k_0 \int_s^t \|z(\zeta)\|_{\mathbf{H}^1}^2 d\zeta + \|z(s)\|_{\mathbf{H}^1}^2.$$

Integrating this equation with respect to s between $t-1$ and t we obtain

$$\|z(t)\|_{\mathbf{H}^1}^2 \leq 2M|\Omega| + (2k_0+1)\int_{t-1}^t \|z(s)\|_{\mathbf{H}^1}^2 ds.$$

Using (3.47) we obtain

$$\|z(t)\|_{\mathbf{H}^1}^2 \leq 2M|\Omega| + (2k_0+1)I_1, \qquad (3.52)$$

provided that $t \geq t_0(\|z_0\|_2) + 1$.

Since we do not know if the solution z is smooth enough to justify the above computations, we will need the following result to rigorously prove the existence of an absorbing set in $\mathbf{H}^1$.

Lemma 11 (Lemma 11.2 [99])**.** *Let $V \subset\subset H$, with dual V^*. Suppose that $\{z_n\}$ is uniformly bounded in $L^\infty(0,T;V)$,*

$$\mathit{ess}\sup_{t\in[0,T]} \|z_n(t)\| \leq C,$$

and that $z_n \rightharpoonup z$ in $L^2(0,T;V)$; then

$$\mathit{ess}\sup_{t\in[0,T]} \|z(t)\| \leq C.$$

Furthermore, if $z \in C^0(0,T;H)$ then in fact

$$\sup_{t\in[0,T]} \|z(t)\| \leq C.$$

In the next result we will apply the above result with $V = \mathbf{H}^1$ and $H = \mathbf{L}^2$.

Proposition 2. *Suppose that $\Omega \subset \mathbf{R}$. Then the reaction-diffusion system (3.9) has an absorbing set in $\mathbf{H}^1$; there is a constant I_4 and a time $t_1(\|z_0\|_2)$ such that*

$$\|z(t)\|_{\mathbf{H}^1} \leq I_4, \quad \forall\ t \geq t_1(\|z_0\|_2).$$

Proof. We will work with the truncated Galerkin equations

$$\frac{dz_n}{dt} + Az_n = P_nG(z_n), \qquad z_n(0) = P_n z_0.$$

If we follow the computation of Proposition 1 we get

$$\|z_n(t)\|_2 \leq I_0, \quad \forall\ t \geq t_0(\|z_0\|_2),$$

since $\|z_n(0)\|_2 \leq \|z_0\|_2$. Also, we can obtain the equivalent of (3.52) with z

replaced by z_n, i.e.

$$\|z_n(t)\|_{\mathbf{H}^1}^2 \leq 2M|\Omega| + (2k_0+1)I_1, \quad \forall\, t \geq t_0(\|z_0\|_2) + 1,$$

a bound uniform in n. If we take $I_5 = 2M|\Omega| + (2k_0+1)I_1$ and $t_1(\|z_0\|_2) = t_0(\|z_0\|_2) + 1$, then we can write, for any $T > t_1$,

$$\|z_n\|_{L^\infty(t_1,T,H^1(\Omega))^3} \leq I_5.$$

Since $z_n \rightharpoonup z$ in $L^2(0,T;H^1(\Omega))^3$ and $z \in C^0(0,T;L^2(\Omega))^3$, it follows using Lemma 11 that

$$\|z(t)\|_{\mathbf{H}^1}^2 \leq I_5, \quad \forall\, t \geq t_1(\|z_0\|_2).$$

□

Using the absorbing set in $\mathbf{H}^1$, we can deduce the existence of a global attractor as follows.

Theorem 8. *Suppose $\Omega \subset \mathbf{R}$, the reaction-diffusion system (3.9) has a connected and compact global attractor $\mathcal{A}$.*

Proof. Let

$$B := \{z \in \mathbf{H}^1 : \|z(t)\|_{\mathbf{H}^1}^2 \leq I_5, \quad \forall\, t \geq t_1(\|z_0\|_2)\}$$

be the absorbing set in Proposition 2. Since $\mathbf{H}^1 \subset\subset \mathbf{L}^2$ by Rellich-Kondrachov compactness theorem, B is compact in $\mathbf{L}^2$ and $\mathcal{A} = \omega(B)$ is the compact global attractor, where $\omega(B)$ denotes the ω-limit set of the set B. □

3.7 Discussion

Existence of an attractor is not really surprising, however, it confirms our earlier argument that the finite-dimensional ODE system, consisting of the PDE without the Laplacian, carries the interesting dynamics and diffusion only combines this dynamics on a spatial scale.

There are two ways to include impulse radiations into our bystander model. One idea is to stop the dynamics at a radiation event, then apply the surviving fraction due to radiation, and use the resulting population size as initial condition for the next time interval. In this iterative approach, the existence result stated in Theorem 5 (for the system describing the cellular evolution after radiation exposure) is sufficient to guarantee existence and uniqueness of solutions. Each radiation fraction would create a jump in the solution, possibly away from the attractor. The dynamics between radiations would then lead the system back onto the attractor.

Here, we focused on the approach that the radiation terms are directly included into the system of differential-equations via the hazard functions $r_u(d(t))$, $r_v(d(t))$, and $\gamma(d(t))$. In this case, the on-and-off switching of radiation introduces jump discontinuities into the model. We needed to use time-mollification to deal with these jumps. Although this second approach seems complicated, it does allow for the inclusion of arbitrary radiation schedules consisting of combinations of impulse, interval, and continuous radiations.

The parameter regime found for the existence of solutions for the system with and without radiation suggested that (1) during radiation, the rate of damage incurred both directly and indirectly does not exceed the bystander signal-induced death incurred in both damaged and healthy cells, and (2) after radiation exposure, the rate of bystander signal emission by the damaged cells does not exceed the rate of bystander signal-induced death in the damaged cells.

Chapter 4

Asymptotic analysis of bystander signal-mediated cancer invasion

Abstract. *In experimental studies, it has been shown that radiation exposure enhances the invasion of certain cell lines whose invasion speed may have been much slower without the radiation exposure. Radiation-induced bystander signals have been implicated to mediate this radiation-induced cancer invasion. Here, I examine a candidate explanation for this bystander signal-induced cancer invasion by generalizing a system of nonlinear reaction-diffusion equations that describe bystander effects in a single cell line to incorporate tumor cell lines and their surrounding normal tissue. I apply both numerical methods and a matched asymptotic analysis in a traveling wave framework to obtain an explicit understanding of the invasion of a homogeneous tumor-only population into a normal-tissue-only population with a mixed interface. I also show how fundamental parameters govern this speed and the shape of invading tumor waves. Our theoretical analysis will help to identify key parameters that control radiation-induced cancer invasion and can further suggest possible novel therapeutic strategies not yet considered.*

4.1 Introduction

Radiotherapy accounts for the treatment of more than 50% of cancers. As most tumors are surrounded by normal tissues, the standard treatment practice mediates gradients of doses to surrounding normal tissues in such a way that the farther a cell is from the targeted tumor, the lesser the magnitude of dose it receives. This invariably suggests that normal tissues surrounding solid tumors receive low doses of radiation during cancer treatment, which was considered to be acceptable.

However, recent experiments have shown that certain cell lines emit stress signals when exposed to low doses of radiation [8, 42, 49]. These signals, also known as bystander signals, can be propagated to neighboring cells to trigger effects such as cell death, cell damage, delayed DNA repair, and so on. These effects are popularly called the bystander effects. Since the discovery of the phenomenon of bystander effects, there have been concerns about its effect on tumor invasion and metastasis. This is crucial since one of the properties of cancer cells that makes it extremely deadly is its ability to migrate, settle, and survive in distant locations.

Experiments have shown that bystander signals can mediate and enhance tumor invasion into surrounding normal tissues, especially after exposure to radiation. While some of these experiments were conducted at the molecular level, others were confined to different cellular responses of cancer and normal cells to bystander signals. For instance, some experiments have been used to study different molecular pathways that can lead to radiation-induced invasiveness in many cell lines like rectal cancer cells [110], non-small cell lung carcinoma cells [37], human pancreatic cancer cells [97], glioblastoma cells [47, 19], hepatocellular carcinoma cells [18], and metastatic breast cancer cells [9]. In fact, in [9], the authors demonstrate the roles of bystander signals in the enhanced invasiveness of metastatic breast cancer by injecting breast cancer cells into the thorax of mice that were exposed to radiation an hour prior to the injection of the cancer cells. The effect was an increased spread of the cancer cells compared to the case when the thorax was not pre-irradiated.

Other experiments [25, 55, 17, 56] have also been used to study the enhanced invasiveness of cancer cells at both cellular and molecular levels by showing that some cancer cells such as lung cancer cells (A549 cells) and their surrounding normal lung cells (W138 cells) respond differently to bystander signals. In fact, the authors in [25, 55, 17, 56] showed that apart from the destructive response of normal tissues to bystander signals, they can also have a protective response. They showed that normal tissues emit a kind of rescue signals in response to bystander signals. These rescue signals trigger the healing of neighboring damaged cancer cells. This recent discovery has shown that cell-cell communication triggered by radiation can be quite complicated.

Our goal in this chapter is to model the distress signaling behaviours and the corresponding bystander effects when a tumor and their surrounding normal tissue are both exposed to low doses of radiation at a constant rate. For simplicity, we will not consider the effects of rescue signals on radiation-induced invasion in this project. The main aim is to elucidate the role of bystander signals in the observed enhanced invasiveness of tumors and to determine key parameters that can be controlled in order to possibly prevent such side effects of cancer treatment.

The work in this chapter will extend the mathematical model developed in [89] and Chapter 2 to include two cell types namely, tumor and normal cells. In [89], the model was used to analyze the persistence of the emitted bystander signals and to determine key parameters that drive the signal's persistence. The analysis framework that will be employed in this chapter is similar to those used in [29, 74], where matched asymptotic analyses in a travelling wave setting were used to elucidate the consequences of altered energy metabolism in cancer invasion. There are recent advances [122, 121] toward standard analytical methods for computing the travelling wave speeds of a general class of systems of reaction-diffusion equations. However, these analytical methods cannot be generalized to general systems of more than three reaction-diffusion equations. Thus, the analysis of the traveling wavespeed our system of four reaction-diffusion equations will rely solely on the matched asymptotic analysis. This will also help elucidate the role of the key model parameters in the invasion process.

While several mathematical models have been developed to explore the interactions between cells and bystander signals [48, 75, 93], Olobatuyi et. al [89] were the first to use the reaction-diffusion framework to study interactions between cells and bystander signals. For convenience, we reproduce the equations here, with $U(y,\tau)$ denoting the density of target cells as a function of position y and time τ, $V(y,\tau)$ the density of damaged tumor cells, and $W(y,\tau)$ the concentration of bystander signals emitted by the damaged cells. The Olobatuyi et. al equations [89] as well as in Chapter 2 are:

$$\begin{aligned}
U_\tau &= \underbrace{D_u\Delta U}_{\text{Diffusion}} + \underbrace{\mu U\Big(1-\frac{U+V}{u_0}\Big)}_{\text{Growth Dynamics}} - \underbrace{r_u(t)U - \boldsymbol{\gamma}(t)U}_{\text{Radiation effect}} \\
&\quad \underbrace{-A(W)U + F(W)V - E(W)U}_{\text{Bystander Effects}}, \qquad (4.1)\\
V_\tau &= \underbrace{D_v\Delta V}_{\text{Diffusion}} - \underbrace{r_v(t)V + \boldsymbol{\gamma}(t)U}_{\text{Radiation Effects}} - \underbrace{A(W)V - F(W)V + E(W)U}_{\text{Bystander Effects}}, \qquad (4.2)\\
W_\tau &= \underbrace{D_w\Delta W}_{\text{Diffusion}} + \underbrace{\lambda_1 r_v(t)V + \lambda_2 r_u(t)U + \lambda_3\kappa V}_{\text{Signal Emission}} - \underbrace{\eta W}_{\text{Decay}}. \qquad (4.3)
\end{aligned}$$

Here D_i denotes the diffusion constant of the respective i compartment, μ the cell proliferation rate, u_0 the tissue carrying capacity, η the signal decay rate, and λ_i the signal emission rate from the respective dead and damaged cells. The terms $r_i(t)$ and $\boldsymbol{\gamma}(t)$ denote respectively the radiation-induced death and the radiation-damage rate (readers should consult Chapter 2 for more details on the parameters).

This model will be extended to describe a tumor surrounded by normal tissues. This is similar to the framework modeled by Powathil et. al [93] with an individual-based approach, where the effects of different fractional radiation exposure strategies were considered, namely (1) when both tumor and normal tissues are exposed to uniform doses of radiation, (2) when tumor cells receive higher doses while the surrounding normal tissue receives doses inversely proportional to their distance from the tumor cells, and (3) only tumor cells are exposed to radiation and the surrounding normal tissue are completely spared. However, in order to avoid the discontinuity introduced by fractional exposure to radiation, we will assume a constant exposure of both tumor and normal tissues to the same low doses of radiation.

The remainder of this chapter is organized as follows. In Section 4.2, we formulate and develop the generalized mathematical model that describes the cellular interaction between tumor and surrounding normal tissues under constant exposure to low-dose radiation. In Section 4.3, we compute possible equilibrium points of the system under spatio-temporal invariance and also analyze their stability. In Section 4.4, we explore the numerical simulation of the traveling wave solutions of the model. We show numerically that invasion with bystander effects is faster than invasion without bystander effects. In Section 4.5, we explore the traveling wave analysis of the model using the matched asymptotic analytical method to derive an approximate invasion wave speed. This asymptotic wave speed also confirms that invasion speed with bystander effects is always greater than that without bystander effects.

These types of analyses will suggest possible control measures that can minimize or completely eradicate the side effects of cancer treatment in order to improve post-treatment patients' outcome.

4.2 Development of the generalized model

To generalize (4.1)-(4.3) to describe both tumor cells and surrounding normal tissue, which are both uniformly exposed to low doses of radiation, we incorporate two additional compartments. These are the normal tissue and the radiation-damaged normal tissue compartments. The existing compartments will be retained as tumor cells, damaged tumor cells, and bystander signals concentration.

Let $U_1(y,\tau)$ and $V_1(y,\tau)$ denote the densities of tumor and damaged tumor cells, respectively. Also, let $U_2(y,\tau)$ and $V_2(y,\tau)$ denote the densities of normal cells and damage normal cells, respectively. Let $W(y,\tau)$ remain the concentration of bystander signals. Since the growth of damaged cells is arrested in order to concentrate all their energy on repair, it makes sense to assume that energy for motility also is harnessed for repair, which makes damaged cells less diffusive. Also, normal cells are well regulated and participate normally in organs. Therefore, we assume that normal cells will not be diffusive in space

[33]. Denoting with subscript '1' the parameters associated with tumor cells, and subscript '2' the parameters belonging to normal tissue, the new system of reaction-diffusion partial differential equations (PDEs) is given by

$$\begin{aligned}
U_{1_\tau} &= D_1 U_{yy} + \bar{\mu}_1 U_1 \Big(1 - \frac{U_1 + V_1 + \bar{\alpha} U_2 + \bar{\alpha}_1 V_2}{u_{10}}\Big) \\
&\quad - (\bar{A}_1(W) + \bar{E}_1(W) + \bar{\gamma}_1 + \bar{r}_1) U_1 + \bar{F}_1(W) V_1, && (4.4)\\
V_{1_\tau} &= (\bar{\gamma}_1 + \bar{E}_1(W)) U_1 - (\bar{A}_1(W) + \bar{F}_1(W) + \bar{r}_1) V_1, && (4.5)\\
U_{2_\tau} &= \bar{\mu}_2 U_2 \Big(1 - \frac{U_2 + V_2 + \bar{\beta}_1 U_1 + \bar{\beta}_2 V_1}{u_{20}}\Big) \\
&\quad - (\bar{A}_2(W) + \bar{E}_2(W) + \bar{\gamma}_2 + \bar{r}_2) U_2 + \bar{F}_2(W) V_2, && (4.6)\\
V_{2_\tau} &= (\bar{\gamma}_2 + \bar{E}_2(W)) U_2 - (\bar{A}_2(W) + \bar{F}_2(W) + \bar{r}_2) V_2, && (4.7)\\
W_\tau &= D_w W_{yy} + \delta_1(\bar{\kappa}_1 + \bar{r}_1) V_1 + \delta_2(\bar{\kappa}_2 + \bar{r}_2) V_2 \\
&\quad + \delta_1 \bar{r}_1 U_1 + \delta_2 \bar{r}_2 U_2 - \eta W, && (4.8)
\end{aligned}$$

where D_1 denotes the diffusion constant of tumor cells, $\bar{\mu}_1$ the proliferation rate of tumor cells, u_{10} the tumor cell carrying capacity, $\bar{\gamma}_1$ the constant rate of radiation damage of the tumor cells, and $\bar{r}_1$ the radiation-induced tumor death rate. With a change of subscript from '1' to '2', we have the same parameters for the normal tissue. The rates for the bystander signal-induced death, bystander signal-induced damage, and the bystander signal-dependent repair are denoted respectively by $\bar{A}_i(W)$, $\bar{E}_i(W)$, and $\bar{F}_i(W)$. As in Chapter 2, their functional forms are given by

$$\begin{aligned}
\bar{A}_i(W) &= \frac{\bar{A}_{i0}}{2}\Big[1 + \tanh\Big(\frac{6}{a_{i2} - a_{i1}}\big(W - \frac{a_{i1} + a_{i2}}{2}\big)\Big)\Big], && (4.9)\\
\bar{E}_i(W) &= \frac{\bar{E}_{i0}}{2}\Big[1 + \tanh\Big(\frac{6}{e_{i2} - e_{i1}}\big(W - \frac{e_{i1} + e_{i2}}{2}\big)\Big)\Big], && (4.10)\\
\bar{F}_i(W) &= \frac{\bar{F}_{i0}}{2}\Big[1 - \tanh\Big(\frac{6}{f_{i2} - f_{i1}}\big(W - \frac{f_{i1} + f_{i2}}{2}\big)\Big)\Big]. && (4.11)
\end{aligned}$$

The parameters a_{ij}, e_{ij}, and f_{ij} denote the lower and upper thresholds for the respective bystander effects. The dead and damaged cells emit bystander signals at rates δ_i ($i = 1$ for tumor and $i = 2$ for normal tissue). We denote by $\bar{\kappa}_i$ the fraction of damaged cells ($i = 1$ for tumor and $i = 2$ for normal tissue) emitting bystander signals. $\bar{\alpha}$ denotes the relative competitive potential of normal tissue with the tumor cells, while $\bar{\beta}_1$ and $\bar{\beta}_2$ denote the relative competitive potential of tumor and their damaged cells with the normal tissue, respectively.

The remainder of this section will focus on simplifying assumptions to reduce the model complexity and the model's non-dimensionalization.

4.2.1 Simplifying assumptions

In order to simplify the model, we will make the following simplifying assumptions:

- Damaged normal cells do not significantly contribute to the emission of bystander signal. This make sense in the case of normal lung (W138) cells which were found to emit almost negligible concentrations of bystander signals when co-cultured with both irradiated lung cancer and normal cells, respectively [25]. Thus, we will not be keeping track of the damaged normal tissue and we can omit compartment V_2 in the model.

- The conversion factor from bystander signal-producing tumor and normal cells to bystander signals is the same. Thus,

$$\delta := \delta_1 = \delta_2.$$

- The diffusive coefficient for tumor cells is far less than that of the bystander signals. That is, $D_1 \ll D_w$.

- The radiation terms $\bar{r}_{1,2}$ and $\bar{\gamma}_1$ are nonnegative constants. $\bar{r}_{1,2}, \bar{\gamma}_1 > 0$ correspond to constant low-dose radiation, and $\bar{r}_{1,2} = \bar{\gamma}_1 = 0$ to no radiation.

- Since radiation damage rates at constant low-dose radiation are possibly small, we will assume that

$$\bar{\gamma} + \bar{E}_1(W) \ll 1 + \frac{\bar{F}_1(W)}{\bar{A}_1(W) + \bar{r}_1}. \tag{4.12}$$

Eqn. (4.12) will be useful during the stability analysis of the model in Section 4.3.1.

- $\bar{\beta}_{1,2}$, the competitive strength of damaged and undamaged tumor cells are greater than α, the competitive strength of the normal cells, to reflect tumor aggressiveness, which is one of the hallmarks of cancer [39, 40]. Thus $\bar{\alpha} \leq \bar{\beta}_{1,2}$.

- Tumor cells produce more bystander signals but are more resistant to these signals than the surrounding normal cells. This assumption is due to the resistant nature of tumor cells to radiation. Thus $a_{11} \leq a_{21}$, and $\bar{A}_{20} \leq \bar{A}_{10}$.

- In the computation of the radiation terms, we employ

$$\begin{aligned} \bar{r}_i &= (\alpha_i + \beta_i d) d_r, && (4.13) \\ \bar{\gamma} &= \frac{2\gamma_0 \sigma d_r}{1 + (\sigma d_r)^2}, && (4.14) \end{aligned}$$

  where d and d_r denote the dose and the constant dose rate, respectively. α_i is the rate at which single radiation tracks produce lethal lesion, and β_i is the rate at which binary misrepair of pairs of double strand break (DSB) from different radiation tracks lead to lethal lesions [12]. For details about the nonnegative terms γ_0 and σ, please refer to Chapter 2.

Then model (4.4) - (4.8) simplifies to

$$\begin{aligned} U_{1_\tau} &= D_1 U_{yy} + \bar{\mu}_1 U_1 \Big(1 - \frac{U_1 + V_1 + \bar{\alpha} U_2}{u_{10}} \Big) \\ &\quad - (\bar{A}_1(W) + \bar{E}_1(W) + \bar{\gamma}_1 + \bar{r}_1) U_1 + \bar{F}_1(W) V_1, && (4.15) \\ V_{1_\tau} &= (\bar{\gamma}_1 + \bar{E}_1(W)) U_1 - (\bar{A}_1(W) + \bar{F}_1(W) + \bar{r}_1) V_1, && (4.16) \\ U_{2_\tau} &= \bar{\mu}_2 U_2 \Big(1 - \frac{U_2 + \bar{\beta}_1 U_1 + \bar{\beta}_2 V_1}{u_{20}} \Big) - (\bar{A}_2(W) + \bar{r}_2) U_2, && (4.17) \\ W_\tau &= D_w W_{yy} + \delta(\bar{\kappa}_1 + \bar{r}_1) V_1 + \delta \bar{r}_1 U_1 + \delta \bar{r}_2 U_2 - \eta W, && (4.18) \end{aligned}$$

Parameter	Value	Units	Source
$\bar{\mu}_1$	3.6e-03	h^{-1}	[33]
$\bar{\mu}_2$	3.6e-03	h^{-1}	[33]
u_{10}	5e+07	cm^{-3}	[114]
u_{20}	5e+07	cm^{-3}	[114]
D_1	7.2e-07	cm^2h^{-1}	[24]
D_w	7.2e-03	cm^2h^{-1}	[4, 75]
$\bar{\alpha}$	$\mathcal{O}(1)$	Dimensionless	Chosen freely
δ	6.6e0-3	h^{-1}	[75]
η	1.26	h^{-1}	[75]
$\bar{\beta}_1$	$\mathcal{O}(1)$	Dimensionless	Chosen freely
$\bar{\beta}_2$	$\mathcal{O}(1)$	Dimensionless	Chosen freely
$\bar{\kappa}_1$	0.5	$-$	[93]
$\bar{A}_{10}$	0.63	h^{-1}	[89]
$\bar{A}_{20}$	0.88	h^{-1}	[89]
$\bar{E}_{10}$	0.168	h^{-1}	[89]
$\bar{F}_{10}$	0.432	h^{-1}	[89]
a_{11}	0.05	Dimensionless	[89]
a_{21}	0.01	Dimensionless	Chosen freely

Table 4.1: Definition and values of dimensional parameters in system (4.15) - (4.18).

4.2.2 Non-dimensionalization

By applying the following transformations:

$$u_i = \frac{U_i}{u_{i_0}},\ v = \frac{V_1}{u_{10}},\ w = \frac{W}{\delta u_{10}},\ x = \sqrt{\frac{\eta}{D_w}}y,\ t := \eta\tau, \tag{4.19}$$

equations (4.15) - (4.18) become

$$\begin{aligned}
u_{1_t} &= Du_{1_{xx}} + \mu_1 u_1(1 - u_1 - v - \alpha u_2) \\
&\quad - (A_1(w) + E_1(w) + \gamma_1 + r_1)u_1 + F_1(w)v, && (4.20) \\
v_t &= (\gamma_1 + E_1(w))u_1 - (A_1(w) + F_1(w) + r_1)v, && (4.21) \\
u_{2_t} &= \mu_2 u_2(1 - u_2 - \beta_1 u_1 - \beta_2 v) - (A_2(w) + r_2)u_2, && (4.22) \\
w_t &= w_{xx} + (\kappa_1 + r_1)v + r_1 u_1 + r_2 u_2 - w, && (4.23)
\end{aligned}$$

Parameter	Value or range	Constraint	Derivation
$\mu_{1,2}$	2.9e-03		$\frac{\bar{\mu}_{1,2}}{\eta}$
D	1e-04	$D_1 \ll D_w$	$\frac{D_1}{D_w}$
α	$\mathcal{O}(1)$	$\alpha \leq \beta_i$	$\frac{\bar{\alpha} u_{20}}{u_{10}}$
$\beta_{1,2}$	$\mathcal{O}(1)$	$\beta_2 \leq \beta_1$	$\frac{\bar{\beta}_i u_{1_0}}{u_{20}}$
κ_1	0.3968		$\frac{\bar{\kappa_1}}{\eta}$
r_1	1e-03		$\frac{\bar{r_1}}{\eta}$
r_2	4.8e-04		$\frac{\bar{r_2}}{\eta}$
γ	0.0794		$\frac{\bar{\gamma}_1}{\eta}$
A_{10}	0.28 - 1.14	$A_{10} \leq A_{20}$	$\frac{\bar{A}_{10}}{\eta}$
A_{20}	0.7		$\frac{\bar{A}_{20}}{\eta}$
E_{10}	0.1333		$\frac{\bar{E}_{1_0}}{\eta}$
F_{10}	0.26 - 0.88		$\frac{\bar{F}_{10}}{\eta}$

Table 4.2: Values of dimensionless parameters in system (4.20) - (4.23).

where

$$D := \frac{D_1}{D_w},\ \mu_i := \frac{\bar{\mu}_i}{\eta},\ A_{i_0} := \frac{\bar{A}_{i_0}}{\eta},\ E_{10} := \frac{\bar{E}_{1_0}}{\eta},\ \alpha := \frac{\bar{\alpha}u_{20}}{u_{10}},$$
$$\beta_i := \frac{\bar{\beta}_i u_{1_0}}{u_{20}},\ \gamma_1 := \frac{\bar{\gamma}_1}{\eta},\ r_i := \frac{\bar{r}_i}{\eta},\ \kappa_i := \frac{\bar{\kappa_1}}{\eta}\ F_{10} := \frac{\bar{F}_{1_0}}{\eta}.$$

The dimensional and dimensionless (based on the above transformation) parameters are shown in Table 4.1 and 4.2.

4.3 Steady state analysis

In this section, we will compute all the possible steady states of the system (4.20)-(4.23) under spatial and temporal invariance, as well as their respective stability analyses.

4.3.1 Possible equilibrium points

In this subsection, we examine system (4.20)-(4.23) under spatial and temporal invariance to investigate the attainable types of behaviour under different choices of model parameters. We will solve the following system of equations

$$\begin{aligned} 0 &= \mu_1 u_1(1-u_1-v-\alpha u_2) \\ &\quad -(A_1(w)+E_1(w)+\gamma_1+r_1)u_1+F_1(w)v, && (4.24)\\ 0 &= (\gamma_1+E_1(w))u_1-(A_1(w)+F_1(w)+r_1)v, && (4.25)\\ 0 &= \mu_2 u_2(1-u_2-\beta_1 u_1-\beta_2 v)-(A_2(w)+r_2)u_2, && (4.26)\\ 0 &= (\kappa_1+r_1)v+r_1u_1+r_2u_2-w. && (4.27)\end{aligned}$$

From (4.25),

$$u_1 = m_1 v, \qquad (4.28)$$

where

$$m_1 := \frac{F_1 + A_1 + r_1}{\gamma_1 + E_1}. \tag{4.29}$$

From (4.26),

$$u_2 = 0 \quad \text{or} \quad \mu_2(1 - u_2 - \beta_1 u_1 - \beta_2 v) - A_2 - r_2 = 0.$$

If $u_2 = 0$, then from (4.24) and (4.28) we have

$$\mu_1 m_1 v(1 - m_1 v - v) - (A_1 + E_1 + \gamma_1 + r_1) m_1 v + F_1 v \quad = \quad 0,$$

which implies that

$$v = 0 \quad \text{or} \quad \mu_1 m_1(1 - m_1 v - v) - (A_1 + E_1 + \gamma_1 + r_1) m_1 + F_1 = 0.$$

If $v = 0$, then there exists a trivial equilibrium point

$$P_0 = (0, 0, 0, 0).$$

On the other hand, if

$$\mu_1 m_1(1 - m_1 v - v) - (A_1 + E_1 + \gamma_1 + r_1) m_1 + F_1 = 0,$$

then there exists a tumor-signal equilibrium point

$$P_1 = (m_1 v_1^*, v_1^*, 0, w_1^*),$$

where

$$\begin{aligned} v_1^* &= \frac{\mu_1 m_1 - m_1(A_1 + E_1 + \gamma_1 + r_1) + F_1}{\mu_1 m_1(m_1 + 1)} \\ &= (\gamma_1 + E_1)\Big[\frac{1}{A_1 + E_1 + \gamma_1 + r_1 + F_1} - \frac{A_1 + r_1}{\mu_1(A_1 + F_1 + r_1)}\Big], \end{aligned} \tag{4.30}$$

which is nonnegative provided that

$$\frac{A_1 + r_1}{\mu_1} < \frac{A_1 + F_1 + r_1}{A_1 + E_1 + \gamma_1 + r_1 + F_1} < 1. \tag{4.31}$$

Condition (4.31) implies that

$$A_1 + r_1 < \mu_1. \tag{4.32}$$

Then we have

$$u_1^* = \frac{A_1 + F_1 + r_1}{A_1 + E_1 + \gamma_1 + r_1 + F_1} - \frac{A_1 + r_1}{\mu_1}$$

and w_1^* satisfies the expression

$$w = (r_1 + \kappa_1)v_1^* + r_1 u_1^*. \tag{4.33}$$

Remark 1. *Condition (4.32) implies that the cumulative rate of cell death induced from both the direct (radiation-induced) and the indirect effects (bystander signal-induced) is less than its proliferative rate. Otherwise, the tumor will go extinct.*

On the other hand, if

$$\mu_2(1 - u_2 - \beta_1 u_1 - \beta_2 v) - A_2 - r_2 = 0, \tag{4.34}$$

then substituting (4.29) into (4.24), we have

$$v = 0 \quad \text{or} \quad \mu_1 m_1(1 - m_1 v - v - \alpha u_2) - (A_1 + E_1 + \gamma_1 + r_1)m_1 + F_1 = 0.$$

If $v = 0$, then from (4.28), $u_1 = 0$. From (4.34), we have

$$\mu_2(1 - u_2) - A_2 - r_2 = 0,$$

which implies

$$u_2^* \quad = \quad 1 - \frac{r_2}{\mu_2} - \frac{A_2}{\mu_2},$$

which is nonnegative provided

$$r_2 + A_2(w_2^*) < \mu_2. \qquad (4.35)$$

From (4.27), we then have

$$w = r_2\Big(1 - \frac{r_2}{\mu_2} - \frac{A_2}{\mu_2}\Big). \qquad (4.36)$$

Thus, there exists a no-tumor equilibrium point

$$P_2 = (0, 0, u_2^*, w_2^*),$$

where w_2^* satisfies the expression in (4.36).

Remark 2. *Equilibrium P_2 exists provided the cumulative rate of normal cell death induced from both the direct and the indirect effects of radiation is less than its proliferation rate. Otherwise, the normal tissue will go extinct.*

Finally, if

$$\mu_1 m_1(1 - m_1 v - v - \alpha u_2) - (A_1 + E_1 + \gamma_1 + r_1)m_1 + F_1 = 0, \qquad (4.37)$$

then from (4.34), u_2 can be solved in terms of v as follows:

$$u_2^{**} = 1 - v_3^*(\beta_1 m_1 + \beta_2) - \frac{1}{\mu_2}(r_2 + A_2), \qquad (4.38)$$

provided

$$v(\beta_1 m_1 + \beta_2) + \frac{1}{\mu_2}(r_2 + A_2) < 1.$$

Thus, if (4.35) holds, then (4.38) holds if

$$v(\beta_1 m_1 + \beta_2) < 1.$$

Substituting (4.38) into (4.37), we can solve for v as follows:

$$v_3^* = \frac{\mu_1 m_1(1 + \frac{\alpha}{\mu_2}(r_2 + A_2) - \alpha) + F_1 - m_1(A_1 + E_1 + \gamma_1 + r_1)}{\mu_1 m_1(1 + m_1 - \alpha(\beta_1 m_1 + \beta_2))} \tag{4.39}$$

provided $v_3^* > 0$ and

$$1 + m_1 - \alpha(\beta_1 m_1 + \beta_2) \neq 0. \tag{4.40}$$

If $\beta_1 = \beta_2 := \beta$, then (4.40) implies that $\alpha\beta \neq 1$ and v_3^* becomes

$$\begin{aligned} v_3^* &= \frac{\mu_1 m_1(1 + \frac{\alpha}{\mu_2}(r_2 + A_2) - \alpha) + F_1 - m_1(A_1 + E_1 + \gamma_1 + r_1)}{\mu_1 m_1(1 + m_1)(1 - \alpha\beta)} \\ &= \frac{\gamma_1 + E_1}{1 - \alpha\beta}\Big[\frac{1 + \alpha(\frac{r_2 + A_2}{\mu_2} - 1)}{A_1 + r_1 + F_1 + \gamma_1 + E_1} - \frac{\frac{A_1 + r_1}{\mu_1}}{F_1 + A_1 + r_1}\Big]. \end{aligned} \tag{4.41}$$

Thus, for (4.41) to exist, we must have the following conditions

$$\begin{cases} \frac{1+\alpha\left[\frac{r_2+A_2}{\mu_2}-1\right]}{\frac{1}{\mu_1}(A_1+r_1)} < \frac{A_1+r_1+F_1+\gamma_1+E_1}{F_1+A_1+r_1}; & \alpha\beta > 1, \\ \frac{1+\alpha\left[\frac{r_2+A_2}{\mu_2}-1\right]}{\frac{1}{\mu_1}(A_1+r_1)} > \frac{A_1+r_1+F_1+\gamma_1+E_1}{F_1+A_1+r_1}; & \alpha\beta < 1. \end{cases} \tag{4.42}$$

Of course,

$$\begin{cases} \alpha\beta > 1 \Rightarrow & (\alpha > 1,\ \beta < 1),\ (\alpha < 1,\ \beta > 1) \text{ or } 1 < \alpha < \beta \\ \alpha\beta < 1 \Rightarrow & (\alpha > 1,\ \beta < 1),\ (\alpha < 1,\ \beta > 1) \text{ or } 0 < \alpha < \beta < 1. \end{cases} \tag{4.43}$$

However, since tumors are known to be more aggressive than the normal cells, we will assume that $\alpha < \beta$. Thus, the choices in (4.43) reduce to

$$\begin{cases} \alpha\beta > 1 \Rightarrow & (\alpha < 1,\ \beta > 1) \text{ or } 1 < \alpha < \beta; \\ \alpha\beta < 1 \Rightarrow & (\alpha < 1,\ \beta > 1) \text{ or } 0 < \alpha < \beta < 1. \end{cases} \tag{4.44}$$

Substituting (4.41) into (4.38), we have

$$u_2^{**} = \frac{1}{1-\alpha\beta}\Big[1-\beta-\frac{r_2+A_2}{\mu_2}+\beta\Big(\frac{A_1+r_1}{\mu_1}\Big)\Big(\frac{A_1+E_1+F_1+\gamma_1+r_1}{F_1+A_1+r_1}\Big)\Big], \tag{4.45}$$

which exists provided

$$\begin{cases} 1+\beta\Big(\frac{A_1+r_1}{\mu_1}\Big)\Big(\frac{A_1+E_1+F_1+\gamma_1+r_1}{F_1+A_1+r_1}\Big) < \beta+\frac{r_2+A_2}{\mu_2}, & \alpha\beta>1, \\ \beta+\frac{r_2+A_2}{\mu_2} < 1+\beta\Big(\frac{A_1+r_1}{\mu_1}\Big)\Big(\frac{A_1+E_1+F_1+\gamma_1+r_1}{F_1+A_1+r_1}\Big), & \alpha\beta<1. \end{cases} \tag{4.46}$$

Since $u_1^{**}=m_1v_3^*$, we also the following expression for u_1^{**}:

$$u_1^{**} = \frac{1}{1-\alpha\beta}\Big[\frac{(A_1+F_1+r_1)\big(1+\alpha(\frac{r_2+A_2}{\mu_2}-1)\big)}{A_1+r_1+F_1+\gamma_1+E_1}-\frac{A_1+r_1}{\mu_1}\Big]. \tag{4.47}$$

Thus, there exists an heterogeneous equilibrium point

$$P_3=(u_1^{**},v_3^*,u_2^{**},w_3^*),$$

with v_3^* defined in (4.41), u_2^{**} defined in (4.38), and w_3^* satisfing the expression

$$w=r_2u_2^{**}+(r_1+\kappa_1)v_3^*+r_1u_1^{**}.$$

If $\alpha\beta<1$, then from (4.42), we have

$$\frac{\frac{1}{\mu}(A_1+r_1)}{1+\alpha\big[\frac{r_2+A_2}{\mu_2}-1\big]} \ < \ \frac{F_1+A_1+r_1}{A_1+r_1+F_1+\gamma_1+E_1} \ < \ 1,$$

which implies

$$\frac{1}{\mu}(A_1+r_1) \ < \ \Big(\frac{F_1+A_1+r_1}{A_1+r_1+F_1+\gamma_1+E_1}\Big)\Big(1+\alpha\big[\frac{r_2+A_2}{\mu_2}-1\big]\Big).$$

If $r_2+A_2<\mu_2$, then α, the normal tissue competitive potential is key in determining the cumulative rate of cell death relative to tumor proliferation rate that guarantees the existence of P_3 whenever $\alpha\beta<1$. Also, in order to ensure that $\frac{A_1+r_1}{\mu_1}$ is nonnegative, we must have

$$-1 < \alpha\Big[\frac{r_2 + A_2}{\mu_2} - 1\Big] < 0,$$

which implies

$$0 < 1 - \frac{1}{\alpha} < \frac{r_2 + A_2}{\mu_2} < 1.$$

Thus, if $\alpha\beta < 1$, we have a lower bound for the ratio of the cumulative death rate to the proliferation rate for the normal tissue in order for the heterogeneous equilibrium point P_3 to exist. The lower bound implies that $\alpha > 1$. Thus, the conditions (4.44) already exclude the possibility of $\alpha\beta < 1$. This is essentially due to the standing assumption that tumors are more aggressive (relatively competitive) than normal cells. On the other hand, if $\alpha\beta > 1$, there is no restriction on either α or β in order to ensure the existence of P_3.

We summarize the equilibrium points of system (4.20)-(4.23) under spatial and temporal invariance in tabular form in Table 4.3.

4.3.2 Stability analysis of the equilibrium points

The objective of this section is to determine the stability of the equilibrium points derived in the previous subsection.

Stability of P_0

The Jacobian matrix corresponding to this equilibrium point is

$$J(P_0) = \\ \begin{pmatrix} \mu_1 - A_1(0) - E_1(0) - \gamma_1 - r_1 & F_{10} & 0 & 0 \\ \gamma_1 + E_1(0) & -F_{10} - A_1(0) - r_1 & 0 & 0 \\ 0 & 0 & \mu_2 - A_2(0) - r_2 & 0 \\ r_1 & r_1 + \kappa_1 & r_2 & -1 \end{pmatrix}.$$

Symbol	Expression
P_0	$(0,0,0,0)$
P_1	$(u_1^*, v_1^*, 0, w_1^*)$ where $u_1^* = \frac{A_1+F_1+r_1}{A_1+E_1+\gamma_1+r_1+F_1} - \frac{A_1+r_1}{\mu_1}$, $v_1^* = (\gamma_1 + E_1)\Big[\frac{1}{A_1+E_1+\gamma_1+r_1+F_1} - \frac{A_1+r_1}{\mu_1(A_1+F_1+r_1)}\Big]$, and w_1^* solves $w = (r_1+\kappa_1)v_1^* + +r_1u_1^*$. Existence condition: $\frac{A_1+r_1}{\mu_1} < \frac{A_1+F_1+r_1}{A_1+E_1+\gamma_1+r_1+F_1}$
P_2	$(0,0,u_2^*,w_2^*)$, where $u_2^* = 1 - \frac{r_2}{\mu_2} - \frac{A_2(w_2^*)}{\mu_2}$, w_2^* satisfies $w = r_2\Big(1 - \frac{r_2}{\mu_2} - \frac{A_2(w)}{\mu_2}\Big)$. Existence condition: $r_2 + A_2(w_2^*) < \mu_2$.
P_3	$(u_1^{**}, v_3^*, u_2^{**}, w_3^*)$, where $u_1^{**} = \frac{1}{1-\alpha\beta}\Big[\frac{(A_1+F_1+r_1)\big(1+\alpha(\frac{r_2+A_2}{\mu_2}-1)\big)}{A_1+r_1+F_1+\gamma_1+E_1} - \frac{A_1+r_1}{\mu_1}\Big]$, $v_3^* = \frac{\gamma_1+E_1}{1-\alpha\beta}\Big[\frac{1+\alpha(\frac{r_2+A_2}{\mu_2}-1)}{A_1+r_1+F_1+\gamma_1+E_1} - \frac{\frac{A_1+r_1}{\mu_1}}{F_1+A_1+r_1}\Big]$, $u_2^{**} = \frac{1}{1-\alpha\beta}\Big[1 - \beta - \frac{r_2+A_2}{\mu_2} + \beta\Big(\frac{A_1+r_1}{\mu_1}\Big)\Big(\frac{A_1+E_1+F_1+\gamma_1+r_1}{F_1+A_1+r_1}\Big)\Big]$, and w_3^* satisfies $w = r_2u_2^{**} + (r_1+\kappa_1)v_3^* + r_1u_1^{**}$. Existence conditions are: $\alpha\beta > 1$, $\frac{\frac{1}{\mu_1}(A_1+r_1)}{1+\alpha\big[\frac{r_2+A_2}{\mu_2}-1\big]} > \frac{F_1+A_1+r_1}{A_1+r_1+F_1+\gamma_1+E_1}$, and $1 + \beta\Big(\frac{A_1+r_1}{\mu_1}\Big)\Big(\frac{A_1+E_1+F_1+\gamma_1+r_1}{F_1+A_1+r_1}\Big) < \beta + \frac{r_2+A_2}{\mu_2}$.

Table 4.3: Notations and expressions for the equilibrium points for the system (4.24) - (4.27) under temporal and spatial invariance. For clarity, we omit the $w-$ dependence. The equilibrium points are evaluated at the respective equilibrium point for the signal w_i^*, where i depends on the P_i.

The corresponding eigenvalues are $\lambda = -1$,

$$\lambda = \mu_2 - (A_2(0) + r_2), \tag{4.48}$$

and the rest satisfy

$$\lambda^2 + \lambda(-a_a - a_b) + a_a a_b - F_{10}(\gamma_1 + E_1(0)) = 0, \tag{4.49}$$

where

$$\begin{aligned} a_a &= -(F_{10} + A_1(0) + r_1), \\ a_b &= \mu_1 - A_1(0) - E_1(0) - \gamma_1 - r_1. \end{aligned}$$

By using the Routh-Hurwitz criterion, we have the following stability theorem:

Theorem 9. P_0 *is locally asymptotically stable provided*

$$A_2(0) + r_2 > \mu_2, \text{ and} \tag{4.50}$$

$$A_1(0) + r_1 > \mu_1. \tag{4.51}$$

Biological meaning: If the radiation-induced death in both the tumor and the normal cells exceed their respective proliferation rates, all cells will eventually go extinct.

Proof of Theorem 9: The eigenvalue (4.48) is negative provided (4.50) holds. Also by the Routh-Hurwitz criterion, (4.49) has all negative eigenvalues provided

$$F_{10} + 2(A_1(0) + r_1) > \mu_1 - E_1(0) - \gamma_1 \tag{4.52}$$

$$(A_1(0) + r_1)(A_1(0) + E_1(0) + \gamma_1 + r_1 - \mu_1) > F_{10}(\mu_1 - A_1(0) - r_1). \tag{4.53}$$

It is easy to see that (4.53) and (4.52) are both positive when (4.51) holds. □

Stability of P_1

The Jacobian matrix corresponding to this equilibrium point is

$$J(P_1) = \begin{pmatrix} a_{11} & a_{12} & a_{13} & a_{14} \\ a_{21} & a_{22} & 0 & a_{24} \\ 0 & 0 & a_{33} & 0 \\ r_1 & a_{42} & r_2 & -1 \end{pmatrix},$$

where

$$\begin{aligned} a_{11} &= -\frac{F_1}{m_1} - \mu_1 m_1 v_1^*, \quad a_{12} = F_1 - \mu_1 m_1 v_1^*, \\ a_{14} &= -((A_1' + E_1')m_1 - F_1')v_1^*, \quad a_{22} = -(F_1 + A_1 + r_1), \\ a_{33} &= \mu_2(1 - \beta_1 m_1 v_1^* - \beta_2 v_1^*) - (A_2 + r_2), \\ a_{42} &= r_1 + \kappa_1, \quad a_{21} = \gamma_1 + E_1, \quad a_{24} = -v_1^*(F_1' + A_1' - E_1' m_1). \end{aligned} \tag{4.54}$$

The corresponding characteristic polynomial is given by

$$(a_{33} - \lambda)\big[\lambda^3 + \lambda^2 \mathcal{A}_2 + \lambda \mathcal{A}_1 + \mathcal{A}_0\big] = 0,$$

where

$$\mathcal{A}_2 = 1 + \frac{F_1}{m_1} + \mu_1 m_1 v_1^* + F_1 + A_1 + r_1, \tag{4.55}$$

$$\begin{aligned} \mathcal{A}_1 = {} & \frac{F_1}{m_1} + \mu_1 m_1 v_1^* + F_1 + A_1 + r_1 + \Big(\frac{F_1}{m_1} + \mu_1 m_1 v_1^*\Big)(F_1 + A_1 + r_1) \\ & - (\gamma_1 + E_1)(F_1 - \mu_1 m_1 v_1^*) + r_1 v_1^*((A_1' + E_1')m_1 - F_1') \\ & + v_1^*(r_1 + \kappa_1)(F_1' + A_1' - E_1' m_1), \end{aligned} \tag{4.56}$$

$$\begin{aligned} \mathcal{A}_0 = {} & \Big(\frac{F_1}{m_1} + \mu_1 m_1 v_1^*\Big)(F_1 + A_1 + r_1) - (\gamma_1 + E_1)(F_1 - \mu_1 m_1 v_1^*) \\ & + (F_1' + A_1' - E_1' m_1)v_1^*\Big(r_1(\frac{F_1}{m_1} + 1) + \kappa_1(\frac{F_1}{m_1} + \mu_1 m_1 v_1^*)\Big) \\ & + ((A_1' + E_1')m_1 - F_1')v_1^*\Big((\gamma_1 + E_1)(r_1 + \kappa_1) + r_1(F_1 + A_1 + r_1 + 1)\Big). \end{aligned} \tag{4.57}$$

This implies that one eigenvalue is

$$\lambda_1 \;=\; \frac{\mu_1}{1-\alpha\beta}\Big[1-\beta-\frac{r_2+A_2}{\mu_2}+\beta\Big(\frac{A_1+r_1}{\mu_1}\Big)\Big(\frac{A_1+E_1+F_1+\gamma_1+r_1}{F_1+A_1+r_1}\Big)\Big],$$

while the others satisfy the expression

$$\lambda^3+\lambda^2\mathcal{A}_2+\lambda\mathcal{A}_1+\mathcal{A}_0=0. \tag{4.58}$$

If $\lambda_1>0$, then P_1 is locally unstable. Depending on the values of $\alpha\beta$, this is the case whenever

$$\begin{cases} 1+\beta\Big(\frac{A_1+r_1}{\mu_1}\Big)\Big(\frac{A_1+E_1+F_1+\gamma_1+r_1}{F_1+A_1+r_1}\Big)<\beta+\frac{r_2+A_2}{\mu_2}, & \alpha\beta>1,\\ \beta+\frac{r_2+A_2}{\mu_2}<1+\beta\Big(\frac{A_1+r_1}{\mu_1}\Big)\Big(\frac{A_1+E_1+F_1+\gamma_1+r_1}{F_1+A_1+r_1}\Big), & \alpha\beta<1. \end{cases} \tag{4.59}$$

Notice that the conditions in (4.59) are similar to those in (4.46). This implies that whenever equilibrium P_3 exists, equilibrium point P_1 is unstable. On the other hand, P_1 is locally asymptotically stable whenever the eigenvalues of (4.58) are all negative. By the Routh-Hurwitz criterion, all the eigenvalues of (4.58) are negative provided $\mathcal{A}_2>0,\ \mathcal{A}_0>0$ and $\mathcal{A}_2\mathcal{A}_1>\mathcal{A}_0$.

Since $\mathcal{A}_2>0$ clearly holds, then P_1 is locally asymptotically stable only whenever $\mathcal{A}_0>0$ and $\mathcal{A}_2\mathcal{A}_1>\mathcal{A}_0$. To this end, while employing the notations in (4.54) for clarity and simplicity, we have

$$\mathcal{A}_2\mathcal{A}_1=\mathcal{A}_0+\mathcal{E},$$

where

$$\begin{aligned}\mathcal{E} \;=\;& -(a_{11}+a_{22})(1-a_{11}-a_{22}+a_{11}a_{22}-a_{21}a_{12})+a_{14}(a_{21}a_{42}+r_1a_{11})\\ &+a_{24}\Big(r_1\frac{F_1}{m_1}-\kappa_1(1-a_{22})+r_1(a_{11}+a_{22})\Big).\end{aligned}$$

Thus, P_1 is locally asymptotically stable provided

$$\begin{aligned}a_{11}a_{22}-a_{21}a_{12} \;>\;& a_{24}\Big[r_1\Big(\frac{F_1}{m_1}+1\Big)-\kappa_1a_{11}\Big]\\ &+a_{14}\big[a_{21}a_{42}+r_1(1-a_{22})\big]\end{aligned} \tag{4.60}$$

and

$$
\begin{aligned}
a_{24}\Big[r_1\frac{F_1}{m_1}-\kappa_1(1-a_{22})+r_1(a_{11}+a_{22})\Big] \quad > \quad & (a_{11}+a_{22})(1-a_{11}-a_{22}\\
& +a_{11}a_{22}-a_{21}a_{12})\\
& -a_{14}(a_{21}a_{42}+r_1a_{11}). \ (4.61)
\end{aligned}
$$

By adding (4.60) - (4.61), we have

$$(1-a_{11}-a_{22})\big[-a_{24}(r_1+\kappa_1)-r_1a_{14}+a_{11}a_{22}-a_{12}a_{21}-a_{11}-a_{22}\big]>0.$$

However, since $1-a_{11}-a_{22}>0$, we have

$$a_{11}a_{22}-a_{11}-a_{22}>a_{24}(r_1+\kappa_1)+r_1a_{14}+a_{12}a_{21}. \qquad (4.62)$$

Hence, P_1 is locally asymptotically stable provided that (4.60) and (4.62) hold.

Stability of P_2

The Jacobian matrix corresponding to this equilibrium point is

$$J(P_2)=\begin{pmatrix}\mu_1(1-\alpha u_2^*)-(A_1+E_1+\gamma_1+r_1) & F_1 & 0 & 0\\ \gamma_1+E_1 & -(F_1+A_1+r_1) & 0 & 0\\ -\mu_2\beta_1u_2^* & -\mu_2\beta_2u_2^* & -\mu_2 & -A_2'u_2^*\\ r_1 & r_1+\kappa_1 & r_2 & -1\end{pmatrix}.$$

The corresponding characteristic polynomial is given by

$$
\begin{aligned}
&\big[(\lambda+1)(\lambda+\mu_2)-A_2'u_2^*r_2\big]\\
&\big[\big(\mu_1(\alpha u_2^*-1)+A_1+E_1+\gamma_1+r_1+\lambda\big)(F_1+A_1+r_1+\lambda)-F_1(\gamma_1+E_1)\big]=0,
\end{aligned}
$$

where

$$u_2^*=1-\frac{r_2}{\mu_2}-\frac{A_2}{\mu_2}.$$

Thus, we can apply the Routh-Hurwitz criterion to the following quadratic equations:

$$\begin{aligned}&\lambda^2 + \lambda(1+\mu_2) + \mu_2 - A_2' u_2^* r_2 = 0, \text{ and}\\&\lambda^2 + \lambda(2(A_1+r_1) + E_1 + \gamma_1 + \mu_1(\alpha u_2^* - 1) + F_1)\\&+ (A_1 + E_1 + \gamma_1 + r_1 + \mu_1(\alpha u_2^* - 1))(F_1 + A_1 + r_1) - F_1(\gamma_1 + E) = 0.\end{aligned}$$

P_2 is locally asymptotically stable whenever all the following conditions hold:

$$\mu_2 - A_2' u_2^* r_2 > 0, \quad (4.63)$$

$$2(A_1+r_1) + E_1 + \gamma_1 + \mu_1(\alpha u_2^* - 1) + F_1 > 0, \quad (4.64)$$

$$(A_1 + E_1 + \gamma_1 + r_1 + \mu_1(\alpha u_2 - 1))(F_1 + A_1 + r_1) - F_1(\gamma_1 + E) > 0. \quad (4.65)$$

From (4.63), while applying the existence condition (4.35) for equilibrium point P_2, we have

$$\begin{aligned}\mu_2 - A_2' u_2^* r_2 &= \mu_2 - A_2' r_2 (1 - \frac{r_2}{\mu_2} - \frac{A_2}{\mu_2})\\&> r_2 - A_2' r_2 (1 - \frac{r_2}{\mu_2} - \frac{A_2}{\mu_2})\\&= r_2\big(1 - A_2'(1 - \frac{r_2}{\mu_2} - \frac{A_2}{\mu_2})\big),\end{aligned}$$

which is positive whenever

$$1 - A_2'(1 - \frac{r_2}{\mu_2} - \frac{A_2}{\mu_2}) > 0.$$

Equivalently (while combining with (4.35)), we have

$$0 < A_2'(1 - \frac{A_2}{\mu_2} - \frac{r_2}{\mu_2}) < 1. \quad (4.66)$$

For (4.64) to hold while applying (4.35), it is sufficient to have the following,

$$2(A_1+r_1) + E_1 + \gamma_1 + F_1 > \mu_1. \quad (4.67)$$

Also for (4.65) to hold while applying (4.35), it is sufficient to have the following,

$$\begin{aligned}(A_1+r_1-\mu_1)(F_1+A_1+r_1)&+(A_1+r_1)(\gamma_1+E_1)\\ &=\Big(1-\frac{\mu_1}{A_1+r_1}\Big)\Big(\frac{F_1}{A_1+r_1}+1\Big)+\gamma_1+E_1.\end{aligned}$$

Since

$$\Big(\frac{F_1}{A_1+r_1}+1\Big)\gg\gamma_1+E_1,$$

for (4.65) to hold, it is sufficient that

$$1-\frac{\mu_1}{A_1+r_1}\geq 0,$$

or equivalently,

$$A_1+r_1\geq\mu_1. \tag{4.68}$$

Thus, we have the following theorem to summarize the above result:

Theorem 10. *P_2 is asymptotically stable provided that (4.66) and (4.68) hold.*

Remark 3. *Condition (4.66) implies that the rate of bystander signal-induced normal tissue death at equilibrium must be bounded in order for the normal tissue to still persist.*

Remark 4. *Condition (4.68) implies that the cumulative effect of radiation-induced death on the tumor cells should exceed that tumor proliferation before the tumor cell can completely go extinct and normal tissue takes up the entire space.*

Stability of P_3

The Jacobian matrix corresponding to this equilibrium point is

$$J(P_3)=\begin{pmatrix} b_{11} & -\mu_1m_1v_3^*+F_1 & -\mu_1\alpha m_1v_3^* & -((A_1'+E_1')m_1-F_1')v_3^*\\ \gamma_1+E_1 & -(F_1+A_1+r_1) & 0 & -v_3^*(F_1'+A_1'-E_1'm_1)\\ -\mu_2\beta u_2^{**} & -\mu_2\beta u_2^{**} & b_{33} & -A_2'u_2^{**}\\ r_1 & r_1+\kappa_1 & r_2 & -1\end{pmatrix},$$

where

$$\begin{aligned}
b_{11} &= \mu_1(1-2m_1v_3^*-v_3^*-\alpha u_2^{**})-(A_1+E_1+\gamma_1+r_1) \\
&= -\frac{F_1}{m_1}-\alpha\mu_1-m_1\mu_1 v, \\
b_{33} &= \mu_2(1-2u_2^{**}-\beta m_1 v_3^*-\beta v_3^*)-(A_2+r_2) \\
&= -\mu_2+r_2+A_2.
\end{aligned}$$

The corresponding characteristic polynomial is given by

$$\lambda^4-\mathcal{B}_3\lambda^3-\mathcal{B}_2\lambda^2-\mathcal{B}_1\lambda-\mathcal{B}_0=0,$$

where

$$\mathcal{B}_3 = 1+B_1-b_{33}-b_{11}, \tag{4.69}$$

$$\begin{aligned}
\mathcal{B}_2 &= -b_{11}(B_1+1-b_{33})-B_1(b_{33}-1)+b_{33}-A_2'u_2^{**}r_2 \\
&\quad -B_2(r_1+\kappa_1)-B_5B_3-\mu_2\beta u_2^{**}B_6-B_4r_1,
\end{aligned} \tag{4.70}$$

$$\begin{aligned}
\mathcal{B}_1 &= b_{11}[B_1(b_{33}-1)+b_{33}-A_2'u_2^{**}r_2-B_2(r_1+\kappa_1)]-B_1b_{33}-A_2'u_2^{**}r_2B_1 \\
&\quad -B_2[\mu_2\beta r_2u_2^{**}-b_{33}(r_1+\kappa_1)]-B_5B_3(1-b_{33})+B_2B_3r_1 \\
&\quad -B_6[\mu_2\beta u_2^{**}B_5+B_1\mu_2\beta u_2^{**}+\mu_2\beta u_2^{**}+A_2'u_2^{**}r_1] \\
&\quad -B_4[B_5(r_1+\kappa_1)+B_1r_1-\mu_2\beta r_2u_2^{**}-r_1b_{33}],
\end{aligned} \tag{4.71}$$

$$\begin{aligned}
\mathcal{B}_0 &= b_{11}[B_1b_{33}+A_2'u_2^{**}r_2B_1+B_1(\mu_2\beta r_2u_2^{**}-b_{33}(r_1+\kappa_1))] \\
&\quad -B_3[-b_{33}B_5+B_2(\mu_2\beta u_2^{**}r_2+r_1b_{33})]-B_5B_6[\mu_2\beta u_2^{**}+A_2'u_2^{**}(r_1+\kappa_1)] \\
&\quad -B_1B_6[\mu_2\beta u_2^{**}+A_2'u_2^{**}r_1]-B_2B_6\mu_2\beta u_2^{**}\kappa_1 \\
&\quad -B_4B_5[-\mu_2\beta u_2^{**}r_2-b_{33}(r_1+\kappa_1)]-B_1B_4[-\mu_2\beta r_2u_2^{**}-r_1b_{33}],
\end{aligned} \tag{4.72}$$

where

$$\begin{aligned}
B_1 &= F_1+A_1+r_1, \quad B_2=v_3^*(F'+A_1'-E_1'm_1), \quad B_3=\mu_1u_1^{**}-F_1, \\
B_4 &= v_3^*[(A_1'+E_1')m_1-F_1'], \quad B_5=\gamma_1+E_1, \quad B_6=\mu_1\alpha u_1^{**}.
\end{aligned}$$

By the Routh-Hurwitz criterion for $n=4$, P_3 is locally asymptotically

Figure 4.1: Initial densities for the non-dimensional tumor cell (black), damaged tumor cell (red), and normal cell (blue), for all numerical simulations of system (4.20)-(4.23). This assumes no prior exposure to radiation, which is why the initial density for damaged tumor cell and the concentration of bystander signals are zero.

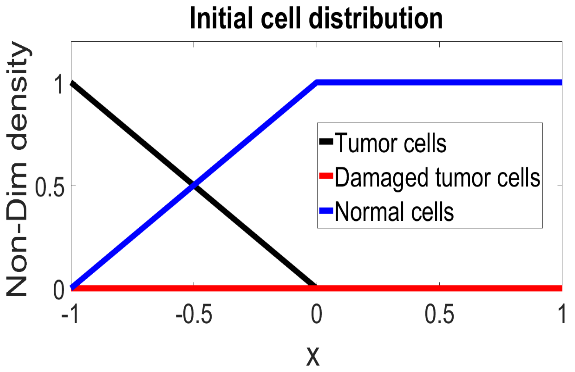

stable provided

$$\mathcal{B}_3, \mathcal{B}_1, \mathcal{B}_0 > 0, \quad (\mathcal{B}_3\mathcal{B}_2\mathcal{B}_1 - \mathcal{B}_1^2) > \mathcal{B}_3^2\mathcal{B}_0.$$

Clearly, $\mathcal{B}_3 > 0$. Hence, P_3 is locally asymptotically stable provided that

$$\mathcal{B}_1, \mathcal{B}_0 > 0, \quad (\mathcal{B}_3\mathcal{B}_2\mathcal{B}_1 - \mathcal{B}_1^2) > \mathcal{B}_3^2\mathcal{B}_0,$$

where $\mathcal{B}_i$ is given in (4.69)-(4.72) for each i.

4.4 Numerical exploration of the model

Our initial condition (Fig. 4.1) imposes a tumor-only state at $x = -1$ and a healthy-only state at $x = 1$. We assume that there is no prior radiation exposure, and thus no damaged tumor cells and bystander signals are initial present. This particular initial cell distribution is chosen simply for clear delineation of tumor vs. healthy cells, with the interface positioned at the domain midpoint ($x = -0.5$) to allow enough space in the domain to observe either leftward- or rightward-propagating waves. Changing the initial condition (not shown) does not alter the overall system behaviour, provided the biologically motivated boundary constraints (one end of the domain is primarily tumor, the other end is exclusively normal tissue with a mixed interface) are satisfied. We will restrict the spatial domain to one-dimension.

We impose the healthy steady state (P_2) at the boundary ahead of the the tumor wavefront and one of the two invaded states, P_1 or P_3 far behind, such that the traveling wave boundary conditions are:

$$(u_1, v, u_2, w)(\infty) \quad = \quad (0, 0, u_2^*, w_2^*), \text{ if } r_2 + A_2(w_2^*) < \mu_2,$$

and

$$(u_1, v, u_2, w)(-\infty) \quad = \quad \begin{cases} (u_1^*, v_1^*, 0, w_1^*), & \text{if } (4.31),\ (4.60) - (4.62) \text{ holds, or} \\ P_3, & \text{when } P_3 \text{ is stable.} \end{cases}$$

where

$$\begin{aligned} u_1^* &= \frac{A_1(w_1^*) + F_1(w_1^*) + r_1}{A_1(w_1^*) + E_1(w_1^*) + \gamma_1 + r_1 + F_1(w_1^*)} - \frac{A_1(w_1^*) + r_1}{\mu_1}, \\ v_1^* &= (\gamma_1 + E_1(w_1^*))\Big[\frac{1}{A_1(w_1^*) + E_1(w_1^*) + \gamma_1 + r_1 + F_1(w_1^*)} - \frac{A_1 + r_1}{\mu_1(A_1 + F_1 + r_1)}\Big], \\ u_2^* &= 1 - \frac{r_2}{\mu_2} - \frac{A_2(w_2^*)}{\mu_2}, \end{aligned}$$

w_1^* solves

$$w \quad = \quad (r_1 + \kappa_1)v_1^*(w) + r_1 u_1^*(w),$$

and w_2^* solves

$$w = r_2\Big(1 - \frac{r_2}{\mu_2} - \frac{A_2(w)}{\mu_2}\Big).$$

We solve (4.20)-(4.23) numerically in Matlab using the parameter values in Table 4.2. We discretize the system of partial differential equations using a spatial step of $dx = 0.15$ and temporal steps of $dt = 0.01$. The wavespeed of an invasive tumour (propagation in the positive x-direction) is measured by tracking the midpoint of the front as it evolves near the end of each simulation.

Consider a subsystem of (4.20) - (4.23), where the bystander signal concentration w is constant, and $A_i(w) = E_1(w) = 0$ and $F_1(w) = F_{10}$ given by

$$\begin{aligned} u_{1_t} &= Du_{1_{xx}} + \mu_1 u_1(1-u_1-v-\alpha u_2) - (\gamma_1+r_1)u_1 + F_{10}v, && (4.73)\\ v_t &= \gamma_1 u_1 - (F_{10}+r_1)v, && (4.74)\\ u_{2_t} &= \mu_2 u_2(1-u_2-\beta_1 u_1-\beta_2 v) - r_2 u_2. && (4.75)\end{aligned}$$

The effect of the bystander signals on the invasion speed of tumor waves is investigated by comparing traveling wave solutions (Figures 4.2a & 4.2b) for the subsystem (4.73) - (4.75) and the traveling wave solutions (Figures 4.2c & 4.2d) for the full system (4.20) - (4.23) for periods of 100 and 200 days of constant radiation exposures, respectively. In comparison, these numerical solutions confirm that bystander effects can indeed increase the invasion speed of tumor cells into surrounding normal cells.

In the next section, we will asymptotically investigate the dependence of the tumor wavespeed on bystander effects.

4.5 Traveling wave analysis of the model

In this section, we will use the method of matched asymptotic analysis to investigate the effect of bystander signals on the cancer invasion. In particular, we will compute the asymptotic wave speed of system (4.20) - (4.23) with constant radiation terms $r_{1,2}$, and $\boldsymbol{\gamma}$. To this end, let $z = x - ct$ be our traveling wave coordinate with c denoting the constant, positive wave speed. We transform (4.20)-(4.23) into traveling wave coordinates by letting $u_1(x,t) = u_1(z)$, $v(x,t) = v(z)$, $u_2(x,t) = u_2(z)$, and $w(x,t) = w(z)$. If we denote differentiation with respect to z by ', then we have

$$\begin{aligned} -cu_1' &= Du_1'' + \mu_1 u_1(1-u_1-v-\alpha u_2)\\ &\quad -(A_1(w)+E_1(w)+\gamma_1+r_1)u_1 + F_1(w)v, && (4.76)\\ -cv' &= (\gamma_1+E_1(w))u_1 - (A_1(w)+F_1(w)+r_1)v, && (4.77)\\ -cu_2' &= \mu_2 u_2(1-u_2-\beta_1 u_1-\beta_2 v) - (A_2(w)+r_2)u_2, && (4.78)\\ -cw' &= w'' + (\kappa_1+r_1)v + r_1 u_1 + r_2 u_2 - w. && (4.79)\end{aligned}$$

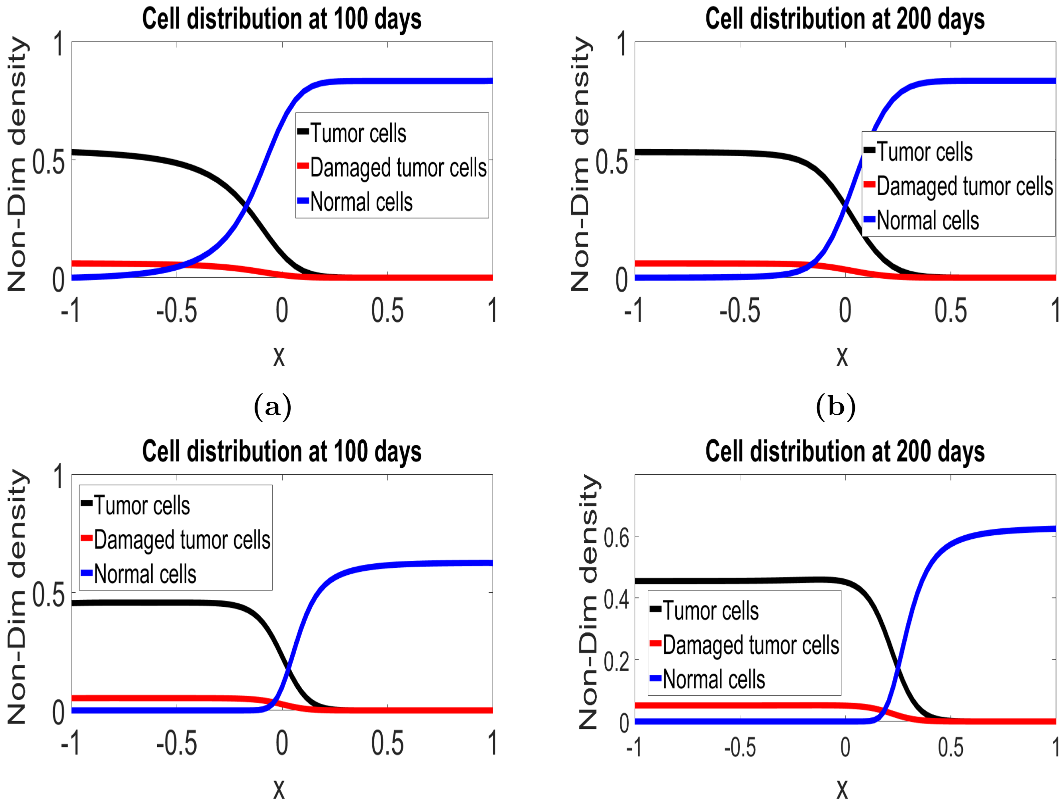

(a) **(b)**

(c) **(d)**

Figure 4.2: Cell distributions for the non-dimensional tumor density (black), damaged tumor density (red), and healthy tissue density (blue) at 100 and 200 days, respectively. The first row is the traveling wave solution for the system of PDE (4.20) - (4.23) when the bystander signal, w is assumed constant, and bystander effects are set to zero. The second row consists of the traveling wave solutions to the system (4.20) - (4.23) with bystander effects. The parameter values are the same as the dimensionless values outlined in Table 4.2.

The boundary condition is similar to the one used for the numerical simulation in Section 4.4. Since $D_1 \ll D_w$ in (4.76), the parameter D, which is the ratio between the free-space tumor diffusion coefficient D_1 and bystander signal diffusion coefficient D_w, is very small. We exploit it as a small parameter in the upcoming asymptotic analysis. So we relate D to the wave speed via consideration of the fast and slow dynamics of (4.76)-(4.79) related to a small parameter ϵ. In other words, if we let $z = x - \epsilon\theta t$, where $\epsilon = \sqrt{D} \ll 1$ and

$\theta = O(1)$, then the system becomes:

$$\begin{aligned} -\epsilon\theta u_1' &= \epsilon^2 u_1'' + \mu_1 u_1(1 - u_1 - v - \alpha u_2) \\ &\quad -(A_1 + E_1 + \gamma_1 + r_1)u_1 + F_1 v, && (4.80) \\ -\epsilon\theta v' &= (\gamma_1 + E_1)u_1 - (A_1 + F_1 + r_1)v, && (4.81) \\ -\epsilon\theta u_2' &= \mu_2 u_2(1 - u_2 - \beta_1 u_1 - \beta_2 v) - (A_2 + r_2)u_2, && (4.82) \\ -\epsilon\theta w' &= w'' + (\kappa_1 + r_1)v + r_1 u_1 + r_2 u_2 - w. && (4.83) \end{aligned}$$

In the following subsection, we will briefly introduce an important integral that will be very useful in the matched asymptotic analysis of the subsequent subsections. In Subsections 4.5.2 and 4.5.3, we will solve the ordinary differential equations (4.77) and (4.78) for an approximate solution to v and u_2, respectively. In Subsection 4.5.5, we will apply the method of matched asymptotic analysis to solve the reaction-diffusion equation for w. These approximate solutions will be combined to compute the asymptotic wavespeed in Subsection 4.5.6.

4.5.1 Laplace integral and Laplace method

Before we explore the asymptotic approximations for each model compartment, we will define an important integral that will be useful in the asymptotic analyses. The brief summary presented in this subsection is adapted from both Murray [85] and Bender and Orszag [6].

Definition 5 (Laplace Integral)**.** *A Laplace integral has the form*

$$I(x) := \int_{s_1}^{s_2} f(s) e^{x\phi(s)} ds, \qquad (4.84)$$

where x, which is very large (approaching infinity), is real and positive, $f(s)$ is a real continuous function, and $\phi(s)$, $\phi'(s)$, and $\phi''(s)$ are real and continuous in $s_1 \leq s \leq s_2$, where s_1 and s_2 are real.

A special case of the Laplace integral in (4.84) that occurs when $\phi(s) = -s$,

$s_1 = 0$, and $s_2 = \infty$ is given as

$$I(x) := \int_0^\infty f(s)e^{-xs}ds. \tag{4.85}$$

A classical result that is fundamental in determining the behavior of Laplace integral in (4.85), which can be extended to those of the form in (4.84) as well, is the Watson's Lemma, which we will state without proof in the following:

Theorem 11 (Watson's Lemma). *If* $f(s) \sim s^\alpha \sum_{n=0}^\infty a_n s^{\beta_n}$ *as* $s \to 0^+$, *where* $\alpha > -1$ *and* $\beta > 0$, *then*

$$\int_0^\infty e^{-xs} f(s)ds \sim \sum_{n=0}^\infty \frac{a_n \Gamma(\alpha + \beta_n + 1)}{x^{\alpha+\beta_n+1}} \quad (x \to \infty),$$

provided the integral converges for all sufficiently large x.

Watson's Lemma relies on the fact that the major contribution to the integral and hence to its leading order asymptotic approximation as $x \to \infty$ will come from the neighbourhood of zero, where $\phi(s) = -s$ assumes its maximum. In general, the behavior of Laplace integral of the form (4.84) is asymptotically determined by the contribution from the point in $s_1 \leq s \leq s_2$ where $\phi(s)$ has its maximum value. If there are several maxima, then the asymptotic approximation may have contributions from each of them. For example, if $\phi'(s) < 0$ in $s_1 \leq s \leq s_2$, then $\phi(s_1)$ is the maximum of $\phi(s)$. The integral can therefore be solved asymptotically by 'Taylor expanding' both $f(s)$ and $\phi(s)$ about s_1. We will apply this technique in the asymptotic approximations of the damaged tumor cells v and normal cells u_2 in the next two subsections.

4.5.2 Asymptotic approximation for the $v-$profile

For simplicity, let $G_1(z) = (\gamma_1 + E_1(w(z)))u_1(z)$ and $G_2(z) = A_1(w(z)) + F_1(w(z)) + r_1$. Thus, (4.81) simplifies to

$$\dot{v} - \frac{1}{\epsilon\theta} G_2(z)v = -\frac{1}{\epsilon\theta} G_1(z). \tag{4.86}$$

Using the elementary integrating factor method, the solution to the previous equation becomes

$$v(z) \quad = \quad \frac{1}{\epsilon\theta} e^{\frac{1}{\epsilon\theta}\int_0^z G_2(\xi)d\xi} \int_z^{\infty} G_1(s) e^{-\frac{1}{\epsilon\theta}\int_0^s G_2(\xi)d\xi} ds. \qquad (4.87)$$

Letting

$$\phi(s) = -\frac{1}{\theta}\int_0^s G_2(\xi)d\xi \quad \text{and} \quad I(z) = \int_z^{\infty} G_1(s) e^{\frac{1}{\epsilon}\phi(s)} ds,$$

(4.87) becomes

$$v(z) \quad = \quad \frac{I(z)}{\epsilon\theta} e^{\frac{1}{\epsilon\theta}\int_0^z G_2(\xi)d\xi},$$

where $I(z)$ is a Laplace integral [6, 85] of the form (4.84). Since $\phi(s) < -\frac{r_1 s}{\theta}$, then $e^{\frac{1}{\epsilon}\phi(s)}$ decays faster than $e^{\frac{r_1 s}{\epsilon\theta}}$. Since $G_2(z) > 0$ for all z in the interval $[z, \infty)$, then

$$\dot{\phi}(s) = -\frac{1}{\theta} G_2(s) < 0, \text{ for all } s \text{ in } [z, \infty).$$

This implies that on the interval $[z, \infty)$, $\frac{1}{\epsilon}\phi(s)$ has its maximum at $s = z$, and thus, Taylor expanding $I(z)$ about this point, yields:

$$\begin{aligned} I(z) \quad &\sim \quad \int_z^{\infty} G_1(z) e^{\frac{1}{\epsilon}(\phi(z) + (s-z)\dot{\phi}(z))} ds \qquad (4.88) \\ &= \quad G_1(z) e^{\frac{1}{\epsilon}(\phi(z) - z\dot{\phi}(z))} \int_z^{\infty} e^{\frac{1}{\epsilon} s \dot{\phi}(z)} ds \\ &= \quad -\frac{\epsilon}{\dot{\phi}(z)} G_1(z) e^{\frac{1}{\epsilon}\phi(z)}. \end{aligned}$$

The last equality uses the fact that

$$\lim_{z \to \infty} e^{\frac{z}{\epsilon}\dot{\phi}(z)} = 0.$$

Note that in (4.88), we have used

$$\begin{aligned} G_1(s) &= G_1(z) + \mathcal{O}(z) \\ \phi(s) &= \phi(z) + (s-z)\dot{\phi}(z) + \mathcal{O}(z^2). \end{aligned}$$

Thus,

$$\begin{aligned} v(z) &\sim \frac{1}{\epsilon\theta}\Big(- \frac{\epsilon}{\dot{\phi(z)}} G_1(z) e^{\frac{1}{\epsilon}\phi(z)} \Big) e^{-\frac{1}{\epsilon}\phi(z)} \\ &= \frac{G_1(z)}{G_2(z)} := \frac{\gamma_1 + E_1(w(z))}{A_1(w(z)) + F_1(w(z)) + r_1} u_1(z), \end{aligned} \tag{4.89}$$

where the last expression is valid since ϵ is very small parameter.

We notice that the asymptotic approximation to v is the steady-state solution to Eq. (4.21). In Fig. 4.3, we show both the asymptotic approximation and the numerical solution for damaged tumor cells and observe good agreement.

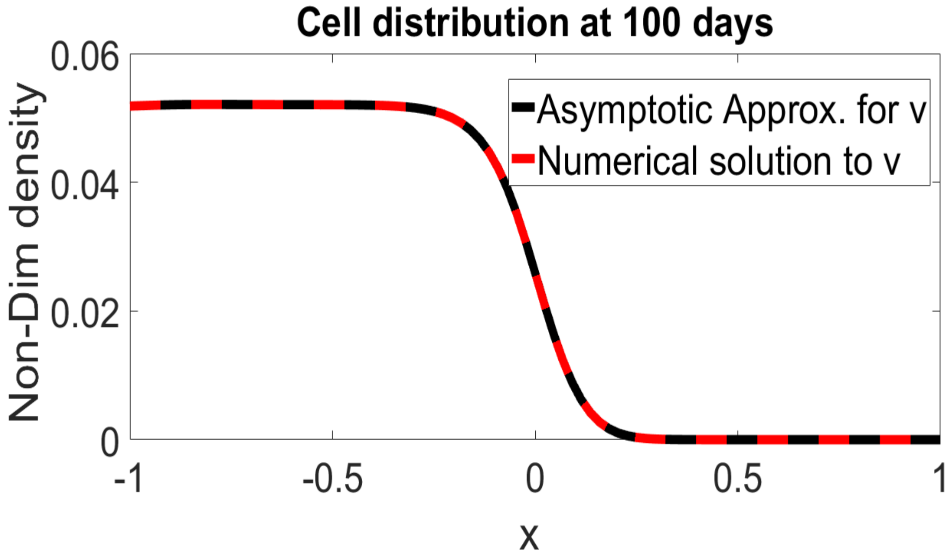

Figure 4.3: Traveling wave solutions to the $v-$ differential equation. We see good agreement between the asymptotic approximation (black) and the numerical solution (red) to the $v-$ equation (4.86)

4.5.3 Asymptotic approximation for the u_2-profile

From (4.82), we have

$$\begin{aligned} u_2' &= \frac{\mu_2}{\epsilon\theta}u_2^2 - \frac{\mu_2}{\epsilon\theta}u_2\big(1-\beta_1 u_1 - \beta_2 v - \frac{A_2}{\mu_2} - \frac{r_2}{\mu_2}\big) \\ &= \frac{\mu_2}{\epsilon\theta}(u_2^2 - B(z)u_2), \end{aligned} \tag{4.90}$$

where

$$B(z) = 1-\beta_1 u_1 - \beta_2 v - \frac{A_2}{\mu_2} - \frac{r_2}{\mu_2}.$$

With the substitution of $u_2 = \frac{1}{u_3}$ in (4.90), we have

$$u_3' - \frac{\mu_2}{\epsilon\theta}B(z)u_3 = -\frac{\mu_2}{\epsilon\theta},$$

which can be solved to get

$$u_3(z) = u_3(\bar{z})e^{-\frac{\mu_2}{\epsilon\theta}\int_z^{\bar{z}} B(s)ds} + \frac{\mu_2}{\epsilon\theta}e^{\frac{\mu_2}{\epsilon\theta}\int_0^z B(s)ds}\int_z^{\bar{z}} e^{-\frac{\mu_2}{\epsilon\theta}\int_0^\xi B(s)ds}d\xi,$$

where $\bar{z}$ is chosen to be very large so that

$$u_3(\bar{z}) = \frac{1}{u_2(\bar{z})} \approx \frac{1}{1-\frac{r_2}{\mu_2}-\frac{A_2(w_r)}{\mu_2}} = \frac{\mu_2}{\mu_2 - r_2 - A_2(w_r)}$$

with $w_r = w(+\infty)$. Substituting $u_2(z)$ back into the equation, we have

$$u_2(z) \approx \frac{\big(1-\frac{r_2}{\mu_2}-\frac{A_2(w_r)}{\mu_2}\big)e^{\frac{\mu_2}{\epsilon\theta}\int_z^{\bar{z}} B(s)ds}}{1+\frac{1}{\epsilon\theta}\big(\mu_2 - r_2 - A_2(w_r)\big)e^{\frac{\mu_2}{\epsilon\theta}\int_0^{\bar{z}} B(s)ds}\int_z^{\bar{z}} e^{-\frac{\mu_2}{\epsilon\theta}\int_0^\xi B(s)ds}d\xi}.$$

Suppose we denote

$$\begin{aligned} \phi_1(\xi) &= -\frac{\mu_2}{\theta}\int_0^\xi B(s)ds, \text{ and} \\ I_1(z) &= \int_z^{\bar{z}} e^{\frac{1}{\epsilon}\phi_1(\xi)}d\xi, \end{aligned}$$

then we have

$$u_2(z) \quad \approx \quad \frac{\left(1 - \frac{r_2}{\mu_2} - \frac{A_2(w_r)}{\mu_2}\right) e^{\frac{\mu_2}{\epsilon\theta}\int_z^{\bar{z}} B(s)ds}}{1 + \frac{I_1(z)}{\epsilon\theta}\left(\mu_2 - r_2 - A_2(w_r)\right) e^{\frac{\mu_2}{\epsilon\theta}\int_0^{\bar{z}} B(s)ds}}, \tag{4.91}$$

where $I_1(z)$ is a Laplace integral [6, 85]. To derive an asymptotic approximation to $I_1(z)$, we will consider different cases based on the zeros of $B(z)$.

Case 1: $B(z)$ has no root on the interval $[z, \bar{z}]$.

For fixed z, suppose that $B > 0$ on the interval $[z, \bar{z}]$, with $\bar{z} \gg 1$. Since we have that $\dot{\phi}_1(s) = -\frac{\mu_2}{\theta}B(s)$ for all $s \in [z, \bar{z}]$, this implies that $\frac{1}{\epsilon}\phi_1(s)$ has its maximum at $s = z$. Then we can Taylor expand the integrand of $I_1(z)$ about $s = z$, as follows:

$$\begin{aligned} I(z) \quad &\sim \quad \int_z^{\bar{z}} e^{\frac{1}{\epsilon}[\phi_1(z) + (\xi - z)\dot{\phi}_1(z)]} d\xi \\ &= \quad \int_z^{\infty} e^{\frac{1}{\epsilon}[\phi_1(z) + (\xi - z)\dot{\phi}_1(z)]} d\xi \\ &= \quad -\frac{\epsilon}{\dot{\phi}_1(z)} e^{\frac{1}{\epsilon}\phi_1(z)}. \end{aligned}$$

The last equality is based on the fact that

$$\lim_{z \to \infty} e^{\frac{z}{\epsilon}\dot{\phi}_1(z)} = 0.$$

Substituting this into (4.91), we obtain

$$\begin{aligned} u_2 \quad &\sim \quad \frac{\left(1 - \frac{r_2}{\mu_2} - \frac{A_2(w_r)}{\mu_2}\right) e^{\frac{\mu_2}{\epsilon\theta}\int_z^{\bar{z}} B(s)ds}}{1 + \frac{1}{\mu_2 B(z)}\left(\mu_2 - r_2 - A_2(w_r)\right) e^{\frac{\mu_2}{\epsilon\theta}\int_z^{\bar{z}} B(s)ds}} \\ &= \quad \frac{\left(1 - \frac{r_2}{\mu_2} - \frac{A_2(w_r)}{\mu_2}\right) e^{\frac{\mu_2}{\epsilon\theta}\int_z^{\bar{z}} B(s)ds}}{\frac{1}{B(z)}\left(1 - \frac{r_2}{\mu_2} - \frac{A_2(w_r)}{\mu_2}\right) e^{\frac{\mu_2}{\epsilon\theta}\int_z^{\bar{z}} B(s)ds}} \\ &= \quad B(z), \end{aligned}$$

where the second line follows from the first by observing that $B(s) > 0$ for all s in $[z, \bar{z}]$, $r_2 + A_2(w) < \mu_2$, $\epsilon \ll 1$, and hence the exponential dominates unity.

Case 2: $B(z)$ has at least one root on the interval $[z, \bar{z}]$.

Suppose that $s = z^*$ is the largest point in $[z, \bar{z}]$ for which $B(z^*) = 0$. For $z > z^*$, $B(z) > 0$ and the asymptotic analysis are analogous to the no-root case, where we found that $u_2(z) \approx B(z)$. It remains to consider the case $z < z^*$. At $z^* = z$, $\dot{\phi}_1(z^*) = -\frac{1}{\theta}B(z^*) = 0$, and it follows that $\ddot{\phi}_1(z^*) = -\frac{1}{\theta}\dot{B}(z^*) \leq 0$. Excluding the case for which $\ddot{\phi}_1(z^*) = 0$, we assume that $\ddot{\phi}_1(z^*) > 0$ and expand $I(z)$ about $s = z^*$:

$$\begin{aligned}
I_1(z) &\sim \int_z^{z^*} e^{\frac{1}{\epsilon}[\phi_1(z^*)+(\xi-z^*)\ddot{\phi}_1(z^*)]} d\xi \\
&= e^{\frac{1}{\epsilon}\phi_1(z^*)} \int_{\xi-z}^{0} e^{\frac{s^2}{\epsilon}\ddot{\phi}_1(z^*)} ds \quad \text{where } s = \xi - z^*, \\
&\sim e^{\frac{1}{\epsilon}\phi_1(z^*)} \int_{-\infty}^{\infty} e^{\frac{s^2}{\epsilon}\ddot{\phi}_1(z^*)} ds \;=\; 2e^{\frac{1}{\epsilon}\phi_1(z^*)} \int_0^{\infty} e^{\frac{s^2}{\epsilon}\ddot{\phi}_1(z^*)} ds \\
&= 2e^{\frac{1}{\epsilon}\phi_1(z^*)} \int_0^{\infty} e^{\frac{x}{\epsilon}} \frac{dx}{\ddot{\phi}_1(z^*)\sqrt{\frac{2x}{\ddot{\phi}_1(z^*)}}} \quad \text{where } x = \frac{1}{2}\ddot{\phi}_1(z^*)s^2; \\
&= \sqrt{\frac{2}{\ddot{\phi}_1(z^*)}} e^{\frac{1}{\epsilon}\phi_1(z^*)} \int_0^{\infty} e^{\frac{x}{\epsilon}} x^{-\frac{1}{2}} dx \;=\; \sqrt{\frac{2\pi\epsilon}{-\ddot{\phi}_1(z^*)}} e^{\frac{1}{\epsilon}\phi_1(z^*)}.
\end{aligned}$$

Substituting this into (4.90) gives us

$$\begin{aligned}
u_2(z) &\sim \frac{\left(1 - \frac{r_2}{\mu_2} - \frac{A_2(w_0)}{\mu_2}\right) e^{\frac{\mu_2}{\epsilon\theta}\int_z^{\bar{z}} B(s)ds}}{1 + \frac{1}{\epsilon\theta}\sqrt{\frac{2\pi\epsilon\theta}{\dot{B}(z^*)}} e^{\frac{1}{\epsilon}\phi_1(z^*)} \big(\mu_2 - r_2 - A_2(w_0)\big) e^{\frac{\mu_2}{\epsilon\theta}\int_0^{\bar{z}} B(s)ds}} \\
&= \frac{\left(1 - \frac{r_2}{\mu_2} - \frac{A_2(w_0)}{\mu_2}\right) e^{\frac{\mu_2}{\epsilon\theta}\int_z^{\bar{z}} B(s)ds}}{1 + \sqrt{\frac{2\pi}{\epsilon\theta\dot{B}(z^*)}} \big(\mu_2 - r_2 - A_2(w_0)\big) e^{\frac{\mu_2}{\epsilon\theta}\int_{z^*}^{\bar{z}} B(s)ds}} \\
&\approx \frac{\left(1 - \frac{r_2}{\mu_2} - \frac{A_2(w_0)}{\mu_2}\right) e^{\frac{\mu_2}{\epsilon\theta}\int_z^{\bar{z}} B(s)ds}}{\sqrt{\frac{2\pi}{\epsilon\theta\dot{B}(z^*)}} \big(\mu_2 - r_2 - A_2(w_0)\big) e^{\frac{\mu_2}{\epsilon\theta}\int_{z^*}^{\bar{z}} B(s)ds}} \\
&= \frac{e^{\frac{\mu_2}{\epsilon\theta}\int_z^{\bar{z}} B(s)ds}}{\mu_2\sqrt{\frac{2\pi}{\epsilon\theta\dot{B}(z^*)}} e^{\frac{\mu_2}{\epsilon\theta}\int_{z^*}^{\bar{z}} B(s)ds}} \\
&= \frac{1}{\mu_2}\sqrt{\frac{\epsilon\theta\dot{B}(z^*)}{2\pi}} e^{\frac{\mu_2}{\epsilon\theta}\int_z^{z^*} B(s)ds} \;\approx\; 0,
\end{aligned}$$

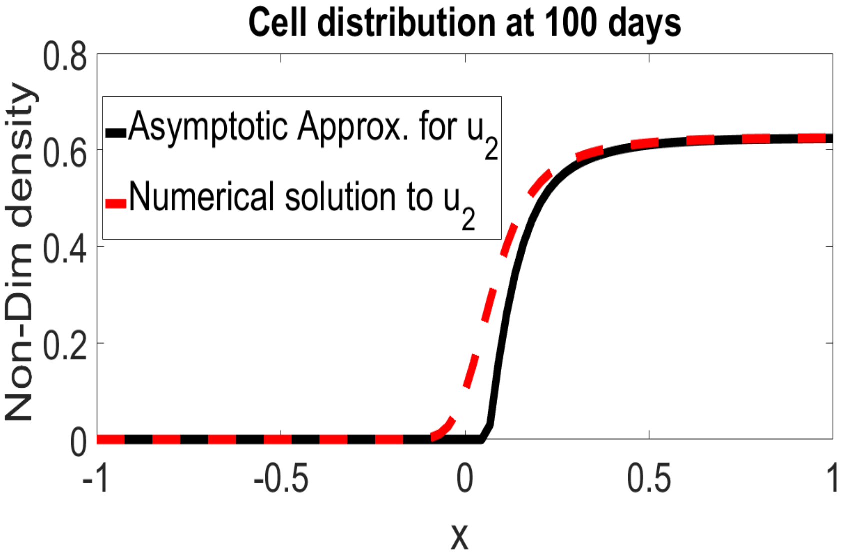

Figure 4.4: Traveling wave solutions to the u_2- differential equation. We see good agreement between the asymptotic approximation (Eq. (4.92) in black) and the numerical solution (Eq. (4.90 in red)).

where the third line follows from the domination of the exponential function over the unity and the last line follows from letting $\epsilon \to 0$ from an approximation to leading order in ϵ. This holds since $B(s) < 0$ in the interval $[z, z^*]$ and hence the exponential vanishes.

Thus, we found that

$$u_2 \sim \max\{B(z), 0\} \tag{4.92}$$

to leading order of ϵ.

In Fig. 4.4, we show both the asymptotic approximation in Eq. (4.92) and the numerical solution for normal cells and observe good agreement.

4.5.4 Boundary layer - outer and inner solutions

It is clear from the numerical simulations that the system exhibits a boundary layer: within and near the tumor wavefront is a region of a rapid change for the species and their derivatives, while far behind and ahead of the wavefront the changes are much slower. To asymptotic (leading-order) accuracy, the solution in the slowly-varying outer regions satisfies (4.80)-(4.83) with $\epsilon = 0$:

$$\begin{aligned} 0 &= \mu_1 u_1(1 - u_1 - v - \alpha u_2) \\ &\quad -(A_1(w) + E_1(w) + \gamma_1 + r_1)u_1 + F_1(w)v, && (4.93) \\ 0 &= (\gamma_1 + E_1)u_1 - (A_1 + F_1 + r_1)v, && (4.94) \\ 0 &= \mu_2 u_2(1 - u_2 - \beta_1 u_1 - \beta_2 v) - (A_2 + r_2)u_2, && (4.95) \\ 0 &= w'' + (\kappa_1 + r_1)v + r_1 u_1 + r_2 u_2 - w. && (4.96) \end{aligned}$$

If we rescale the narrow wavefront region by setting $z = \epsilon\zeta$ and denote the leading-order solution in the wavefront region with subscript 'in', we have

$$\begin{aligned} -\theta u'_{1_{in}} &= u''_{1_{in}} + \mu_1 u_{1_{in}}(1 - u_{1_{in}} - v_{in} - \alpha u_{2_{in}}) && (4.97) \\ &\quad -(A_1(w) + E_1(w) + \gamma_1 + r_1)u_{1_{in}} + F_1(w)v_{in}, && (4.98) \\ -\theta v'_{in} &= (\gamma_1 + E_1)u_{1_{in}} - (A_1 + F_1 + r_1)v_{in}, && (4.99) \\ -\theta u'_{2_{in}} &= \mu_2 u_{2_{in}}(1 - u_{2_{in}} - \beta_1 u_{1_{in}} - \beta_2 v_{in}) - (A_2 + r_2)u_{2_{in}}, && (4.100) \\ w''_{in} &= 0. && (4.101) \end{aligned}$$

We will find an asymptotic approximation for the bystander signal profile (w) using the method of matched asymptotic analysis, which matches the solution for the outer region to the solution for the inner region. Finally, we will incorporate the asymptotic solutions for the inner region for v, u_2, and w into (4.98). By that, we can estimate the wavespeed of the system.

To this end, while incorporating the solution for v and u_2 in the two previous subsections, we will approximate the bystander signals profile, w.

4.5.5 Asymptotic approximation for the $w-$profile

Based on the boundary conditions behind and ahead of the tumor wave front, $u_1, v \approx 0$ ahead of the wavefront. Since $u_2 \sim \max\{B(z), 0\}$ on the domain, we see that in order for the normal tissue to satisfy the boundary conditions imposed ahead of the tumor waves, then $u_2 \sim B(z) = 1 - \frac{A_2(w_r)}{\mu_2} - \frac{r_2}{\mu_2}$, with $w_r = w(+\infty)$.

Using this information, ahead of the wavefront, the bystander signal waves governed by (4.96) is asymptotically given by

$$\begin{aligned} 0 &\sim w'' + r_2\big(1 - \frac{A_2(w_r)}{\mu_2} - \frac{r_2}{\mu_2}\big) - w \\ &= w'' - w + r_2\big(1 - \frac{r_2}{\mu_2} - \frac{A_2(w_r)}{\mu_2}\big), \end{aligned}$$

the solution of which is given by

$$\begin{aligned} w_+(z) &\sim r_2(1 - \frac{A_2(w_r)}{\mu_2} - \frac{r_2}{\mu_2}) + K_1 e^{-z} + K_2 e^{z} \\ &= r_2(1 - \frac{A_2(w_r)}{\mu_2} - \frac{r_2}{\mu_2}) + K_1 e^{-z}, \end{aligned}$$

where the last line follows from applying the boundary condition for w ahead of the wavefront. On the other hand, behind the wavefront, since $v \approx v(-\infty) = v_1^*$, and $u_1 \approx u(-\infty) = m_1(w_l)v_1^*$, (where m_1 and v_1^* are as in (4.29) and (4.30)), the $w-$profile can be approximated by

$$w'' - w + (\kappa_1 + r_1 + r_1 m_1(w_l))v_1^* \approx 0,$$

which can be solved to get

$$\begin{aligned} w_-(z) &\approx (\kappa_1 + r_1 + r_1 m_1(w_l))v_1^* + K_3 e^{z} + K_4 e^{-z} \\ &= (\kappa_1 + r_1 + r_1 m_1(w_l))v_1^* + K_3 e^{z}, \end{aligned}$$

where the last line follows from applying the boundary conditions for w behind the wavefront. From (4.101),

$$w_{in} = K_5 + K_6\xi.$$

Since w_{in} must be bounded at both ends, w_{in} must be a constant. Matching the outer solution to the inner boundary is equivalent to matching the functional forms of $w_-(0)$ and $w_+(0)$ with one another across the inner region, where both take the value of w_{in}. We match the functions, $w_-(0) = w_+(0)$, and their derivatives, $\dot{w}_-|_0 = \dot{w}_+|_0$, to obtain the leading order in ϵ: $w_-(0) = w_+(0)$ and

$\dot{w}_+(0) = \dot{w}_-(0)$ respectively imply that

$$\begin{aligned}(\kappa_1 + r_1 + r_1 m_1(w_l))v_1^* + K_3 &= r_2(1 - \frac{A_2(w_r)}{\mu_2} - \frac{r_2}{\mu_2}) + K_1, \quad \text{and} \\ -K_1 &= K_3,\end{aligned}$$

which in turn implies

$$\begin{aligned}K_1 &= \frac{1}{2}\Big[(\kappa_1 + r_1 + r_1 m_1(w_l))v_1^* - r_2\big(1 - \frac{A_2(w_r)}{\mu_2} - \frac{r_2}{\mu_2}\big)\Big], \\ K_3 &= -\frac{1}{2}\Big[(\kappa_1 + r_1 + r_1 m_1(w_l))v_1^* - r_2\big(1 - \frac{A_2(w_r)}{\mu_2} - \frac{r_2}{\mu_2}\big)\Big].\end{aligned}$$

Therefore,

$$w(z) \approx \begin{cases}(\kappa_1 + r_1 + r_1 m_1(w_l))v_1^*(1 - \frac{1}{2}e^z) + \frac{r_2}{2}\big(1 - \frac{A_2(w_r)}{\mu_2} - \frac{r_2}{\mu_2}\big)e^z, & z < 0 \\ r_2\big(1 - \frac{A_2(w_r)}{\mu_2} - \frac{r_2}{\mu_2}\big)(1 - \frac{1}{2}e^{-z}) + \frac{v_1^*}{2}(\kappa_1 + r_1 + r_1 m_1(w_l))e^{-z}, & z > 0,\end{cases} \tag{4.102}$$

and it follows that

$$w_{in} = \frac{1}{2}\Big[r_2\big(1 - \frac{A_2(w_r)}{\mu_2} - \frac{r_2}{\mu_2}\big) + (\kappa_1 + r_1 + r_1 m_1(w_l))v_1^*\Big] \tag{4.103}$$

since $w_+(0) = w_-(0) = w_{in}$, where

$$m_1 = \frac{F_1(w_l) + A_1(w_l) + r_1}{\gamma_1 + E_1(w_l)},$$

with $w_l = w(-\infty)$.

4.5.6 Determination of asymptotic wave speed, c

In order to compute the invasive speed c, of an invading tumor wave in our system, we first notice that the solution to the inner dynamics of the $v-$profile is given (as a consequence of 4.89) by

$$v_{in} \sim \frac{\gamma + E_1(w_{in})}{A_1(w_{in}) + F_1(w_{in}) + r_1} u_{1_{in}}(z). \tag{4.104}$$

Also, as a consequence of (4.92), the solution to the inner dynamics of u_2-profile is given by

$$u_{2_{in}} \sim 1 - \beta_1 u_{1_{in}} - \beta_2 v_{in} - \frac{A_2(w_{in})}{\mu_2} - \frac{r_2}{\mu_2}. \tag{4.105}$$

Thus, incorporating the solution to the inner dynamics of v, u_2, and w in (4.98), (4.104), (4.103), (4.105), respectively, we get an equation for $u_{1_{in}}$, namely

$$\begin{aligned} -\theta u'_{1_{in}} &= u''_{1_{in}} + u_{1_{in}} \Big[\mu_1 - \mu_1 u_{1_{in}} - \frac{\mu_1}{m_1(w_{in})} u_{1_{in}} - \mu_1 \alpha u_{2_{in}} \\ &\quad - A_1(w_{in}) - E_1(w_{in}) - \gamma_1 - r_1 + \frac{F_1(w_{in})}{m_1(w_{in})} \Big]. \end{aligned}$$

Thus, if we denote

$$\beta_0 = \mu_1 + \frac{F_1(w_{in})}{m_1(w_{in})} + \mu_1 \alpha \big(\frac{A_2(w_{in})}{\mu_2} - 1 + \frac{r_2}{\mu_2} \big) - \big(A_1(w_{in}) + E_1(w_{in}) + \gamma_1 + r_1 \big),$$

$$\beta_{00} = \mu_1 \Big(1 + \frac{1 - \alpha\beta_2}{m_1(w_{in})} - \alpha \beta_1 \Big),$$

then the equation simplifies to a Fisher-KPP-type equation:

$$-\theta u'_{1_{in}} \sim u''_{1_{in}} + u_{1_{in}} (\beta_0 - \beta_{00} u_{1_{in}}).$$

which exhibits an asymptotic front speed of $\theta \sim 2\sqrt{\beta_0}$. Substituting back to the original parameters and recalling that $c \sim \epsilon\theta = \sqrt{D}\theta$, the wavespeed is then given by

$$c \ \sim \ 2\sqrt{D\mu_1\Big[1+\alpha\Big(\frac{A_2(w_{in})+r_2}{\mu_2}-1\Big)-\Big(\frac{A_1(w_{in})+r_1}{\mu_1}\Big)\Big(1+\frac{1}{m_1(w_{in})}\Big)\Big]}, \tag{4.106}$$

where w_{in} is given by (4.103).

A close look at the wavespeed (4.106) reveals its dependence on the bystander signals in both the tumor and the normal cells. While the bystander effect $A_2(w)$ on the normal cells enhances the tumor invasion speed, the bystander effect $A_1(w)$ on the tumor cells decreases the invasion speed. Similarly, while the radiation-induced normal cell death (with rate r_2) enhances the invasion speed, radiation-induced tumor cell death (with rate r_1) reduces the speed. We also notice that highly proliferative normal cells (with large μ_2) will decrease the speed and highly proliferative (with large μ_1) tumor cells will be more invasive.

Comparing our analytical solutions, (4.89), (4.92), (4.102), and (4.103), with estimates measured from our numerical solutions, we see an agreement (figure not shown). There are discrepancies on the order of our asymptotic parameter ϵ, resulting from the use of leading-order approximations in the asymptotics. This discrepancies might decrease if we include higher-order terms.

If we set $A_i(w_{in}) = E_1(w_{in}) = 0$ and $F_1(w_{in}) = F_{10}$ in (4.106), we derive the wavespeed c_0 for the system without bystander effects as

$$c_0 \ \sim \ 2\sqrt{D\mu_1\Big[1+\alpha\Big(\frac{r_2}{\mu_2}-1\Big)-\frac{r_1}{\mu_1}\Big(1+\frac{\gamma_1}{F_{10}+r_1}\Big)\Big]}, \tag{4.107}$$

which is the invasion speed of the subsystem (4.73)-(4.75). This clearly reveals that a tumor that possesses a high rate F_{10} of damage repair will be more invasive.

In order to confirm the bystander signal-induced invasion observed in the numerical solutions in Fig. 4.2, we also compare the asymptotic wavespeeds with and without bystander effects as shown in Fig. 4.5. We observe that

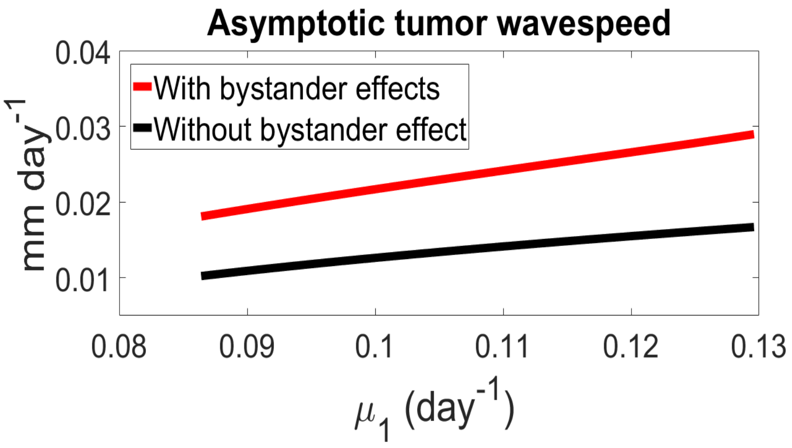

Figure 4.5: Asymptotic tumor wavespeed over increasing proliferation rate of tumor cell population, μ_1. The wavespeed with bystander effects is computed from Eq. (4.106) and wavespeed without bystander effects is computed from (4.107). We kept $\beta_{1,2} = 2$, $\alpha = 0.5$, $A_{10} = 0.5$, $F_{10} = 0.7$, and other parameters are held constant according to Table 4.2.

the wavespeed with bystander effects always predominates the speed without bystander effects, thus confirming the signal-mediated cancer invasion.

4.6 Discussion

We have developed a continuum framework to investigate the bystander signal-mediated tumor invasion observed in many biological experiments. This modeling framework is a generalization of the model for bystander signal developed in Chapter 2. By modeling continuous exposure of a tumor and its surrounding normal tissue to constant low doses of radiation, we were able to confirm (both numerically and analytically) that bystander signal can expedite tumor invasion. The analyses of this chapter are still restricted only to the invasion of a homogeneous tumor mass into a homogeneous normal cell population with a mixed interface. However, since tumors can be interwoven with other normal cells, a next step is to consider the invasion of a heterogenous mixture of both tumor and normal cells into a homogeneous normal cell population. This case is also suggested by the steady-state analysis of our model. Nevertheless, it is promising that the current analyses obtained such invasive behavior, in part because they provide good target for model validation. In this respect, our model fits into a larger goal of assessing possible experiments that will test the bystander signal-mediated invasion hypothesis - an important task toward developing novel cancer treatment strategies.

Furthermore, Section 4.5 demonstrates that our model remains amenable to mathematical analysis. Through matched asymptotic traveling wave analysis, we have been able to characterize the homogeneous invasive behavior in parameter space. The asymptotic wavespeeds are also well corresponded with the numerical simulations (figure not shown). We also compared the asymptotic approximation to the wavespeed with and without bystander effects. We showed that the asymptotic wavespeed with bystander effects is always higher than the speed without bystander effects. This also confirms the earlier numerical solution.

While the model presented here captures experimental observations at the cellular scale, the bystander signal-mediated invasion might be a result of some biochemical or molecular mechanisms. These details would inform the choice of the functional forms of $A_i(w)$, $B(w)$, $E(w)$ and $F(w)$, which describe the bystander effects. Thus a finer-scale understanding of the bystander signal interaction in the observed tumor invasion maybe necessary for more insight that is capable of informing better treatment strategies for aggressively invasive tumors.

Chapter 5

Effects of G2-checkpoint dynamics on low-dose hyper-radiosensitivity

The work presented in this chapter has been published as: Olobatuyi, Oluwole, Gerda de Vries, and Thomas Hillen. *Effects of G2 checkpoint dynamics on low-dose hyper-radiosensitivity.* Journal of mathematical biology, 2018, https://doi.org/10.1007/s00285-018-1236-8.

Abstract. *In experimental studies, it has been found that certain cell lines are more sensitive to low-dose radiation than would be expected from the classical Linear-Quadratic model (LQ model). In fact, it is frequently observed that cells incur more damage at low dose (say 0.3 Gy) than at higher dose (say 1 Gy). This effect has been termed hyper-radiosensitivity (HRS). The effect depends on the type of cells and on their phase in the cell cycle when radiation is applied. Experiments have shown that the G2-checkpoint plays an important role in the HRS effects. Here we design and analyze a differential equation model for the cell cycle that includes G2-checkpoint dynamics and radiation treatment. We fit the model to surviving fraction data for different cell lines including glioma cells, prostate cancer cells, as well as to cell populations that are enriched in certain phases of the cell cycle. The HRS effect is measured* *in the literature through* $\frac{\alpha_s}{\alpha}$*, the ratio of slope* $-\alpha_s$ *of the surviving fraction curve at zero dose to slope* $-\alpha$ *of the corresponding LQ model. We derive an explicit formula for this ratio and we show that it corresponds very closely to experimental observations. Finally, we identify the dependence of this ratio on the surviving fraction at 2 Gy. It was speculated in the literature that such dependence exists. Our theoretical analysis will help to more systematically identify the HRS in cell lines, and opens doors to analyze its use in cancer treatment.*

5.1 Introduction

The cell cycle is an ordered sequence of phases in the lifespan of a cell, which normally culminates in cell division. The cell cycle progression from one phase to the other is unidirectional. The four phases of the cell cycle are ordered as G1, S, G2, and M. The G1-phase is the first phase of a new daughter cell which lasts between 10-12h. This is the first growth phase where a cell increases its protein supply, increases the number of organelles like mitochondria and ribosomes, and increases in size. The S-phase, also referred to as the synthesis phase, starts when DNA replication commences. During this phase, which lasts about 5-7h, the amount of DNA in the cell effectively doubles. The G2-phase is the second growth phase lasting about 4h. This is the period of protein synthesis and rapid cell growth in preparation for cell division. The last phase is the M-phase, also referred to as the mitotic phase. This is the shortest cycle which last about 2h. During this stage, the cell divides into two daughter cells.

As a cell progresses through this cycle, the integrity of its genome is ensured and maintained by regulatory mechanisms called checkpoints [28]. These checkpoints, *seemingly* situated at the entrance to the next cycle phase, ensure that a cell does not progress into the next phase with unrepaired damage. Usually, when a cell sustains any form of damage in a particular phase, the checkpoint of that phase will stop the cell's progression into the next phase in order to allow more time for damage repair. The process that stops cycle progression in order to give more time for repair is referred to as cell cycle arrest [84]. As soon as the repair is complete, the cell is allowed to continue to the next phase.

The type of damage that is of particular interest in this chapter is radiation-induced damage and the corresponding response of various cell cycle checkpoints. Sometimes, the radiation damage is not recognized by the checkpoint, and damaged cells proceed to the next phase unrepaired. Damaged cells in the G2 phase that evade the G2 checkpoint have been shown to experience cell death shortly afterward. This cell death, which prevents mutation as a result of unrepaired damage, is called mitotic catastrophe [16]. Experiments have shown that checkpoint evasion predominantly occurs when cells are exposed to low doses of radiation (mostly below 0.5 Gy) [45]. Mitotic catastrophe of G2-phase cells that evade the checkpoint has been shown to result in increased cell death at low doses of radiation. This phenomenon is called hyper-radio-sensitivity (HRS). As the radiation dose increases and the corresponding damage is recognized by the checkpoint, there is cell cycle arrest of the damaged cells, which results in an apparent resistance to radiation. This low-dose resistance phenomenon is referred to as Increased Radio-Resistance (IRR). Experiments involving cells in different phases have also shown that the HRS/IRR phenomena are more exaggerated in G2-phase cells relative to cells in other phases [108, 67, 65, 54, 30].

The surviving fraction (SF) of cells is traditionally modelled by the Linear Quadratic (LQ) model given by

$$\mathrm{SF}_0(D) \;=\; e^{-\alpha D-\beta D^2}, \tag{5.1}$$

where D is the total radiation dose (measured in Gy), α is the rate at which single radiation tracks produce lethal lesions, and β is the rate at which binary misrepair of pairs of double strand breaks (DSB) from different radiation tracks lead to lethal lesions [12]. The LQ model is a monotonically decreasing function of dose; it cannot be used to describe the low-dose phenomena of HRS/IRR. In most cases, due to insufficient information about the low-dose cellular behaviors, the LQ model is extrapolated to low doses. However, experiments have shown that such extrapolation underestimates the low-dose

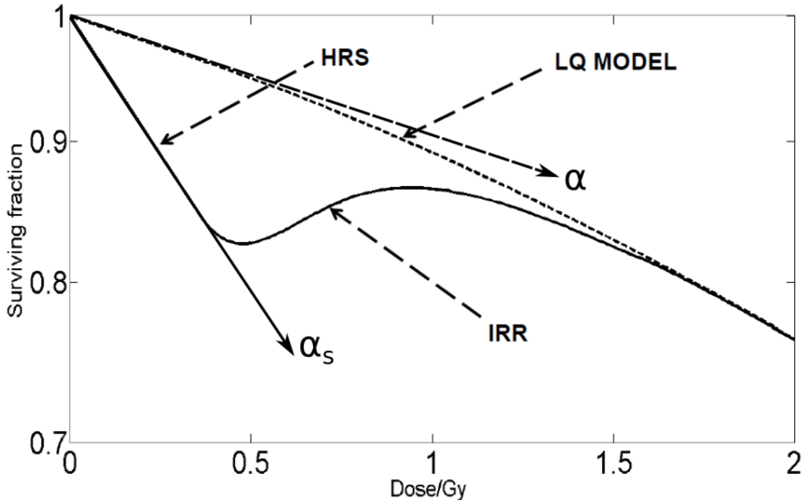

Figure 5.1: A surviving fraction curve illustrating the phenomena of HRS and IRR. The solid curve is the IR model while the dotted curve is the LQ model. $-\alpha_s$ denotes the initial slope of the IR model while $-\alpha$ denotes initial slope of the LQ model.

radiation effects [54, 30].

In order to account for the HRS/IRR phenomena, Marples et. al. in [66] developed a modification of the LQ model, called the Induced Repair (IR) model, given by

$$\mathrm{SF}_1(D) \;=\; \exp\Big\{-\alpha\Big(1+\Big(\frac{\alpha_s}{\alpha}-1\Big)e^{-\frac{D}{D_c}}\Big)D-\beta D^2\Big\}, \tag{5.2}$$

where α, β, and D are as defined in (5.1). D_c is the dose at which HRS transitions to the IRR phenomenon, and $-\alpha_s$ is the initial slope of the surviving fraction curve (5.2) at $d = 0$ Gy. Figure 5.1 clearly explains these terminologies. Since the IR model was developed, the HRS/IRR phenomena have been widely quantified by the α_s/α index [44, 108]. It is easy to see that if $\frac{\alpha_s}{\alpha} = 1$, then the IR model reduces to the LQ model. Furthermore, any cell with $\frac{\alpha_s}{\alpha} > 1$ will exhibit the HRS/IRR phenomena.

Experiments in [53, 54] have been conducted at the molecular level in order to identify what is responsible for the HRS/IRR phenomena. It has been shown in [71, 65, 70] that the HRS/IRR phenomena consist of a sequence of cellular events such as checkpoint activity, mitotic catastrophe, cellular repair mechanism; and also the proportion of G2-phase cells at the time of radiation exposure. However, the relationship between the $-\alpha_s$, the slope of the surviving fraction curve at $d = 0$ Gy, and these events remains unclear. In particular, how can we interpret or model the slope $-\alpha_s$ in terms of these events?

In this chapter, we focus on the HRS phenomenon by building an ordinary differential equations (ODE) model for the dynamics of cell cycle phases and damage repair, and how these are affected by radiation. We validate the model by fitting it to surviving fraction curves of ten asynchronous and three synchronous cell lines that exhibit the HRS phenomenon. Then we derive $-\alpha_s$, the initial slope of the surviving fraction (SF) curve, from this model for two cases motivated by the radiobiological experiments. In particular, we derive this initial slope of the SF curve when cell survival is computed immediately after radiation with (1) exposure time too short to accommodate cell progression and damage repair, and (2) exposure time long enough to accommodate damage repair but too short to accommodate cell cycle progression. Although in the experimental procedures leading to the measurement of the SF data, there is a post-radiation incubation period of 2 weeks after which survived cells can be recognized by their ability to form colonies (i.e., more than 50 daughter cells). This is because the current technology cannot detect survived cells until they are able to form colonies. However, since our deterministic model can compute the number of radiation-induced dead cells immediately after radiation exposure, we will assume that this model can be used as a proxy for measuring SF. Furthermore, experiments have shown that the repair of radiation damage usually occurs between 30-35mins after radiation [53]. Thus, since most SF data are measured from radiation exposure of at most 10 mins, we will use the derivation under the first assumption to compute the corresponding $-\alpha_s$ for our model. We find that the values of $-\alpha_s$ computed from our model agree with the data available in the literature. We also find the relationship between $-\alpha_s$ and some of the cellular events implicated in the HRS phenomenon. Finally, we find an explicit relationship between the $\frac{\alpha_s}{\alpha}$ index and the radioresistance at 2 Gy, which confirms speculations from the observations in [57].

All through this chapter, the term *synchronous* cell population will mean a culture of cells that is *rich* in a particular phase of the cell cycle. Thus, we will use this term interchangeably with the term cell culture *enriched* in a particular phase of the cell cycle. On the other hand, the term *asynchronous* cell population will refer to a cell culture that is not enriched in a particular phase of the cell cycle.

The rest of this chapter will be organized as follows: In Section 5.2, we formulate and develop the mathematical model from underlying cell cycle dynamics, and explain the relevant parameters. In Section 5.3, we fit the model to the surviving fraction data for 10 different asynchronous cell lines. We also fit the model to populations of cells enriched in various cell cycle phases. We estimate the model parameters and their 95% credible intervals for these cell lines. In Section 5.4, we derive the analytical formula for $-\alpha_s$ from the model under the two simplifying cases mentioned earlier. In Section 5.5, we numerically validate the derivations in the previous section. We find that the formula for the initial slope of SF curve derived in the previous section can replicate the values of $-\alpha_s$ in the literature. In Section 5.6, we derive the relationship between $\frac{\alpha_s}{\alpha}$ index and the radioresistance at 2 Gy. We find that cells with the same intrinsic radiosensitivity show an increasing relationship between $\frac{\alpha_s}{\alpha}$ and the radioresistance at 2 Gy. This result contextualizes the suggestion of Lambin et. al in [57]. We finish the chapter with a discussion in Section 5.7.

5.2 Model formulation

Let u and w denote the population of cells in G2- and M/G1/S-phases, respectively. The model in this chapter will be built from a simple model given by

$$\begin{aligned} \dot{u} &= -\mu u + a w, \\ \dot{w} &= 2\mu u - a w, \end{aligned} \tag{5.3}$$

where μ is the rate of progression from G2 phase into mitosis, which results in two daughter cells entering the M/G1/S phase, and a is the rate of cell cycle

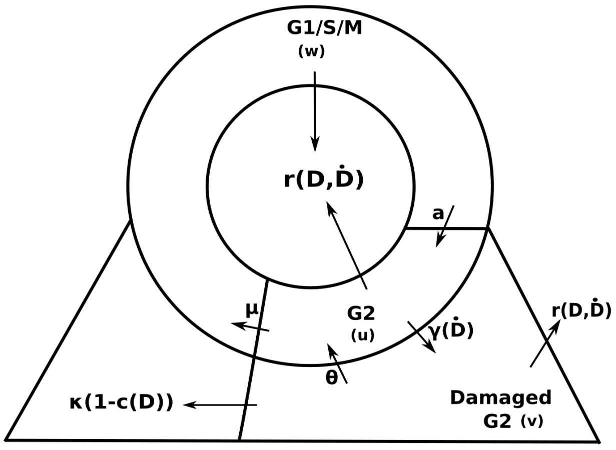

Figure 5.2: Schematics for the model in (5.4). The circle is partitioned into G2 and G1/S/M compartments. The arrows denote the rates of change between compartments. The damaged G2 compartment is an extension of the G2 compartments. The extension of the G1/S/M compartment denotes the damaged cells in mitosis that evade the G2 checkpoint.

progression from M/G1/S phase into G2 phase. We have restricted the model compartments to these two phase categories for simplicity. However, as we will see in Section 5.4, the derivation of the initial slope of the SF curve scales "nicely" with increase in the number of compartments.

We include radiation in the cell cycle dynamics (5.3), keeping in mind that the G2 checkpoint occurs in the damaged G2 phase. Thus, including the population of the damaged G2 cells, v, and the radiation terms along with their cellular interactions, we have,

$$\begin{aligned} \dot{u} &= -\mu u + aw - r_u(D(t),\dot{D}(t))u - \gamma(\dot{D}(t))u + \theta v, \\ \dot{v} &= \gamma(\dot{D}(t))u - r_v(D(t),\dot{D}(t))v - \theta v - \kappa(1-c(D(t)))v, \\ \dot{w} &= 2\mu u - aw - r_w(D(t),\dot{D}(t))w, \end{aligned} \tag{5.4}$$

where $D(t)$ denotes the total dose at time t, delivered at dose rate $\dot{D}(t)$, and is given by

$$D(t) = \int_0^t \dot{D}(z)dz.$$

A schematic of the model, illustrating the relationship between the compartments, is given in Figure 5.2. When cells are exposed to radiation, a proportion of G2-phase cells is damaged at rate $\gamma(\dot{D}(t))$. Damaged cells in the G2 phase undergo mitotic catastrophe at rate κ. The rate of mitotic catastrophe reduces when the G2 checkpoint, modeled by $c(D)$, is activated. $c(D) = 1$ corresponds to a fully activated checkpoint and $c(D) = 0$ corresponds to the state when the checkpoint is not activated. The activation of this checkpoint arrests the damaged cells in the v compartment in order to give time for repair which occurs at a rate, θ.

We model the checkpoint dynamics by the function $c(D)$, defined as

$$c(D) \quad = \quad \frac{1}{2}\Big[1 + \tanh\Big(\frac{6}{D_2 - D_1}\big(D - \frac{D_1 + D_2}{2}\big)\Big)\Big]. \tag{5.5}$$

We denote D_1 as the dose threshold below which the checkpoint fails to be activated ($c(D) \approx 0,\ \forall D < D_1$), and D_2 as the dose threshold above which the checkpoint is fully activated ($c(D) \approx 1,\ \forall D \geq D_2$) and damaged cells are arrested for repair. These thresholds are chosen to be in line with the experimental results in [53]. Figure 5.3 illustrates the profile of the checkpoint function $c(D)$. This conforms to the hypothesis of Joiner et. al. in [45], which suggests that for HRS to occur at low doses, there must be a dose-sensing threshold below which damage is not sufficient to activate the repair mechanism. The half- saturation constant is given by $\frac{D_1+D_2}{2}$ and the slope of the curve is given by $\frac{6}{D_2-D_1}$. We are not particularly concerned whether the G2 checkpoint is activated as a result of more damaged cells or as a result of more damaged sites in a single cell. The dose-dependence of this checkpoint function, $c(D)$, is sufficient to take care of these concerns.

The two direct radiation effects on the cells are mainly the radiation-induced DNA damage and death, which occur at rates γ and r_i, with $i = \{u,\ v,\ w\}$, respectively. We model the radiation-induced damage in the G2 cells as proposed in [89], that is,

$$\gamma(\dot{D}(t)) \quad = \quad 2\gamma_0 \frac{\eta \dot{D}(t)}{1 + (\eta \dot{D}(t))^2}, \tag{5.6}$$

where γ_0 is the maximum damage rate and $\eta = \frac{1}{\dot{D}_{\mathrm{M}}}$ denotes the reciprocal

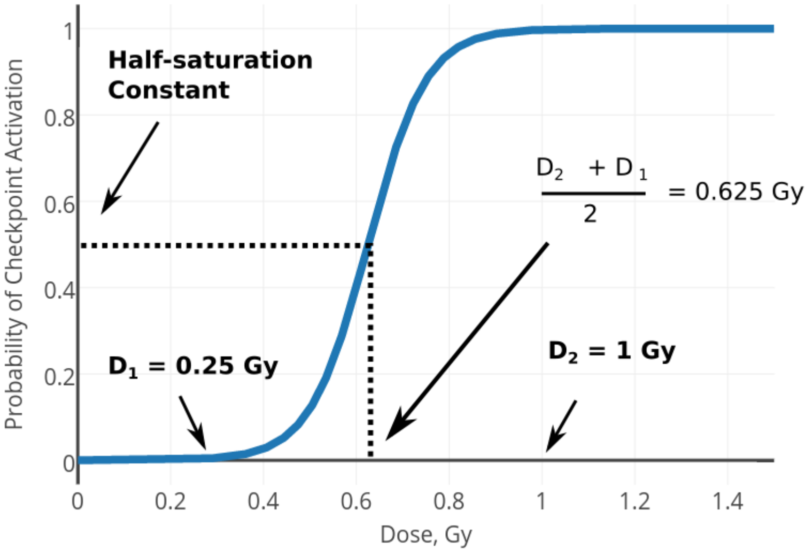

Figure 5.3: The profile of the G2 checkpoint functional. The lower threshold below which DNA is not recognized and the upper threshold above which the damaged cells are completely arrested for repair are given by $D_1 = 0.25$ Gy and $D_2 = 1$ Gy, respectively.

of the dose rate $\dot{D}_{\text{M}}$ at which the radiation damage is maximal in a cell. We model the radiation-induced death rate by the radiation hazard function in [34], given by

$$r_i(D(t), \dot{D}(t)) \quad = \quad (\alpha_i + \beta_i D)\dot{D}(t), \tag{5.7}$$

where α_i and β_i are as described in the LQ model for the different cycle phases, $i = u,\ v,\ w$.

We note here that the method we will use to derive the initial slope of the SF curve in Section 5.4 only works when the parameters and functions of the model (5.4) are independent of time. Therefore, we restrict the analysis to a time interval of constant radiation $[0, t_0]$ such that on this time interval the dose rate $\dot{D}(t) = \frac{D}{t_0}$ is constant. Since we are only interested in the first period of radiation exposure of length t_0, we can drop the time dependence of

(5.6)-(5.7) as follows:

$$\gamma\Big(\frac{D}{t_0}\Big) \;=\; \frac{2\gamma_0\eta\frac{D}{t_0}}{1+\big(\eta\frac{D}{t_0}\big)^2} \quad\text{and}\quad r_i\Big(D,\frac{D}{t_0}\Big) \;=\; (\alpha_i+\beta_i D)\frac{D}{t_0}. \qquad (5.8)$$

In the definition of $c(D(t))$, the checkpoint functional depends on the total dose given over total time, t_0. Then,

$$D(t) = \int_0^{t_0} \frac{D}{t_0} ds = D.$$

This implies that at time t_0 we have

$$c(D) \;=\; \frac{1}{2}\Big[1+\tanh\Big(\frac{6}{D_2-D_1}\big(D-\frac{D_1+D_2}{2}\big)\Big)\Big], \quad \forall\ t\geq t_0. \qquad (5.9)$$

The data fitting in Section 5.3 and the derivation of the initial slope of the SF curve in Section 5.4 will be based on model (5.4) with time independent parameters and functions, namely

$$\begin{aligned}
\dot{u} &= -\mu u + aw - r_u\Big(D,\frac{D}{t_0}\Big)u - \gamma\Big(\frac{D}{t_0}\Big)u + \theta v,\\
\dot{v} &= \gamma\Big(\frac{D}{t_0}\Big)u - r_v\Big(D,\frac{D}{t_0}\Big)v - \theta v - \kappa(1-c(D))v, \qquad (5.10)\\
\dot{w} &= 2\mu u - aw - r_w\Big(D,\frac{D}{t_0}\Big)w,
\end{aligned}$$

for $0\leq t\leq t_0$. The terms $\gamma\big(\frac{D}{t_0}\big)$, $r_i\big(D,\frac{D}{t_0}\big)$, and $c(D)$ are given by (5.8) and (5.9), respectively.

5.3 Data fitting and numerical simulation

In this section, we fit a simplified version of model (5.10) to the surviving fraction data of different cell lines (both synchronous and asynchronous cells), and estimate the model parameters with their 95% credible intervals. All of the cell lines in [53, 73, 66, 69, 118, 108] have been shown to exhibit the low-dose HRS phenomenon, although with varying degrees.

We will define the surviving fraction in the context of model (5.4). This is crucial because the formulas for the surviving fraction in both the LQ and the IR models do not account for the duration of the radiation exposure. The duration of the radiation exposure will be very significant in our analysis. Thus, we give the following definition:

Definition 6. *The surviving fraction $SF(D,t)$ of cells at total dose D and time t from model (5.10) is given by*

$$SF(D,t) \quad = \quad \frac{u(D,t)+v(D,t)+w(D,t)}{u_0+w_0}, \tag{5.11}$$

where $u(D,t)$, $v(D,t)$, and $w(D,t)$ are the cell populations at time t and after radiation dose D in G2, damaged G2, and M/G1/S phases, respectively. We denote $u_0 = u(0,0)$ and $w_0 = w(0,0)$ as the initial populations of cells in G2 and M/G1/S phases, respectively, before radiation exposure started.

We fit the surviving fraction $SF(D,t_0)$ as defined in (5.11), to SF data over a radiation exposure time t_0 chosen to be too short to accommodate both cell cycle progression and damage repair. This will be among the cases we will consider in the next section. As noted earlier, we will assume that the SF computed from model (5.10) is a good approximation to the experimental values of SF. Since the duration of radiation exposure is very short, we will also assume that the cell cycle progression rates μ, a and the DNA repair rate θ are zero in the simulation.

Thus, the simplification of model (5.10) that we will fit to the asynchronous data, for $0 \leq t \leq t_0$, is given by

$$\begin{aligned} \dot{u} &= -r_u\Big(D,\frac{D}{t_0}\Big)u-\gamma\Big(\frac{D}{t_0}\Big)u, \\ \dot{v} &= \gamma\Big(\frac{D}{t_0}\Big)u-r_v\Big(D,\frac{D}{t_0}\Big)v-\kappa(1-c(D))v, \\ \dot{w} &= -r_w\Big(D,\frac{D}{t_0}\Big)w. \end{aligned} \tag{5.12}$$

For the synchronous cell population, model (5.12) will be extended to accommodate all the phases of the cell cycle. Thus, for $0 \leq t \leq t_0$, we have

$$\begin{aligned}
\dot{u} &= -r_u\Big(D, \frac{D}{t_0}\Big)u - \gamma\Big(\frac{D}{t_0}\Big)u, \\
\dot{v} &= \gamma\Big(\frac{D}{t_0}\Big)u - r_v\Big(D, \frac{D}{t_0}\Big)v - \kappa(1 - c(D))v, \\
\dot{z} &= -r_z\Big(D, \frac{D}{t_0}\Big)z, \\
\dot{w} &= -r_w\Big(D, \frac{D}{t_0}\Big)w, \\
\dot{s} &= -r_s\Big(D, \frac{D}{t_0}\Big)s,
\end{aligned} \tag{5.13}$$

where $u,\ v,\ z,\ w,\ s$ denote the population of cells in healthy G2, damaged G2, M-, G1, and S phases, respectively. We have also excluded the cell cycle rates, $\mu,\ a$, and the DNA repair rate θ because the duration of radiation exposure t_0 of interest is assumed to be too short to accommodate such dynamics.

In particular, we are interested in using formula (5.26) derived in Section 5.4 to estimate the initial slope of the SF curve of these cell lines using the parameter values for $\gamma_0,\ \kappa,\ \eta,\ D_1,\ D_2,\ \alpha,\ \text{and}, \beta$ that will be estimated in this section. Notice that we have dropped the subscripts in the α's and β's in the data fitting. This is because in most of the literature, it is usually assumed that $\alpha := \alpha_i$ and $\beta := \beta_i$ for all $i \in \{u,\ v,\ w\}$ in the asynchronous cell population. Similarly for the synchronous cell population, we will also assume that $\alpha := \alpha_i$ and $\beta := \beta_i$ for all $i \in \{u,\ v,\ z,\ w,\ s\}$ and that α and β parameters will denote the radio-responsiveness of the enriched phase of the cell cycle. The ultimate goal is to compare these computed values of initial slope of the SF curve to the data in Figure 2 in [45].

The surviving fraction data of the various cell lines considered in this chapter [53, 73, 66, 69, 118, 108] were measured from experiments where cells were irradiated with single doses of X-rays between 0.05 and 6 Gy at dose rates ranging between 0.2-0.5 Gy/min. The surviving fraction of cells after exposure to a single dose was measured using a Cell Sorter. Most data points represent multiple measurements and are denoted as mean ± standard deviation. Cell survival was described in terms of their ability to form a colony (i.e., reproduce at least 50 offspring after radiation exposure) and cells which are unable to form a colony do not survive.

In this data fitting, we employ an implementation of the Goodman and Weare Affine invariant ensemble Markov Chain Monte Carlo (MCMC) sampler [35] to fit the model to the available surviving fraction datasets. The affine invariance property of this routine enables a much faster convergence even for badly scaled problems. This implementation takes, as an input, a log-likelihood function of the experimental data and a log-prior of each parameter. We assume an exponential distribution for the surviving fraction data. We also assume a uniform distribution for the prior of each parameter over the prescribed intervals of biologically relevant values. The posterior distribution for each parameter, which is one of the outputs of the fitting procedure, is Gaussian. The 95% credible interval for each parameter is then computed from the respective posterior distribution. It is important to clarify that the model fits shown in Figures 5.4 and 5.5 are the median of the posterior distribution for each parameter.

In the following subsections, we will respectively fit models (5.12) and (5.13) to the asynchronous and synchronous cell data.

5.3.1 Asynchronous cell lines

In this subsection, we fit model (5.12) to the SF data of the following asynchronous cell lines: MR4 [53], PC3 [73], V79 [66], V79ox [69], V79hyp [69], A549 [118], HT29 [118], U1 [118], T98G [108], and RWPE1 [73] cells. As mentioned earlier, these data describe the survival of cells after exposure to a single dose of 240kvp X-rays radiation. Doses between 0.05 and 6 Gy were delivered at dose rates ranging between 0.2 - 0.5 Gy/min. Since there is no specific detail of which dose was delivered at a particular dose rate, we assume that every dose was delivered over a period of 10 mins. This assumption is fair because standard radiation technique delivers doses with appropriate dose rate over 10 mins. We assume that these asynchronous cells consist of 63% G1-phase cells, 19.35% S-phase cells, and 17.65% G2-phase cells. This assumption is based on the mean of the proportion of cells in each phase that

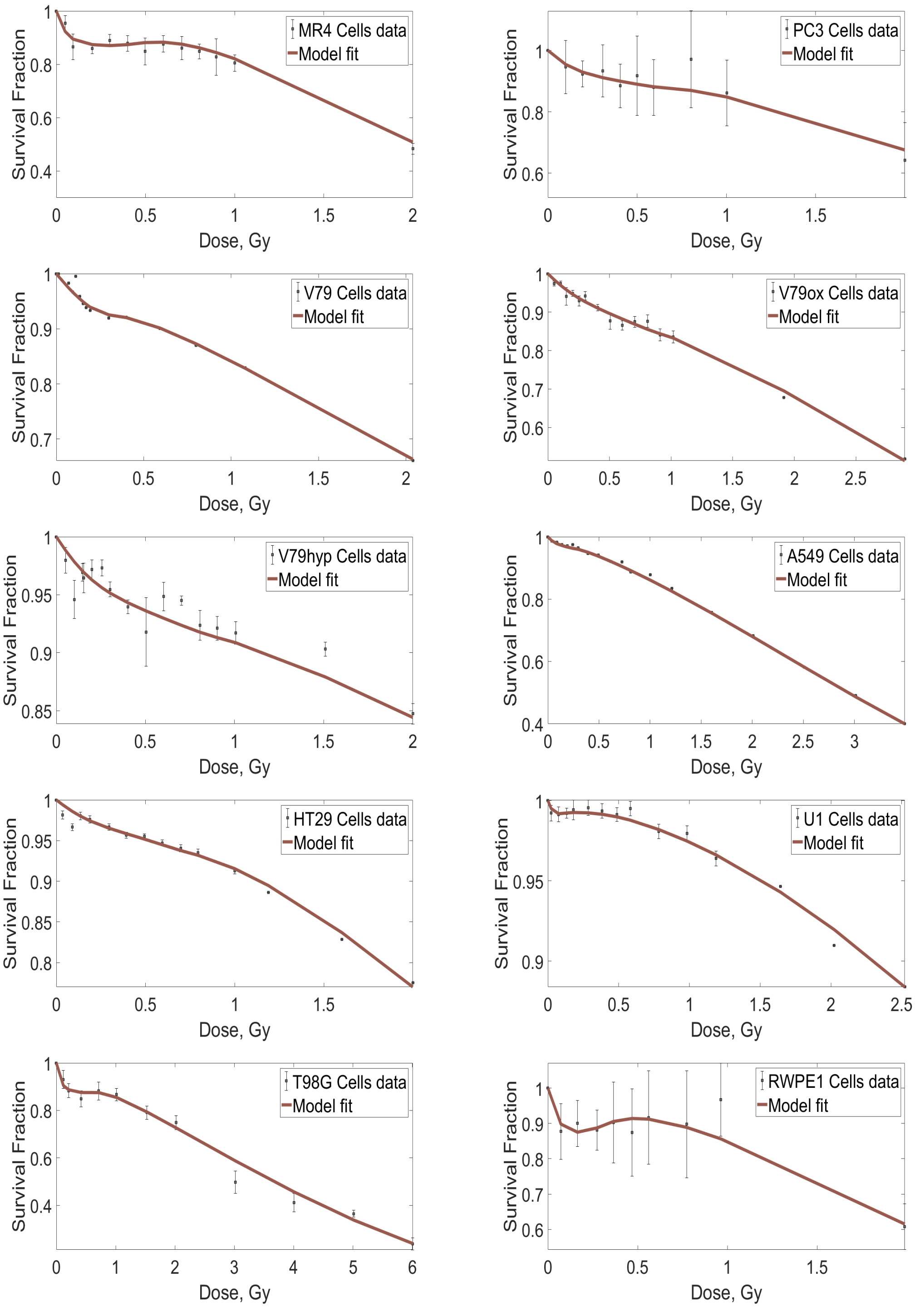

Figure 5.4: Data fitting for the asynchronous cell population data. Model (5.12) is fitted to the surviving fraction data of ten different asynchronous cell populations. The data are shown with error bars. The best fit, computed from the median of each parameter posterior distribution, is shown in red.

constitute asynchronous cell population in [67]. The values of the parameters and their respective 95% credible intervals from the data fitting are given in Table 5.1.

5.3.2 Synchronous cell lines

In this subsection, we fit model (5.13) to the SF data of the V79, T98G, and U373 cell lines available for enriched G1, S and G2 phases in [67, 108], respectively. The proportion of cells in different cell cycle phases at the time of radiation for the synchronous cell population are found in [67]. The estimated parameter values in this subsection are in Table 5.2 and the corresponding fits are in Figure 5.5.

Notice that in Figure 5.5, some of the cell lines enriched with non-G2-phase cells also display the HRS phenomenon. In the middle row of Figure 5.5, both the T98G cell lines enriched with G1-phase and S-phase cells, respectively, exhibit a small measure of HRS. These two cell lines contain a sizable proportion of G2-phase cells. For instance, according to the surviving fraction data from [67], the T98G cell line enriched with G1-phase cells contains 85% G1-phase cells, 4.7% S-phase cells, and 10.3% G2-phase cells. The relatively high proportion of G2-phase cells in this cell line explains the observed HRS. In contrast, HRS is not observed in the V79 and U373 cell lines enriched with either G1-phase cells or S-phase cells. These cells lines contain a negligible proportion of G2-phase cells. For example, according to the surviving fraction from [67], both V79 and U373 cell lines enriched with G1-phase cells contain 95.2% G1-phase cells, 4.7% S-phase cells, and only 0.1% G2-phase cells. This suggests that if we can synchronize the cell lines to be pure (contain only non-G2-phase cells or only G2-phase cells), we might be better convinced that the HRS phenomenon is exclusive to G2-phase cells.

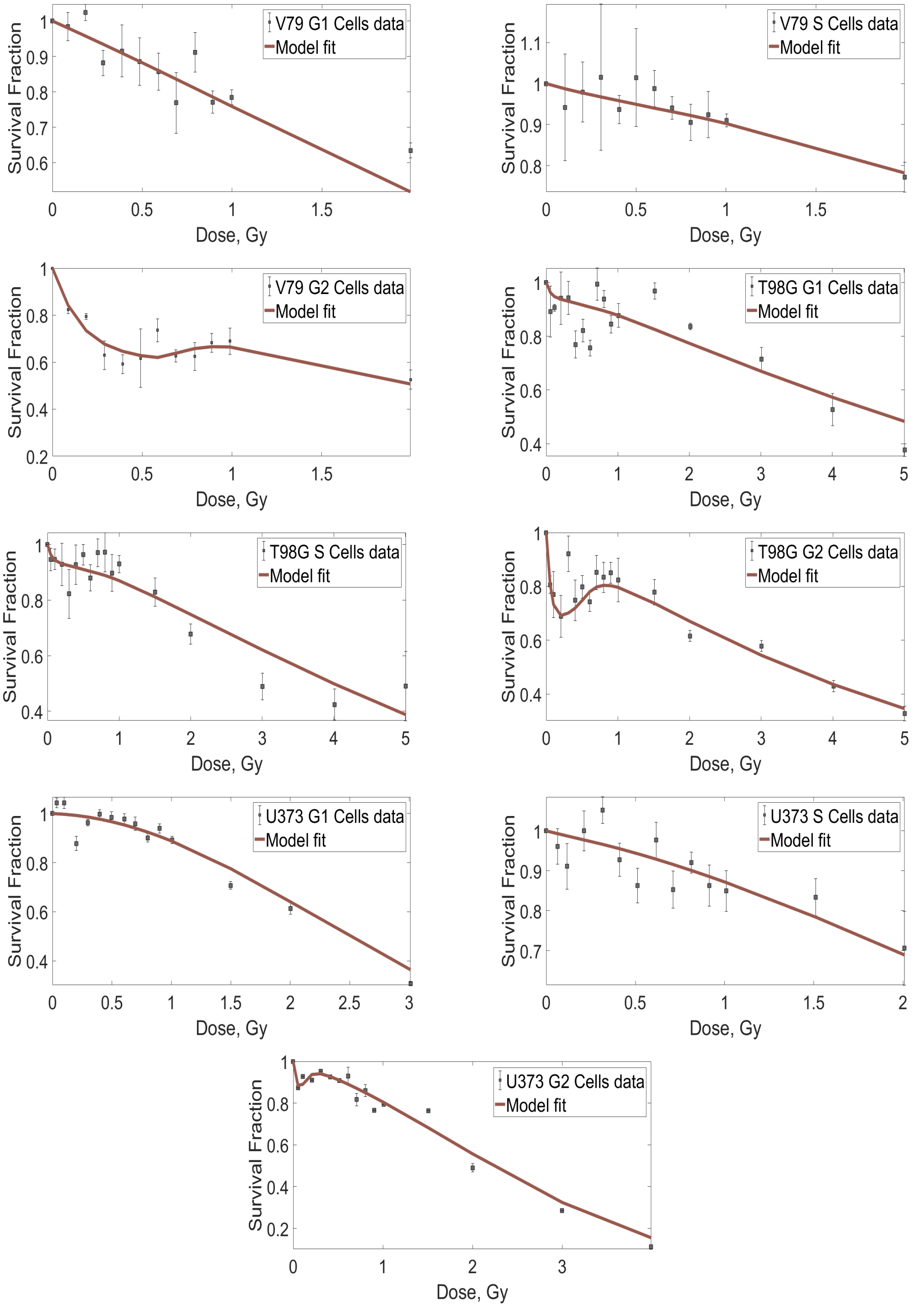

Figure 5.5: Data fitting for the synchronous cell population data. Model (5.13) is fitted to the surviving fraction data of three different synchronous cell populations. The data are shown with error bars. The best fit, computed from the median of each parameter posterior distribution, is shown in red.

Cell line	γ_0	κ	η	d_1	d_2	$-\alpha$	$-\beta$
MR4	0.255 ± 0.009	0.205 ± 0.009	50.75 ± 1.287	0.105 ± 0.009	0.575 ± 0.009	0.042 ± 0.002	0.160 ± 0.018
PC3	0.138 ± 0.049	0.115 ± 0.044	29.93 ± 6.450	0.370 ± 0.065	0.720 ± 0.208	0.113 ± 0.066	0.050 ± 0.030
V79	0.081 ± 0.0441	0.137 ± 0.073	23.87 ± 9.663	0.086 ± 0.038	0.379 ± 0.199	0.158 ± 0.016	0.030 ± 0.012
V79ox	0.128 ± 0.076	0.091 ± 0.059	17.74 ± 8.078	0.506 ± 0.188	1.057 ± 0.303	0.120 ± 0.054	0.044 ± 0.028
V79hyp	0.066 ± 0.036	0.092 ± 0.068	25.35 ± 9.516	0.503 ± 0.190	1.052 ± 0.303	0.086 ± 0.031	0.003 ± 0.002
A549	0.066 ± 0.036	0.040 ± 0.030	90.40 ± 12.31	0.155 ± 0.038	0.261 ± 0.060	0.119 ± 0.035	0.045 ± 0.026
HT29	0.092 ± 0.029	0.055 ± 0.029	25.22 ± 8.776	0.425 ± 0.086	0.848 ± 0.184	0.033 ± 0.016	0.055 ± 0.018
U1	0.058 ± 0.019	0.024 ± 0.007	149.99± 8.00	0.035 ± 0.008	0.600 ± 0.032	0.013 ± 0.004	0.017 ± 0.004
T98G	0.201 ± 0.065	0.165 ± 0.073	47.59 ± 5.657	0.110 ± 0.022	0.792 ± 0.392	0.135 ± 0.033	0.018 ± 0.009
RWPE1	0.300 ± 0.016	0.190 ± 0.016	55.65 ± 7.570	0.015 ± 0.008	0.385 ± 0.318	0.085 ± 0.023	0.090 ± 0.030

Table 5.1: Estimated parameter values and their respective 95% credible intervals from fitting model (5.12) to the SF data of the listed asynchronous cell lines.

5.4 Derivation of the initial slope of the SF curve from the model

In the previous section, we have numerically shown that the model we formulated in this chapter can describe the low-dose HRS phenomenon observed in both synchronous and asynchronous cells. In this section, we will derive the formula for computing the initial slopes of these surviving fraction curves.

From the LQ and the IR models in (5.1) and (5.2), we have

$$\frac{\partial}{\partial D} SF_0(D)\Big|_{D=0} = -\alpha, \quad \text{and} \quad \frac{\partial}{\partial D} SF_1(D)\Big|_{D=0} = -\alpha_s. \tag{5.14}$$

Cell line	γ_0	κ	η	d_1	d_2	$-\alpha$	$-\beta$
V79 G1	0.159 ± 0.079	0.103 ± 0.062	23.77 ± 9.743	0.400 ± 0.058	0.700 ± 0.231	0.250 ± 0.013	0.052 ± 0.023
V79 S	0.162 ± 0.082	0.105 ± 0.064	23.67 ± 9.437	0.400 ± 0.059	0.698 ± 0.220	0.085 ± 0.007	0.025 ± 0.007
V79 G2	0.160 ± 0.069	0.103 ± 0.059	23.60 ± 7.349	0.399 ± 0.042	0.695 ± 0.172	0.303 ± 0.036	0.026 ± 0.016
T98G G1	0.185 ± 0.035	0.118 ± 0.041	65.02 ± 11.80	0.200 ± 0.046	0.964 ± 0.321	0.130 ± 0.023	0.005 ± 0.002
T98G S	0.185 ± 0.011	0.115 ± 0.033	64.89 ± 10.90	0.201 ± 0.046	0.9 ± 0.153	0.130 ± 0.022	0.014 ± 0.001
T98G G2	0.151 ± 0.062	0.110 ± 0.062	55.20 ± 7.062	0.150 ± 0.061	0.701 ± 0.130	0.21 ± 0.014	0.003 ± 0.001
U373 G1	0.091 ± 0.048	0.070 ± 0.028	145.13± 9.712	0.009 ± 0.003	0.291 ± 0.061	0.020 ± 0.011	0.111 ± 0.039
U373 S	0.100 ± 0.042	0.071 ± 0.021	14.48 ± 1.069	0.010 ± 0.003	0.291 ± 0.045	0.100 ± 0.042	0.051 ± 0.023
U373 G2	0.076 ± 0.033	0.065 ± 0.021	144.63± 11.53	0.009 ± 0.003	0.225 ± 0.038	0.160 ± 0.015	0.078 ± 0.004

Table 5.2: Estimated parameter values and their respective 95% credible intervals from fitting model (5.13) to the SF data of the listed synchronous cell lines.

This implies that $-\alpha$ and $-\alpha_s$ are the initial slopes of the surviving fraction curve determined by both the LQ and the IR models, respectively. Hence, in order to derive the initial slope of the surviving fraction curve determined by model (5.12), it suffices to compute

$$-\alpha_s := \frac{\partial SF(D,t_0)}{\partial D}\Big|_{D=0} = \frac{\frac{\partial u}{\partial D}(D,t_0) + \frac{\partial v}{\partial D}(D,t_0) + \frac{\partial w}{\partial D}(D,t_0)}{u_0 + w_0}\Big|_{D=0}, \quad (5.15)$$

where $\frac{\partial u}{\partial D}$, $\frac{\partial v}{\partial D}$, and $\frac{\partial w}{\partial D}$ denote the partial derivatives of u, v, and w, with respect to D. t_0 is the time at which the surviving fraction data is measured. Throughout this chapter, the surviving fraction from the above model will be computed right after radiation exposure. Invariably, this implies that t_0 is the radiation exposure time. In the following two subsections, we will derive the initial slope of the SF curve from model (5.12) for the two cases that t_0 is

1. too short to accommodate both cell cycle progression and damage repair, and
2. too short to accommodate cell cycle progression but sufficient to accommodate damage repair.

The biological implications of these two cases will be discussed in Section 5.7.

5.4.1 Radiation exposure time too short for both repair of damage and cell progression

Model (5.10) can be written in vector form as

$$\begin{pmatrix} u & v & w \end{pmatrix}_t^T = A \begin{pmatrix} u & v & w \end{pmatrix}^T, \tag{5.16}$$

where

$$A = \begin{pmatrix} -\mu - r_u\big(D, \frac{D}{t_0}\big) - \gamma\big(\frac{D}{t_0}\big) & \theta & a \\ \gamma\big(\frac{D}{t_0}\big) & -r_v\big(D, \frac{D}{t_0}\big) - \kappa(1 - c(D)) - \theta & 0 \\ 2\mu & 0 & -a - r_w\big(D, \frac{D}{t_0}\big) \end{pmatrix}. \tag{5.17}$$

If we assume that the radiation time is too small to accommodate cycle progression and cell repair, matrix A then becomes

$$A = \begin{pmatrix} -r_u\big(D, \frac{D}{t_0}\big) - \gamma\big(\frac{D}{t_0}\big) & 0 & 0 \\ \gamma\big(\frac{D}{t_0}\big) & -r_v\big(D, \frac{D}{t_0}\big) - \kappa(1 - c(D)) & 0 \\ 0 & 0 & -r_w\big(D, \frac{D}{t_0}\big) \end{pmatrix}, \tag{5.18}$$

so that model (5.10) can be approximated by the reduced system in (5.12).

System (5.12) can be solved explicitly with solution

$$\begin{pmatrix} u & v & w \end{pmatrix}^T = \sum_{i=1}^{3} l_i e^{\lambda_i t} E_i, \tag{5.19}$$

where λ_i is the eigenvalue of A that corresponds to eigenvector E_i for each $i = \{u,\ v,\ w\}$. To this end, let λ denote an eigenvalue of A. $|A - \lambda I| = 0$ implies

$$\lambda_1 = -r_u\big(D, \frac{D}{t_0}\big) - \gamma\big(\frac{D}{t_0}\big),\ \lambda_2 = -r_v\big(D, \frac{D}{t_0}\big) - \kappa(1 - c(D)),\ \lambda_3 = -r_w\big(D, \frac{D}{t_0}\big). \tag{5.20}$$

For each λ_i, the corresponding eigenvector E_i is given by

$$E_1 = \begin{pmatrix}1 & m & 0\end{pmatrix}^T,\quad E_2 = \begin{pmatrix}0 & 1 & 0\end{pmatrix}^T \quad \text{and} \quad E_3 = \begin{pmatrix}0 & 0 & 1\end{pmatrix}^T, \tag{5.21}$$

with

$$m = \frac{-\gamma\big(\frac{D}{t_0}\big)}{-r_v\big(D, \frac{D}{t_0}\big) - \kappa(1 - c(D)) + r_u\big(D, \frac{D}{t_0}\big) + \gamma\big(\frac{D}{t_0}\big)}.$$

Thus, (5.19) with the corresponding eigenvalues and eigenvectors in (5.20) and (5.21) forms the general solution for system (5.12). Now, using the initial conditions $u(0) = u_0,\ v(0) = 0,\ w(0) = w_0$, we have

$$u(t) = u_0 e^{-\left(\gamma\left(\frac{D}{t_0}\right) + r_u\left(D, \frac{D}{t_0}\right)\right)t}, \tag{5.22}$$

$$v(t) = u_0 m\Big(e^{-\left(\gamma\left(\frac{D}{t_0}\right) + r_u\left(D, \frac{D}{t_0}\right)\right)t} - e^{-\left(r_v\left(D, \frac{D}{t_0}\right) + \kappa(1 - c(D))\right)t}\Big), \tag{5.23}$$

$$w(t) = w_0 e^{-r_u\left(D, \frac{D}{t_0}\right)t}. \tag{5.24}$$

Since

$$\frac{\partial}{\partial D}\gamma\big(\frac{D}{t_0}\big)\Big|_{D=0} = \frac{2\gamma_0\eta}{t_0},\quad \gamma\big(\frac{D}{t_0}\big)\Big|_{D=0} = 0,\quad \text{and}$$
$$r_i'\big(D, \frac{D}{t_0}\big)\Big|_{D=0} = \frac{\alpha_i}{t_0},\quad r_i\big(D, \frac{D}{t_0}\big)\Big|_{D=0} = 0, \qquad \forall i = \{u,\ v,\ w\},$$

the partial derivatives of u, v, w with respect to D, evaluated at $D = 0$ and at time t_0, are given by

$$
\begin{aligned}
\frac{\partial u}{\partial D}(D, t_0)\Big|_{D=0} &= -(2\gamma_0\eta + \alpha_u)u_0, \\
\frac{\partial v}{\partial D}(D, t_0)\Big|_{D=0} &= u_0 m'(0)\big(1 - e^{-\kappa t_0(1-c(0))}\big), \\
\frac{\partial w}{\partial D}(D, t_0)\Big|_{D=0} &= -\alpha_w w_0,
\end{aligned}
$$

so that

$$
\begin{aligned}
-\alpha_s := \frac{\partial SF(D, t_0)}{\partial D}\Big|_{D=0} &= -\frac{\alpha_u u_0 + \alpha_w w_0}{u_0 + w_0} \\
&\quad -\Big(\frac{u_0}{u_0 + w_0}\Big)\Big(2\gamma_0\eta - m'(0)(1 - e^{-\kappa t_0}\Big), \\
&= -\frac{\alpha_u u_0 + \alpha_w w_0}{u_0 + w_0} \\
&\quad -2\gamma_0\eta\Big(\frac{u_0}{u_0 + w_0}\Big)\Big(1 - \frac{1 - e^{-\kappa t_0}}{\kappa t_0}\Big). \qquad (5.25)
\end{aligned}
$$

However, for asynchronous cell population where $\alpha := \alpha_u = \alpha_w$, (5.25) simplifies to

$$
-\alpha_s := \frac{\partial SF(D, t_0)}{\partial D}\Big|_{D=0} = -\alpha - 2\gamma_0\eta\Big(\frac{u_0}{u_0 + w_0}\Big)\Big(1 - \frac{1 - e^{-\kappa t_0}}{\kappa t_0}\Big), \tag{5.26}
$$

where the direct radiation effect is clearly described by $-\alpha$, which is the rate at which single radiation tracks produce lethal lesion in a general cell population. Moreover, for small radiation exposure time, t_0, using Taylor expansion, we get a more compact form given by

$$
-\alpha_s := \frac{\partial SF(D, t_0)}{\partial D}\Big|_{D=0} \approx -\alpha - \gamma_0\eta\Big(\frac{u_0}{u_0 + w_0}\Big)\kappa t_0. \tag{5.27}
$$

(5.27) reveals that the slope of the SF curve after a short duration of radiation exposure is controlled by two components, namely the direct effect of radiation (captured by the first term on the RHS of (5.27)) and the indirect effect of radiation (captured by the second term on the RHS of (5.27)). The impact of this second term on $-\alpha_s$ is controlled by the proportion of cells in G2-phase. This is largely because the other parameters in the second term on RHS of (5.27) belong to the cells in the G2 phase of the cell cycle. This confirms the essence of the initial distribution of cells in various phases of the cell cycle at the time of radiation exposure on the low-dose HRS phenomenon hypothesized in [45, 106, 67]. In fact, for synchronous cells enriched in G2-phase, the slope of the SF curve will be steeper because of the significant contributions from both the direct and the indirect radiation effects. On the other hand, for any synchronous cells enriched in non-G2-phase, the steepness of the slope is mainly controlled by the direct radiation effect $-\alpha$ with very little contribution from the indirect radiation effect.

We also observe that the second term on the RHS of (5.27) is dominated by the parameter κ, denoting the rate of mitotic catastrophe. This implies that a major determinant of the degree of HRS is the rate of death of the G2-phase cells which evade the checkpoint activity.

5.4.2 Radiation exposure time too short for cell progression but sufficient enough for damage repair

In the previous subsection, we considered the case where the SF is computed right after radiation exposure whose duration is too short to accommodate cell cycle progression and DNA damage repair. Now we compute the surviving fraction immediately after a radiation exposure whose duration is long enough to accommodate repair but not sufficient to have any significant cycle progression. It is interesting to understand how the repair mechanism impacts the initial slope of the SF curve in this case. This problem is simply equivalent to solving (5.16) with A given by

$$A = \begin{pmatrix} -r_u\big(D, \frac{D}{t_0}\big) - \gamma\big(\frac{D}{t_0}\big) & \theta & 0 \\ \gamma\big(\frac{D}{t_0}\big) & -r_v\big(D, \frac{D}{t_0}\big) - \kappa(1-c(D)) - \theta & 0 \\ 0 & 0 & -r_w\big(D, \frac{D}{t_0}\big) \end{pmatrix}. \tag{5.28}$$

Notice that the difference between this matrix and the one in the previous subsection in (5.18) is the nonzero parameter θ in (5.28). As a check, this derivation should result in that of the last subsection when $\theta = 0$.

Following the technique used in the last subsection, we can solve this system analytically to derive the following solution (where we have dropped the arguments for simplicity)

$$\begin{aligned} u(t) &= -\frac{u_0}{2m}\big(r_u + \gamma - r_v - \theta - \kappa(1-c)\big)(e^{\lambda_+ t} - e^{\lambda_- t}) + \frac{u_0}{2}(e^{\lambda_+ t} + e^{\lambda_- t}), \quad (5.29) \\ v(t) &= \frac{u_0}{4m\theta}\Big((r_u + \gamma - r_v - \theta - \kappa(1-c))^2 - m^2\Big)\big(e^{\lambda_- t} - e^{\lambda_+ t}\big), \quad (5.30) \\ w(t) &= w_0 e^{-r_w t}, \quad (5.31) \end{aligned}$$

where $u_0 = u(0,0)$ and $w_0 = w(0,0)$, with

$$m = \sqrt{\big(r_u + \gamma + r_v + \theta + \kappa(1-c)\big)^2 - 4\big((r_u + \gamma)(r_v + \theta + \kappa(1-c)) - \theta\gamma\big)} \quad (5.32)$$

and

$$\lambda_\pm = -\frac{1}{2}\big(r_u + \gamma + r_v + \theta + \kappa(1-c)\big) \pm \frac{1}{2}m. \quad (5.33)$$

By computing $\frac{\partial u}{\partial D}\big|_{D=0}$, $\frac{\partial v}{\partial D}\big|_{D=0}$, and $\frac{\partial w}{\partial D}\big|_{D=0}$, we can evaluate (5.15) to get

$$\begin{aligned} \frac{\partial SF(D,t_0)}{\partial D}\Big|_{D=0} &= -\Big(\frac{\alpha_u u_0 + \alpha_w w_0}{u_0 + w_0}\Big) \\ &\quad -2\gamma_0\eta\Big(\frac{u_0}{u_0 + w_0}\Big)\Big(1 - \frac{\theta}{(\kappa+\theta)t_0} - \kappa\big(\frac{1 - e^{-(\kappa+\theta)t_0}}{(\kappa+\theta)^2 t_0}\big)\Big). \end{aligned} \quad (5.34)$$

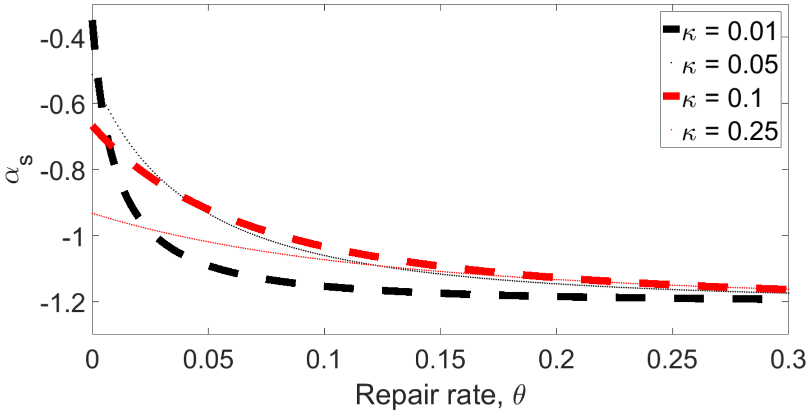

Figure 5.6: The profile of the initial slope of the SF curve as a function of repair rate θ, at different rates of mitotic catastrophe κ. The black dashed curve is for $\kappa = 0.01$, the black dotted curve is for $\kappa = 0.05$, the red dashed curve is for $\kappa = 0.1$, and the red dotted curve is for $\kappa = 0.25$.

As before, assuming $\alpha_u = \alpha_w = \alpha$, (5.34) reduces to

$$\begin{aligned} -\alpha_s &:= \frac{\partial SF(D,t_0)}{\partial D}\Big|_{D=0} \\ &= -\alpha - 2\gamma_0\eta\Big(\frac{u_0}{u_0+w_0}\Big)\Big(1 - \frac{\theta}{(\kappa+\theta)t_0} - \kappa\big(\frac{1-e^{-(\kappa+\theta)t_0}}{(\kappa+\theta)^2 t_0}\big)\Big). \end{aligned} \tag{5.35}$$

After Taylor expansion for small t_0, we can get a more compact form given by

$$-\alpha_s := \frac{\partial SF(D,t_0)}{\partial D}\Big|_{D=0} = -\alpha - 2\gamma_0\eta\Big(\frac{u_0}{u_0+w_0}\Big)\Big(\frac{\kappa t_0}{2} + \frac{\theta(t_0-1)}{t_0(\kappa+\theta)}\Big). \tag{5.36}$$

As noted earlier, we see that (5.26) is a special case of (5.35) when $\theta = 0$. We can also understand the interaction between the rate of repairing DNA damage and the mitotic catastrophe experienced by damaged G2-phase cells that eventually culminates into the HRS phenomenon through (5.35). For example in Figure 5.6, we see that for small mitotic catastrophic rate κ, the slope $-\alpha_s$ of the SF curve is more sensitive to changes in the DNA repair rate θ than for larger values of κ. Thus, the slope $-\alpha_s$ of the SF curve depends on

	MR4	PC3	V79	V79 ox	V79 hyp	A549	HT29	U1	T98G	RWPE1
$-\alpha_s$	2.727± 0.774	0.703± 0.448	0.470± 0.280	0.394± 0.3032	0.289± 0.215	0.484± 0.362	0.222± 0.162	0.353± 0.186	1.858± 1.057	3.230± 0.810
$\frac{\alpha_s}{\alpha}$	64.94	6.241	2.981	3.294	3.368	4.068	6.784	28.24	13.78	37.15
SF_2	0.483	0.643	0.674	0.667	0.847	0.682	0.775	0.910	0.748	0.607

Table 5.3: Computed values of $\frac{\alpha_s}{\alpha}$ and literature values of the SF_2 for asynchronous cell lines. The mean ± SD of $-\alpha_s$ are computed from (5.26) using the estimated parameters in Table 5.1; values of $\frac{\alpha_s}{\alpha}$ are computed using the mean of $-\alpha_s$ and the values of $-\alpha$ from Table 5.1; SF_2 data are taken from the respective literature.

the relationship between the rates of mitotic catastrophe κ and DNA repair θ.

Furthermore, it is worth noting that (5.25) and (5.34) scale nicely with increase in the number of model compartments. For example, suppose model (5.10) has n compartments, where u_{i_0} and u_i denote the cell population at time, $t = 0$, and at any time, $t > 0$, respectively, with $i = 1, \ldots, n$. Let $i = 1$ denote the compartment for the G2-phase cells, then (5.25) and (5.34) become

$$\begin{aligned} -\alpha_s := \frac{\partial SF(D,t_0)}{\partial D}\Big|_{D=0} &= -\frac{\sum_{i=1}^{n} \alpha_i u_{i_0}}{\sum_{i=1}^{n} u_{i_0}} - 2\gamma_0\eta\Big(\frac{u_{1_0}}{\sum_{i=1}^{n} u_{i_0}}\Big)\kappa t_0, \quad (5.37) \\ &= -\frac{\sum_{i=1}^{n} \alpha_i u_{i_0}}{\sum_{i=1}^{n} u_{i_0}} \\ &\quad -2\gamma_0\eta\Big(\frac{u_{1_0}}{\sum_{i=1}^{n} u_{i_0}}\Big)\Big(\frac{\kappa t_0}{2} + \frac{\theta(t_0-1)}{t_0(\kappa+\theta)}\Big). \quad (5.38) \end{aligned}$$

This implies that an increase in the number of model compartments only affects direct radiation effects.

In the next section, we will validate these derivations against the data for the $-\alpha_s$ of the ten different asynchronous cell lines and three different synchronous cell lines used earlier in Section 5.3. We are interested in computing the initial slope of the SF curve using formula (5.26) and comparing it with the data in [45].

5.5 Validation of the analytical derivations of the $\frac{\alpha_s}{\alpha}$ index

In this section, we validate the analytical results of the previous section against SF data of both synchronous and asynchronous cell lines. In particular, we estimate the initial slope of the SF curve using formula (5.26) and compare it to the data in Figure 2 of Joiner et. al [45], which is the plot of $\frac{\alpha_s}{\alpha}$ vs. SF_2, the surviving fraction at 2 Gy.

The values of $-\alpha_s$ computed using formula (5.26) with parameter values in Table 5.1 and 5.2 are recorded in Table 5.3 for asynchronous cells and Table 5.4 for synchronous cells, respectively. The third row contains the value of the $\frac{\alpha_s}{\alpha}$ index for each cell line and cell cycle phase, as the case may be. The $-\alpha$ values used in the computation of $\frac{\alpha_s}{\alpha}$ index are from Tables 5.1 and 5.2 while SF_2 values are taken from respective literature.

The numerical validation of formula (5.26) against data is shown in figure 5.7. This Figure shows the relationship between the $\frac{\alpha_s}{\alpha}$ index and SF_2. In this figure, we superimpose two sets of data. First, we plot the model results from Tables 5.3 and 5.4, and then superimpose experimental results from Joiner et. al [45]. The plot in Joiner et. al [45] contains 33 different cell lines. Although Figure 5.7 has fewer cell lines, we observe a good qualitative agreement between model results and a subset of the data from Joiner et. al [45]. This affirms that the values of $-\alpha_s$ computed from formula (5.26) agree with the existing

	V79 G1	V79 S	V79 G2	T98G G1	T98G S	T98G G2	U373 G1	U373 S	U373 G2
$-\alpha_s$	0.253± 0.016	0.155± 0.067	2.779± 2.017	1.157± 0.549	1.335± 0.491	5.890± 4.202	0.028± 0.017	0.120± 0.054	5.203± 3.195
$\frac{\alpha_s}{\alpha}$	1.012	1.824	9.172	8.900	10.26	28.05	1.400	1.200	32.52
SF_2	0.63	0.77	0.53	0.83	0.67	0.61	0.61	0.70	0.49

Table 5.4: Computed values of $\frac{\alpha_s}{\alpha}$ and literature values of the SF_2 for synchronous cell lines. The mean ± SD of $-\alpha_s$ are computed from (5.26) using the estimated parameters in Table 5.2; values of $\frac{\alpha_s}{\alpha}$ are computed using the mean of $-\alpha_s$ and the values of $-\alpha$ from Table 5.2; SF_2 data are taken from the respective literature.

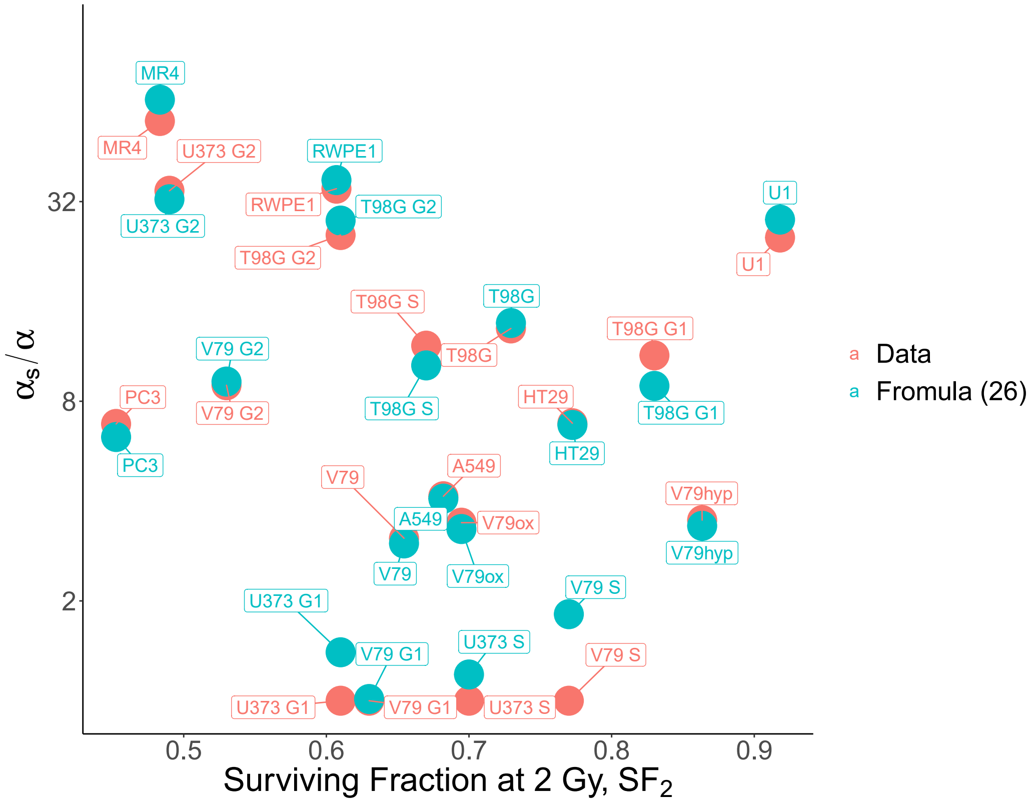

Figure 5.7: $\frac{\alpha_s}{\alpha}$ index measured at low doses of radiation against the surviving fraction measured at 2 Gy, SF_2. Red bullets represent data of different synchronous and asynchronous cells line from [45, 67, 108]; green bullets represent the computational results from formula (5.26).

data.

5.6 Relationship between the $\frac{\alpha_s}{\alpha}$ index and SF_2

As noted earlier, considerable attempt has been made in the past to describe the relationship between the degree of HRS exhibited in a cell and its radioresistance at 2 Gy. In [57], the authors found that cells that exhibit a higher degree of HRS also demonstrate a significant increase in radioresistance at 2 Gy. It was later found in [45] that more data from additional cell lines do not bear this relationship. Figure 5.7 also does not bear out such relationship.

In this section, we will analytically derive this relationship and also nu-

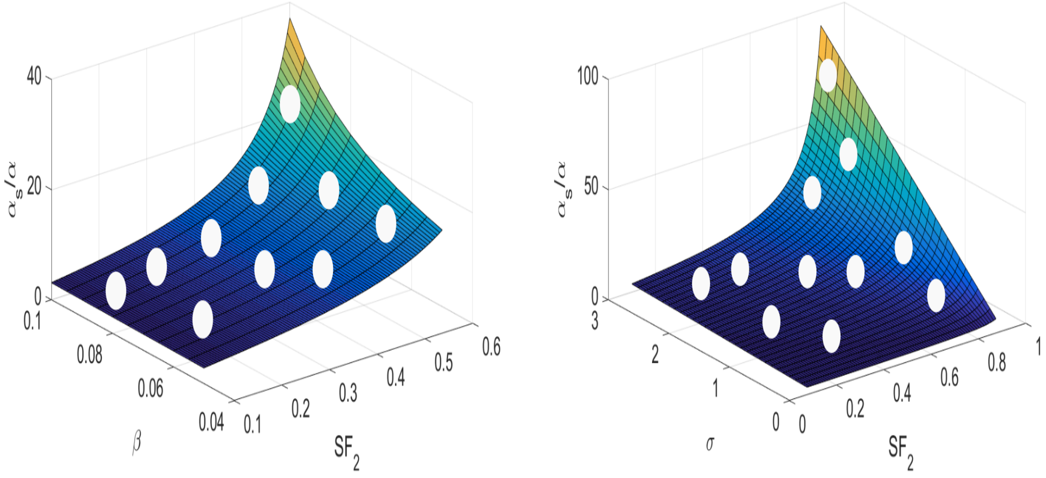

(a) **(b)**

Figure 5.8: Surface plot of the relationship (5.42) between the $\frac{\alpha_s}{\alpha}$ index and SF_2, the surviving fraction at 2 Gy, at different values of σ and β, respectively. The white dots represent different cell lines depending on their σ and β values. (a) The surface plot for a fixed $\sigma = 2$; (b) The surface plot for a fixed $\beta = 0.01\ Gy^{-2}$.

merically explore the relationship for better understanding of the relationship between the surviving fraction at 2 Gy and the extent to which the HRS phenomenon is exhibited in a cell. Fortunately, the derivation is simplified because of the earlier work in Section 5.4.

From the LQ model, we derive;

$$SF_2 := SF(2) = e^{-2\alpha-4\beta}.$$

This implies that

$$-\alpha \quad = \quad \frac{\ln(SF_2) + 4\beta}{2}. \tag{5.39}$$

From (5.26), we have

$$\frac{\alpha_s}{\alpha} = 1 + \frac{2\gamma_0\eta}{\alpha}\Big(\frac{u_0}{u_0+w_0}\Big)\Big(1 - \frac{1-e^{-\kappa t_0}}{\kappa t_0}\Big) := 1 + \frac{\sigma}{\alpha} > 0, \tag{5.40}$$

where

$$\sigma \;=\; 2\gamma_0\eta\Big(\frac{u_0}{u_0+w_0}\Big)\Big(1-\frac{1-e^{-\kappa t_0}}{\kappa t_0}\Big). \tag{5.41}$$

Henceforth, the parameter σ in (5.41) will be referred to as the *intrinsic radiosensitivity* of a cell. This terminology makes sense since it is the indirect radiation effect that determines the degree of HRS a cell exhibits. Combining (5.39) and (5.40) gives

$$\frac{\alpha_s}{\alpha} \;=\; 1-\frac{2\sigma}{\ln(SF_2)+4\beta}, \tag{5.42}$$

which depends on σ, the cell's intrinsic radiosensitivity, β, the rate at which binary misrepair of pairs of DSB from different radiation tracks lead to lethal lesions, and SF_2, the surviving fraction at 2 Gy. Our interest is to understand how these three parameters affect the data in Figure 5.7 using (5.42).

As noted earlier, Lambin et. al [57] suggested that a universal relationship between the $\frac{\alpha_s}{\alpha}$ index and SF_2 should exist, but that the hypothesis was not supported by the study of more cell lines. Here we find that such a relationship does exist. However, it depends on two cell-specific parameters, the intrinsic radiosensitivity σ and the direct radiation sensitivity β. In Figure 5.8, we show that the cell lines we examined do fall onto the surface defined by (5.42). Since it is hard to visualize a plot in 4-dimensions, we fix either σ or β in order to generate a surface plot of the function (5.42). It is worth noting that function (5.42) has a vertical asymptote at $SF_2 = e^{-4\beta}$ for each value of β. Figure 5.8a is a surface plot of (5.42) for $\sigma = 2$. This plot is an increasing manifold in both β and SF_2, respectively. The white dots represent different cell lines lying on the manifold based on their corresponding values for β and SF_2. Similarly, the surface plot in Figure 5.8b for a fixed $\beta = 0.01\ Gy^{-2}$ also shows increasing trends both in σ and SF_2 and a good match with the white dots corresponding to different cell lines. Note that if we project these plots onto the $(\frac{\alpha_s}{\alpha}, SF_2)$ plane, we will get a 2-dimensional plot similar to Figure 5.7, but in which the trends no longer are obvious. Hence, the trend suggested by Lambin et. al [57] indeed holds across cell lines. In other word, if the data in Figure 5.7 was plotted in 3-dimension with β or σ as the third axis, we will have different cell lines lying on different layers of these manifolds depending on and increasing in both β and σ.

5.7 Discussion

The phenomenon of low-dose hyper-radiosensitivity has been observed across many different kind of cell lines. Several malignant cancer cells like glioma cells (T98G) and prostate cancer cells (PC3) are among the cells that exhibit this low-dose phenomenon. Many researchers [15, 26, 103, 113] are currently investigating how this phenomenon can be exploited to improve the effectiveness of cancer radiotherapies. The major obstacle to this idea is the superficiality in the level of understanding of this low-dose phenomenon.

It is worth noting that there are other mechanisms, which are not cell cycle-based, that can trigger the low-dose HRS phenomenon. For example, the mechanism of bystander effects has been implicated in the HRS phenomenon in [89, 93, 78, 86]. Moreover, Mothersill et al. in [81] have shown that both the mechanisms of bystander effects and G2 checkpoint are two mutually exclusive cellular events.

The most common approach for measuring this low-dose phenomenon in a cell is by comparing the initial slope of its SF curve α_s, to that of its initial slope of the SF curve α, described by the LQ model. That is, by determining the $\frac{\alpha_s}{\alpha}$ index. We understand that this index quantifies the degree of HRS in a cell and must relate to some of the molecular cascades or signaling pathways implicated in the occurrence of HRS phenomenon [53, 54, 20]. However, the specific form of this relationship is yet unknown.

In this chapter, we attempt to unravel this relationship by building a system of ODE that captures the interaction between radiation exposure and cells in different cycle phases. Our model is able to fully capture the observed HRS phenomenon in ten different asynchronous cell lines and three different synchronous cells in different cell cycle phases.

The derivation in Section 5.4 of $-\alpha_s$, the initial slope of the SF curve, reveals the dependence of $-\alpha_s$ on the proportion of cells in the G2 phase, the rate of mitotic catastrophe experienced by damaged G2-phase cells, the rate of radiation-induced cell damage, the rate of damage repair, and the duration of radiation exposure. This is consistent with experimental observations that damaged G2-phase cells which evade the early G2-checkpoint to proceed to mitosis undergo mitotic catastrophe, which manifests itself as the HRS phenomenon as observed in the surviving fraction curve. Although, our result is not surprising, the analytic quantification of this dependence is novel and we observe a good qualitative agreement between this dependence and experimental data as shown in Figure 5.7.

In the case where the duration of radiation exposure is long enough to accommodate DNA repair, we observe that the repair rate θ, and the rate of mitotic catastrophe κ, contribute differently to the degree at which a cell exhibits HRS. Our model shows that for small mitotic catastrophe rate κ, the slope $-\alpha_s$ of the SF curve is more sensitive to changes in the DNA repair rate θ, than for larger values of κ.

In these analytic relationships, we realize that there is no dependence on any of the parameters in the checkpoint function, $c(D)$. This further supports the hypothesis that the low-dose HRS is a result of ineffective checkpoint activity while the IRR is a consequence of checkpoint activation. The model developed in this chapter can also be used to study the effect of checkpoint activity on the low-dose increased radioresistance phenomenon. However, this will be outside the scope of consideration since we are only exploring the phenomenon of HRS in this chapter.

Another important concern in (5.26) is that it does not consider the effect of cells that were damaged in non-G2 phases but have progressed into G2 phase with unrepaired damage. For instance, suppose only cells in non-G2 phases are irradiated. In a matter of time, there will be more cells entering into the G2 phase, some of which will carry over damage from other cycle phases. It is then reasonable to ask if these damaged cells in G2 phase also contribute to the mechanism underlying the phenomenon of HRS. In response to this concern, there are biological experiments [53, 54] that have shown that the checkpoint mechanisms that control the mitosis of G2 cells that carry over damage from other phases is different from the mechanism that controls the cells that sustain radiation damage right in the G2 phase. The checkpoint that controls the former is called the Sinclair Checkpoint while the checkpoint that controls the latter is called the Early G2 Checkpoint. An experiment by Krueger et. al. in [53] has shown that the Sinclair checkpoint does not contribute to the HRS phenomenon. This is also confirmed in the formula for the initial slope of the SF curve in (5.27).

In order to investigate the relationship between the $\frac{\alpha_s}{\alpha}$ index and SF_2, the surviving fraction at 2 Gy (or equivalently radioresistance at 2 Gy), we derive an analytical formula which is a function of three parameters, namely; SF_2, the surviving fraction at 2 Gy, σ, the intrinsic radiosensitivity, and β, the rate of binary misrepair of pairs of DSB forming lethal lesions. We found that for each value of either σ or β, the increasing trend in SF_2 is preserved by a manifold increasing in either both σ and SF_2 or β and SF_2. Thus, the cells with higher $\frac{\alpha_s}{\alpha}$ index can also have higher SF_2 value depending on the corresponding values of σ and β. This result generalizes Lambin's result in [57] to any cell lines.

In the experiments for measuring the surviving fraction data, irradiated cells undergo about two weeks of incubation period after which the surviving cells are determined. Our mathematical derivations do not account for the cellular dynamics during this incubation period. Our model simply assumes that the outcome of the incubation can be approximated by computing the surviving fraction from our model immediately after an exposure. This assumption was justified by the qualitative agreement between our model computational results and the experimental data.

The current understanding of the low-dose HRS is still limited in the context of cell lines. There is a need to understand the connection to low-dose radiation in the context of human tissue. Such an understanding may have implications for current radiotherapy practices and perhaps could point the way to treatment strategies not yet considered.

Chapter 6

Discussion

This thesis contains the formulations and analyses of novel continuum mathematical models that describe the effects of low-dose radiation on cell survival and their medical implications. We used the models to investigate the HRS/IRR phenomenon. Based on biological insights, we focused on two cellular occurrences, namely radiation-induced bystander effects, and the activities of the G2-checkpoint, which are hypothesized to underlie the low-dose HRS/IRR phenomenon. We also explored the therapeutic consequences of bystander effects on the invasion of tumor cells into their neighboring normal tissues.

The main research questions we wished to address in this thesis were outlined in the introduction. These questions and their corresponding answers are:

- Can bystander effects explain the HRS/IRR phenomena? The answer is yes, as I was able to fit the bystander model to cell survival data of glioma cells of Joiner et. al in [45].

- What are the dynamics of radiation-induced bystander signals in tissues? I employed a detailed phase plane and bifurcation analyses of the system of equations used to model the bystander effects, finding an interesting saddle-node bifurcation that can explain the longevity of the bystander signal in tissues.

- Are mathematical properties like local and global existence and global attractor supported by the system of PDEs developed to model the bystander effects? I present a full local and global existence theory and results on global attractors for specific radiation schedules.

- What are the effects of bystander signals on the speed and shape of invading tumor waves into its surrounding normal tissue? I was able to quantify the invasion effect of the bystander signal, which can lead to accelerated cancer invasion.

- Can the activity of the G2-checkpoint explain the HRS/IRR phenomenon? The answer is yes, since I was able to fit the system of equations that model the activity of the G2 checkpoint to the cell survival data of glioblastoma, Chinese hamster, prostate cancer, human lung carcinoma, human colon cancer, prostate epithelial cell, and human astrocytoma cell [45, 108, 73, 66, 69, 66, 69, 118, 73].

- How does the classical index $\frac{\alpha_s}{\alpha}$ for the HRS in cells relate to the underlying cellular events that contribute to its occurrence? The analysis of the system of equations that model the G2-checkpoint dynamics enabled me to find an explicit relation of the $\frac{\alpha_s}{\alpha}$ ratio to the model parameters. The medical implications are discussed in Chapter 5.

- Is there a relationship between the HRS index $\frac{\alpha_s}{\alpha}$ and the cell surviving fraction at 2 Gy? Indeed, we can find an explicit relationship between the index $\frac{\alpha_s}{\alpha}$ and SF_2, which fits the observed experimental data really well.

In Chapter 2, we began by improving on existing models of radiation-induced bystander effects by incorporating novel features, which are largely suggested by the dynamics of the cytochrome-complex. The additional features of our model are:

- Modeling both the cellular evolution and bystander signal dynamics with reaction-diffusion partial differential equations;

- Modeling bystander responses in both irradiated and neighboring cells with continuous functions;

- Incorporating more bystander effects such as cell death, DNA damage, and DNA repair delay;

- Assuming that there is no proliferation in damaged cells since they should experience cell cycle arrest;

- Assuming that damaged cells continuously emit bystander signals as long as they are not dead or repaired.

To model the bystander responses in both irradiated and surrounding cells with continuous functions, we employed the threshold-dependent hyperbolic tangent function. The shortcoming of this approach is the introduction of more parameters into the model. Some of these parameters, like the minimum concentration of bystander signal that triggers bystander effect were not available in the literature. Availability of such experimental data will better inform our model and also suggest new scientific questions that can be tested with our model.

We used the method of affine's invariant ensemble MCMC sampler [35] to fit this novel model to data of surviving fraction of glioblastoma cells in Chapter 2. The estimated values for the minimum threshold for bystander effects suggests a possible sequence of occurrence of the bystander effects such as bystander signal-induced cell death, DNA repair delay, and signal-induced DNA damage. As pointed out earlier, more experiments are needed to further validate these results.

In Chapter 3, we showed existence of weak solutions to the system of reaction-diffusion model for radiation-induced bystander effects. We also proved the existence of the global attractor for the model. In the literature, there are rich mathematical theories for studying the structures of global attractors of gradient systems. These are systems that posses a Lyapunov functional, which provides a powerful method to investigate the structure of the global attractor. However, similar theory for non-gradient systems is lacking and hence, proving the structure of the global attractor for our model still remains an open question.

This model, in its present state, cannot be used to used to study the dynamics of radiation-induced abscopal effects [10]. These effects describe cellular responses to bystander signals emitted by cells in a distant location. Aside from the normal diffusion, the bystander signals propagation can also be assisted by body fluids like the blood to reach distant cells. Although, the model can be extended to study such effects by introducing nonlocal terms, we did not consider such class of cellular response in this thesis.

In Chapter 4, we investigated the role of bystander effects on the invasion waves of tumor cells into surrounding healthy tissues. The model in Chapter 2 was extended to accommodate cellular interactions between tumor cells and their surrounding normal tissues. We showed that bystander signals can enhance the speed of tumor invasion into surrounding healthy tissues. We found an asymptotic wave speed for tumor waves from a tumor-only steady state invading into a healthy-tissue-only steady state, which corresponds closely to the wave speed observed numerically. We also found the parameter regime that supports such invasive behavior.

In Chapter 5, we formulated and analyzed a continuum system of ordinary differential equations, which incorporated cell cycle dynamics, radiation treatment, and the G2-checkpoint dynamics. Under mild assumptions on the duration of radiation exposure, we were able to derive an analytical formula that connects the magnitude of HRS in cell lines to some of its underlying cell cycle events. More work is still needed to understand the dynamics of the low-dose HRS cell response when there is no restriction on the exposure time. However, the exposure time in most *in-vitro* experiments for surviving fraction is less than the average repair time, which is far less than the minimum duration of a cell in any phase. As a consequence of our derivation, we were also able to relate the magnitude of HRS in a cell to its radio-resistance at 2 Gy, and thereby settle a debate in the literature.

We found an experiment [81] that suggests that the two cellular events (bystander signal and G2-checkpoint) studied in this thesis are mutually exclusive in some cell lines. The underlying mechanism driving such exclusive relationship is still not well understood. The two models developed in this thesis can be leveraged to build a more informative model that can investigate such relationship. However, a major obstacle to such investigation is the present lack of experimental data to develop such model.

In conclusion, we have made significant progress in the understanding of the phenomenon of low-dose hyper-radiosensitivity via modeling the radiation-induced bystander effects (RIBEs) and the activities of the G2-checkpoint. Using a continuum framework, we investigated the dynamics of bystander signals and explained the various dynamics reported in the literature. Also in a continuum framework, we showed that bystander signal can enhance tumor invasion into surrounding healthy tissue. We also found conditions under which such invasion can be stopped or even reversed. Finally, we were able to connect HRS effect to underlying cellular mechanism through a system of ordinary differential equations. We were also able to derive the long-debated relationship between HRS in cells and their radio-resistance at 2 Gy.

Perhaps, the most important significance of this thesis are new possible research directions that have been identified. So far, we have studied the low-dose HRS/IRR phenomenon in cell lines. However, the main interest is to understand these effects in the context of tissue radiation. This work can be extended to study HRS/IRR in tissues and can perhaps suggest innovative cancer therapies not yet considered.

Bibliography

[1] Jérôme Alexandre, Yumin Hu, Weiqin Lu, Helene Pelicano, and Peng Huang. Novel action of paclitaxel against cancer cells: bystander effect mediated by reactive oxygen species. *Cancer Research*, 67(8):3512–3517, 2007.

[2] Francesca Antonelli, Mauro Belli, Giacomo Cuttone, Valentina Dini, Giuseppe Esposito, Giustina Simone, Eugenio Sorrentino, and Maria Antonella Tabocchini. Induction and repair of DNA double-strand breaks in human cells: dephosphorylation of histone H2AX and its inhibition by calyculin a. *Radiation Research*, 164(4):514–517, 2005.

[3] Edouard I Azzam, Sonia M de Toledo, and John B Little. Direct evidence for the participation of gap junction-mediated intercellular communication in the transmission of damage signals from α-particle irradiated to nonirradiated cells. *Proceedings of the National Academy of Sciences*, 98(2):473–478, 2001.

[4] F Ballarini, D Alloni, A Facoetti, A Mairani, R Nano, and A Ottolenghi. Modelling radiation-induced bystander effect and cellular communication. *Radiation Protection Dosimetry*, 122(1-4):244–251, 2006.

[5] Oleg V Belyakov, Stephen A Mitchell, Deep Parikh, Gerhard Randers-Pehrson, Stephen A Marino, Sally A Amundson, Charles R Geard, and David J Brenner. Biological effects in unirradiated human tissue induced by radiation damage up to 1 mm away. *Proceedings of the National Academy of Sciences of the United States of America*, 102(40):14203–14208, 2005.

[6] Carl M Bender and Steven A Orszag. *Advanced mathematical methods for scientists and engineers I: Asymptotic methods and perturbation theory.* Springer Science & Business Media, 2013.

[7] Eric J Bernhard, Eric J Stanbridge, Swati Gupta, Anjali K Gupta, Daniel Soto, Vincent J Bakanauskas, George J Cerniglia, Ruth J

Muschel, and W Gillies McKenna. Direct evidence for the contribution of activated n-ras and k-ras oncogenes to increased intrinsic radiation resistance in human tumor cell lines. *Cancer Research*, 60(23):6597–6600, 2000.

[8] Anupam Bishayee, Helene Z Hill, Dana Stein, Dandamudi V Rao, and Roger W Howell. Free radical-initiated and gap junction-mediated bystander effect due to nonuniform distribution of incorporated radioactivity in a three-dimensional tissue culture model. *Radiation Research*, 155(2):335–344, 2001.

[9] Swati Biswas, Marta Guix, Cammie Rinehart, Teresa C Dugger, Anna Chytil, Harold L Moses, Michael L Freeman, and Carlos L Arteaga. Inhibition of TGF-β with neutralizing antibodies prevents radiation-induced acceleration of metastatic cancer progression. *Journal of Clinical Investigation*, 117(5):1305, 2007.

[10] Benjamin J Blyth and Pamela J Sykes. Radiation-induced bystander effects: what are they, and how relevant are they to human radiation exposures? *Radiation Research*, 176(2):139–157, 2011.

[11] Marie Boyd, Susan C Ross, Jennifer Dorrens, Natasha E Fullerton, Ker Wei Tan, Michael R Zalutsky, and Robert J Mairs. Radiation-induced biologic bystander effect elicited in vitro by targeted radiopharmaceuticals labeled with α-, β-, and auger electron–emitting radionuclides. *Journal of Nuclear Medicine*, 47(6):1007–1015, 2006.

[12] David J Brenner. The linear-quadratic model is an appropriate methodology for determining isoeffective doses at large doses per fraction. In *Seminars in Radiation Oncology*, volume 18, pages 234–239. Elsevier, 2008.

[13] Andrew F Brouwer and Marisa C Eisenberg. The underlying connections between identifiability, active subspaces, and parameter space dimension reduction. *arXiv preprint arXiv:1802.05641*, 2018.

[14] Jiyang Cai, Jie Yang, and DeanP Jones. Mitochondrial control of apoptosis: the role of cytochrome c. *Biochimica et Biophysica Acta (BBA)-Bioenergetics*, 1366(1):139–149, 1998.

[15] George M Cannon, Wolfgang A Tomé, H Ian Robins, and Steven P Howard. Pulsed reduced dose-rate radiotherapy: case report. *Journal of Neuro-Oncology*, 83(3):307–311, 2007.

[16] Maria Castedo, Jean-Luc Perfettini, Thomas Roumier, Karine Andreau, Rene Medema, and Guido Kroemer. Cell death by mitotic catastrophe: a molecular definition. *Oncogene*, 23(16):2825–2837, 2004.

[17] Shaopeng Chen, Y Zhao, Wei Han, SK Chiu, L Zhu, L Wu, and KN Yu. Rescue effects in radiobiology: unirradiated bystander cells assist irradiated cells through intercellular signal feedback. *Mutation Research/Fundamental and Molecular Mechanisms of Mutagenesis*, 706(1):59–64, 2011.

[18] J CH Cheng, CHIA-HUNG Chou, ML Kuo, and CY Hsieh. Radiation-enhanced hepatocellular carcinoma cell invasion with MMP-9 expression through PI3K/Akt/NF-κB signal transduction pathway. *Oncogene*, 25(53):7009–7018, 2006.

[19] Jeong Hyun Cho, Wan Gi Hong, Yu-Jin Jung, Jaeseok Lee, Eunah Lee, Sang-Gu Hwang, Hong-Duck Um, and Jong Kuk Park. γ-ionizing radiation-induced activation of the EGFR–p38/ERK–STAT3/CREB-1–EMT pathway promotes the migration/invasion of non-small cell lung cancer cells and is inhibited by podophyllotoxin acetate. *Tumor Biology*, 37(6):7315–7325, 2016.

[20] C Contreras, G Carrero, and G de Vries. Personal communication. 2017.

[21] Edward Conway, David Hoff, and Joel Smoller. Large time behavior of solutions of systems of nonlinear reaction-diffusion equations. *SIAM Journal on Applied Mathematics*, 35(1):1–16, 1978.

[22] Stanley B Curtis. Lethal and potentially lethal lesions induced by radiation—a unified repair model. *Radiation Research*, 106(2):252–270, 1986.

[23] K Cusato, H Ripps, J Zakevicius, and DC Spray. Gap junctions remain open during cytochrome c-induced cell death: relationship of conductance to bystander cell killing. *Cell Death & Differentiation*, 13(10):1707–1714, 2006.

[24] Paul D Dale, Philip K Maini, and Jonathan A Sherratt. Mathematical modeling of corneal epithelial wound healing. *Mathematical biosciences*, 124(2):127–147, 1994.

[25] Sejal Desai, Alisa Kobayashi, Teruaki Konishi, Masakazu Oikawa, and Badri N Pandey. Damaging and protective bystander cross-talk between human lung cancer and normal cells after proton microbeam irradiation.

Mutation Research/Fundamental and Molecular Mechanisms of Mutagenesis, 763:39–44, 2014.

[26] Joshua T Dilworth, Sarah A Krueger, Mohamad Dabjan, Inga S Grills, John Torma, George D Wilson, and Brian Marples. Pulsed low-dose irradiation of orthotopic glioblastoma multiforme (GBM) in a pre-clinical model: Effects on vascularization and tumor control. *Radiotherapy and Oncology*, 108(1):149–154, 2013.

[27] Wiktor Eckhaus. *Matched asymptotic expansions and singular perturbations*, volume 6. Elsevier, 2011.

[28] Stephen J Elledge. Cell cycle checkpoints: preventing an identity crisis. *Science*, 274(5293):1664, 1996.

[29] Antonio Fasano, Miguel A Herrero, and Marianito R Rodrigo. Slow and fast invasion waves in a model of acid-mediated tumour growth. *Mathematical biosciences*, 220(1):45–56, 2009.

[30] Marie Fernet, Frédérique Mégnin-Chanet, Janet Hall, and Vincent Favaudon. Control of the g2/m checkpoints after exposure to low doses of ionising radiation: implications for hyper-radiosensitivity. *DNA Repair*, 9(1):48–57, 2010.

[31] Douglas K Frank, Bozena Szymkowiak, Olgica Josifovska-Chopra, Torahiko Nakashima, and Kathleen W Kinnally. Single-cell microinjection of cytochrome c can result in gap junction–mediated apoptotic cell death of bystander cells in head and neck cancer. *Head & Neck*, 27(9):794–800, 2005.

[32] Chong Feng Gao, Shuo Ren, Lilin Zhang, Takuma Nakajima, Shizuko Ichinose, Toshiko Hara, Katsuro Koike, and Nobuo Tsuchida. Caspase-dependent cytosolic release of cytochrome c and membrane translocation of bax in p53-induced apoptosis. *Experimental Cell Research*, 265(1):145–151, 2001.

[33] Robert A Gatenby and Edward T Gawlinski. A reaction-diffusion model of cancer invasion. *Cancer research*, 56(24):5745–5753, 1996.

[34] Jiafen Gong, Mairon M dos Santos, Chris Finlay, and Thomas Hillen. Are more complicated tumour control probability models better? *Mathematical Medicine and Biology*, 30(1):1–19, 2013.

[35] Jonathan Goodman and Jonathan Weare. Ensemble samplers with affine invariance. *Communications in Applied Mathematics and Computational Science*, 5(1):65–80, 2010.

[36] Vicente Goyanes-Villaescusa. Chromosomal abnormalities in lymphocytes of children and baby rabbits born from mothers treated by x-irradiation before pregnancy. a transplacentary plasmatic chromosome-damaged factor? *Blut*, 22(2):93–96, 1971.

[37] Qing Gu, Yan He, Jianfeng Ji, Yifan Yao, Wenhao Shen, Jialin Luo, Wei Zhu, Han Cao, Yangyang Geng, Jing Xu, et al. Hypoxia-inducible factor 1α (HIF-1α) and reactive oxygen species (ROS) mediates radiation-induced invasiveness through the SDF-1α/CXCR4 pathway in non-small cell lung carcinoma cells. *Oncotarget*, 6(13):10893, 2015.

[38] Eric J Hall, Amato J Giaccia, et al. *Radiobiology for the Radiologist*, volume 6. Lippincott Williams & Wilkins Philadelphia:, 2006.

[39] Douglas Hanahan and Robert A Weinberg. The hallmarks of cancer. *cell*, 100(1):57–70, 2000.

[40] Douglas Hanahan and Robert A Weinberg. Hallmarks of cancer: the next generation. *cell*, 144(5):646–674, 2011.

[41] Dimitri Hauri, Ben Spycher, Anke Huss, Frank Zimmermann, Michael Grotzer, Nicolas von der Weid, Damien Weber, Adrian Spoerri, Claudia E Kuehni, Martin Röösli, et al. Domestic radon exposure and risk of childhood cancer: a prospective census-based cohort study. *Environmental Health Perspectives*, 121(10):1239–1244, 2013.

[42] Mingyuan He, Chen Dong, Ruiping Ren, Dexiao Yuan, Yuexia Xie, Yan Pan, and Chunlin Shao. Radiation enhances the invasiveness of irradiated and nonirradiated bystander hepatoma cells through a VEGF-MMP2 pathway initiated by p53. *Radiation Research*, 180(4):389–397, 2013.

[43] Burong Hu, Lijun Wu, Wei Han, Leilei Zhang, Shaopeng Chen, An Xu, Tom K Hei, and Zengliang Yu. The time and spatial effects of bystander response in mammalian cells induced by low dose radiation. *Carcinogenesis*, 27(2):245–251, 2006.

[44] Michael C Joiner, Philippe Lambin, and Brian Marples. Adaptive response and induced resistance. *Comptes Rendus de l'Académie des Sciences-Series III-Sciences de la Vie*, 322(2):167–175, 1999.

[45] Michael C Joiner, Brian Marples, Philippe Lambin, Susan C Short, and Ingela Turesson. Low-dose hypersensitivity: current status and possible mechanisms. *International Journal of Radiation Oncology* Biology* Physics*, 49(2):379–389, 2001.

[46] Alexandre Kaliski, Laurence Maggiorella, Keith A Cengel, Denis Mathe, Valerie Rouffiac, Paule Opolon, Nathalie Lassau, Jean Bourhis, and Eric Deutsch. Angiogenesis and tumor growth inhibition by a matrix metalloproteinase inhibitor targeting radiation-induced invasion. *Molecular Cancer Therapeutics*, 4(11):1717–1728, 2005.

[47] Timothy P Kegelman, Bainan Wu, Swadesh K Das, Sarmistha Talukdar, Jason M Beckta, Bin Hu, Luni Emdad, Kristoffer Valerie, Devanand Sarkar, Frank B Furnari, et al. Inhibition of radiation-induced glioblastoma invasion by genetic and pharmacological targeting of MDA-9/syntenin. *Proceedings of the National Academy of Sciences*, page 201616100, 2016.

[48] Igor K Khvostunov and Hooshang Nikjoo. Computer modelling of radiation-induced bystander effect. *Journal of Radiological Protection*, 22(3A):A33, 2002.

[49] Jae Kyoung Kim and Trachette L Jackson. Mechanisms that enhance sustainability of p53 pulses. *PLoS One*, 8(6):e65242, 2013.

[50] M Kohandel, M Kardar, M Milosevic, and S Sivaloganathan. Dynamics of tumor growth and combination of anti-angiogenic and cytotoxic therapies. *Physics in Medicine and Biology*, 52(13):3665, 2007.

[51] Anna Kovalchuk, Richelle Mychasiuk, Arif Muhammad, Shakhawat Hossain, Slava Ilnytskyy, Abhijit Ghose, Charles Kirkby, Esmaeel Ghasroddashti, Olga Kovalchuk, and Bryan Kolb. Liver irradiation causes distal bystander effects in the rat brain and affects animal behaviour. *Oncotarget*, 7(4):4385, 2016.

[52] SA Krueger, MC Joiner, M Weinfeld, E Piasentin, and B Marples. Role of apoptosis in low-dose hyper-radiosensitivity. *Radiation research*, 167(3):260–267, 2007.

[53] Sarah A Krueger, Spencer J Collis, Michael C Joiner, George D Wilson, and Brian Marples. Transition in survival from low-dose hyper-radiosensitivity to increased radioresistance is independent of activation of ATM SER1981 activity. *International Journal of Radiation Oncology* Biology* Physics*, 69(4):1262–1271, 2007.

[54] Sarah A Krueger, George D Wilson, Evano Piasentin, Michael C Joiner, and Brian Marples. The effects of G2-phase enrichment and checkpoint abrogation on low-dose hyper-radiosensitivity. *International Journal of Radiation Oncology* Biology* Physics*, 77(5):1509–1517, 2010.

[55] RKK Lam, YK Fung, W Han, and KN Yu. Rescue effects: irradiated cells helped by unirradiated bystander cells. *International journal of molecular sciences*, 16(2):2591–2609, 2015.

[56] RKK Lam, Wei Han, and KN Yu. Unirradiated cells rescue cells exposed to ionizing radiation: Activation of nf-κb pathway in irradiated cells. *Mutation Research/Fundamental and Molecular Mechanisms of Mutagenesis*, 782:23–33, 2015.

[57] P Lambin. Might intrinsic radioresistance of human tumour cells be induced by radiation? *International Journal of Radiation Biology*, 69(3):279–290, 1996.

[58] P Lambin, B Marples, B Fertil, EP Malaise, and MC Joiner. Hypersensitivity of a human tumour cell line to very low radiation doses. *International Journal of Radiation Biology*, 63(5):639–650, 1993.

[59] Pedro Carlos Lara, Jesús Joaquín López-Peñalver, Virgínea de Araújo Farias, M Carmen Ruiz-Ruiz, Francisco Javier Oliver, and José Mariano Ruiz de Almodóvar. Direct and bystander radiation effects: A biophysical model and clinical perspectives. *Cancer Letters*, 356(1):5–16, 2015.

[60] Klervi Leuraud, David B Richardson, Elisabeth Cardis, Robert D Daniels, Michael Gillies, Jacqueline A O'Hagan, Ghassan B Hamra, Richard Haylock, Dominique Laurier, Monika Moissonnier, et al. Ionising radiation and risk of death from leukaemia and lymphoma in radiation-monitored workers (inworks): an international cohort study. *The Lancet Haematology*, 2(7):e276–e281, 2015.

[61] Rachel Lintott, Stephen McMahon, Kevin Prise, Celine Addie-Lagorio, and Carron Shankland. Using process algebra to model radiation induced bystander effects. In *Computational Methods in Systems Biology*, pages 196–210. Springer, 2014.

[62] Sally A Lorimore, Joanne M McIlrath, Philip J Coates, and Eric G Wright. Chromosomal instability in unirradiated hemopoietic cells resulting from a delayed in vivo bystander effect of γ radiation. *Cancer Research*, 65(13):5668–5673, 2005.

[63] Martine Marion. Attractors for reaction-diffusion equations: existence and estimate of their dimension. *Applicable Analysis*, 25(1-2):101–147, 1987.

[64] Pavel Marozik, Carmel Mothersill, Colin B Seymour, Irma Mosse, and Sergeyi Melnov. Bystander effects induced by serum from survivors of the chernobyl accident. *Experimental Hematology*, 35(4):55–63, 2007.

[65] B Marples. Is low-dose hyper-radiosensitivity a measure of G2-phase cell radiosensitivity? *Cancer and Metastasis Reviews*, 23(3-4):197–207, 2004.

[66] B Marples and MC Joiner. The response of chinese hamster V79 cells to low radiation doses: Evidence of enhanced sensitivity of the whole cell population. *Radiation Research*, 133(1):41–51, 1993.

[67] B Marples, BG Wouters, and MC Joiner. An association between the radiation-induced arrest of G2-phase cells and low-dose hyper-radiosensitivity: a plausible underlying mechanism? *Radiation Research*, 160(1):38–45, 2003.

[68] Brian Marples and Spencer J Collis. Low-dose hyper-radiosensitivity: past, present, and future. *International Journal of Radiation Oncology* Biology* Physics*, 70(5):1310–1318, 2008.

[69] Brian Marples, Michael C Joiner, and Kirsten A Skov. The effect of oxygen on low-dose hypersensitivity and increased radioresistance in chinese hamster V79-379A cells. *Radiation Research*, 138(1s):S17–S20, 1994.

[70] Brian Marples, BG Wouters, SJ Collis, AJ Chalmers, and Michael C Joiner. Low-dose hyper-radiosensitivity: a consequence of ineffective cell cycle arrest of radiation-damaged G2-phase cells. *Radiation Research*, 161(3):247–255, 2004.

[71] KA Skov Marples, P. Lambin and B MC Joiner. Low dose hyper-radiosensitivity and increased radioresistance in mammalian cells. *International Journal of Radiation Biology*, 71(6):721–735, 1997.

[72] S Marsili-Libelli, S Guerrizio, and N Checchi. Confidence regions of estimated parameters for ecological systems. *Ecological Modelling*, 165(2-3):127–146, 2003.

[73] Lynn Martin, Brian Marples, Mary Coffey, Mark Lawler, Donal Hollywood, and Laure Marignol. Recognition of O6MEG lesions by MGMT

and mismatch repair proficiency may be a prerequisite for low-dose radiation hypersensitivity. *Radiation Research*, 172(4):405–413, 2009.

[74] Jessica B McGillen, Eamonn A Gaffney, Natasha K Martin, and Philip K Maini. A general reaction–diffusion model of acidity in cancer invasion. *Journal of mathematical biology*, 68(5):1199–1224, 2014.

[75] S.J. McMahon, K. T. Butterworth, C. Trainor, C. K. McGarry, J. M. O'Sullivan, G. Schettino, A. R. Hounsell, and K. M. Prise. A kinetic-based model of radiation-induced intercellular signalling. *PloS One*, 8(1):e54526, 2013.

[76] William F Morgan. Non-targeted and delayed effects of exposure to ionizing radiation: I. radiation-induced genomic instability and bystander effects in vitro. *Radiation Research*, 159(5):567–580, 2003.

[77] C Mothersill, C Bucking, RW Smith, N Agnihotri, A O'Neill, M Kilemade, and CB Seymour. Communication of radiation-induced stress or bystander signals between fish in vivo. *Environmental Science & Technology*, 40(21):6859–6864, 2006.

[78] C Mothersill and C Seymour. Medium from irradiated human epithelial cells but not human fibroblasts reduces the clonogenic survival of unirradiated cells. *International Journal of Radiation Biology*, 71(4):421–427, 1997.

[79] Carmel Mothersill, Fiona Lyng, Colin Seymour, Paula Maguire, Sally Lorimore, and Eric Wright. Genetic factors influencing bystander signaling in murine bladder epithelium after low-dose irradiation in vivo. *Radiation Research*, 163(4):391–399, 2005.

[80] Carmel Mothersill, Rohin Saroya, Richard W Smith, Harleen Singh, and Colin B Seymour. Serum serotonin levels determine the magnitude and type of bystander effects in medium transfer experiments. *Radiation Research*, 174(1):119–123, 2010.

[81] Carmel Mothersill, C. B. Seymour, and M. C. Joiner. Relationship between radiation-induced low-dose hypersensitivity and the bystander effect. *Radiation Research*, 157(5):526–532, 2002.

[82] Carmel Mothersill and CB Seymour. Bystander and delayed effects after fractionated radiation exposure. *Radiation Research*, 158(5):626–633, 2002.

[83] Carmel Mothersill and Colin Seymour. Radiation-induced bystander effects: evidence for an adaptive response to low dose exposures? *Dose-Response*, 4(4), 2006.

[84] Andrew Murray. Cell cycle checkpoints. *Current Opinion in Cell Biology*, 6(6):872–876, 1994.

[85] James Dickson Murray. *Asymptotic analysis*, volume 48. Springer Science & Business Media, 2012.

[86] Hatsumi Nagasawa and John B Little. Induction of sister chromatid exchanges by extremely low doses of α-particles. *Cancer Research*, 52(22):6394–6396, 1992.

[87] Hooshang Nikjoo and Igor K Khvostunov. Biophysical model of the radiation-induced bystander effect. *International Journal of Radiation Biology*, 79(1):43–52, 2003.

[88] Otilia Nuta and Firouz Darroudi. The impact of the bystander effect on the low-dose hypersensitivity phenomenon. *Radiation and environmental biophysics*, 47(2):265–274, 2008.

[89] Oluwole Olobatuyi, Gerda de Vries, and Thomas Hillen. A reaction–diffusion model for radiation-induced bystander effects. *Journal of Mathematical Biology*, 75(2):341–372, 2017.

[90] Oluwole Olobatuyi, Gerda de Vries, and Thomas Hillen. Effects of G2-checkpoint dynamics on low-dose hyper-radiosensitivity. *Journal of Mathematical Biology*, in-press, 2018.

[91] G Shankar Pant and Nanao Kamada. Chromosome aberrations in normal leukocytes induced by the plasma of exposed individuals. *Hiroshima Journal of Medical Sciences*, 26(2–3):149–154, 1977.

[92] Stephanie Jane Peacock, Martin Krkošek, Mark Alun Lewis, and Subhash Lele. Study design and parameter estimability for spatial and temporal ecological models. *Ecology and evolution*, 7(2):762–770, 2017.

[93] Gibin G Powathil, Alastair J Munro, Mark AJ Chaplain, and Maciej Swat. Bystander effects and their implications for clinical radiation therapy: Insights from multiscale in silico experiments. *Journal of Theoretical Biology*, 401:1–14, 2016.

[94] Kevin M Prise and Joe M O'Sullivan. Radiation-induced bystander signalling in cancer therapy. *Nature Reviews Cancer*, 9(5):351–360, 2009.

[95] Kevin M Prise, Giuseppe Schettino, Melvyn Folkard, and Kathryn D Held. New insights on cell death from radiation exposure. *The Lancet Oncology*, 6(7):520–528, 2005.

[96] KM Prise. Studies of bystander effects in human fibroblasts using a charged particle microbeam. *International Journal of Radiation Biology*, 74(6):793–798, 1998.

[97] Li-Wu Qian, Kazuhiro Mizumoto, Taro Urashima, Eishi Nagai, Naoki Maehara, Norihiro Sato, Motowo Nakajima, and Masao Tanaka. Radiation-induced increase in invasive potential of human pancreatic cancer cells and its blockade by a matrix metalloproteinase inhibitor, CGS27023. *Clinical Cancer Research*, 8(4):1223–1227, 2002.

[98] Jeremy N Rich. Cancer stem cells in radiation resistance. *Cancer research*, 67(19):8980–8984, 2007.

[99] James C Robinson. *Infinite-dimensional dynamical systems: an introduction to dissipative parabolic PDEs and the theory of global attractors*, volume 28. Cambridge University Press, 2001.

[100] Kai Rothkamm, Ines Krüger, Larry H Thompson, and Markus Löbrich. Pathways of DNA double-strand break repair during the mammalian cell cycle. *Molecular and cellular biology*, 23(16):5706–5715, 2003.

[101] Kai Rothkamm and Markus Löbrich. Evidence for a lack of DNA double-strand break repair in human cells exposed to very low X-ray doses. *Proceedings of the National Academy of Sciences*, 100(9):5057–5062, 2003.

[102] Lorna A Ryan, Richard W Smith, Colin B Seymour, and Carmel E Mothersill. Dilution of irradiated cell conditioned medium and the bystander effect. *Radiation Research*, 169(2):188–196, 2008.

[103] Diane Schoenherr, Sarah A Krueger, Lynn Martin, Laure Marignol, George D Wilson, and Brian Marples. Determining if low dose hyper-radiosensitivity (HRS) can be exploited to provide a therapeutic advantage: A cell line study in four glioblastoma multiforme (GBM) cell lines. *International Journal of Radiation Biology*, 89(12):1009–1016, 2013.

[104] Martin Schuler, Ella Bossy-Wetzel, Joshua C Goldstein, Patrick Fitzgerald, and Douglas R Green. p53 induces apoptosis by caspase activation through mitochondrial cytochrome c release. *Journal of Biological Chemistry*, 275(10):7337–7342, 2000.

[105] Colin B Seymour and Carmel Mothersill. Radiation-induced bystander effects – implications for cancer. *Nature Reviews Cancer*, 4(2):158–164, 2004.

[106] S. Short, C. Mayes, M. Woodcock, H. Johns, and M. C. Joiner. Low dose hypersensitivity in the T98G human glioblastoma cell line. *International Journal of Radiation Biology*, 75(7):847–855, 1999.

[107] S. C. Short, J. Kelly, C. R. Mayes, M. Woodcock, and M. C. Joiner. Low-dose hypersensitivity after fractionated low-dose irradiation in vitro. *International Journal of Radiation Biology*, 77(6):655–664, 2001.

[108] SC Short, M Woodcock, B Marples, and MC Joiner. Effects of cell cycle phase on low-dose hyper-radiosensitivity. *International Journal of Radiation Biology*, 79(2):99–105, 2003.

[109] Joel Smoller. *Shock waves and reactiondiffusion equations*, volume 258. Springer Science & Business Media, 2012.

[110] WJ Speake, RA Dean, A Kumar, TM Morris, JH Scholefield, and SA Watson. Radiation induced mmp expression from rectal cancer is short lived but contributes to in vitro invasion. *European Journal of Surgical Oncology (EJSO)*, 31(8):869–874, 2005.

[111] Peter Storz et al. Reactive oxygen species in tumor progression. *Front Biosci*, 10(1-3):1881–1896, 2005.

[112] Roger Temam. *Infinite-dimensional dynamical systems in mechanics and physics*, volume 68. Springer Science & Business Media, 2012.

[113] Wolfgang A Tomé and SP Howard. On the possible increase in local tumour control probability for gliomas exhibiting low dose hyper-radiosensitivity using a pulsed schedule. *The British Journal of Radiology*, 80(949):32–37, 2007.

[114] P Tracqui, GC Cruywagen, DE Woodward, GT Bartoo, JD Murray, and EC Alvord. A mathematical model of glioma growth: the effect of chemotherapy on spatio-temporal growth. *Cell proliferation*, 28(1):17–31, 1995.

[115] Anne Viallefont, Jean-Dominique Lebreton, Anne-Marie Reboulet, and Gerard Gory. Parameter identifiability and model selection in capture-recapture models: a numerical approach. *Biometrical Journal: Journal of Mathematical Methods in Biosciences*, 40(3):313–325, 1998.

[116] Bixiang Wang. Attractors for reaction-diffusion equations in unbounded domains. *Physica D: Nonlinear Phenomena*, 128(1):41–52, 1999.

[117] MV Williams, J Denekamp, and JF Fowler. A review of $\alpha\beta$ ratios for experimental tumors: Implications for clinical studies of altered fractionation. *International Journal of Radiation Oncology* Biology* Physics*, 11(1):87–96, 1985.

[118] Bradly G Wouters, Arturo M Sy, and Lloyd D Skarsgard. Low-dose hypersensitivity and increased radioresistance in a panel of human tumor cell lines with different radiosensitivity. *Radiation Research*, 146(4):399–413, 1996.

[119] Yi-Chu Yu, Pei-Ming Yang, Qiu-Yu Chuah, Yao-Huei Huang, Chih-Wen Peng, Yi-Jang Lee, and Shu-Jun Chiu. Radiation-induced senescence in securin-deficient cancer cells promotes cell invasion involving the IL-6/STAT3 and PDGF-BB/PDGFR pathways. *Scientific Reports*, 3:1675, 2013.

[120] EHW Yum, VWY Choi, D Nikezic, VWT Li, SH Cheng, and KN Yu. Alpha-particle-induced bystander effects between zebrafish embryos in vivo. *Radiation Measurements*, 44(9):1077–1080, 2009.

[121] Tianran Zhang. Minimal wave speed for a class of non-cooperative reaction–diffusion systems of three equations. *Journal of Differential Equations*, 262(9):4724–4770, 2017.

[122] Tianran Zhang, Wendi Wang, and Kaifa Wang. Minimal wave speed for a class of non-cooperative diffusion–reaction system. *Journal of Differential Equations*, 260(3):2763–2791, 2016.